SPATIO-TEMPORAL STATISTICAL CHARACTERIZATION OF BOUNDARY KINEMATIC PHENOMENA OBSERVED ON A SERIES OF TRIAXIAL SAND SPECIMENS

A Dissertation

by

YICHUAN ZHU

Submitted to the Office of Graduate and Professional Studies of
Texas A&M University
in partial fulfillment of the requirements for the degree of

DOCTOR OF PHILOSOPHY

Chair of Committee,	Zenon Medina-Cetina
Committee Members,	Charles Aubeny
	Julie Loisel
	Minsu Cha
Head of Department,	Robin Autenrieth

December 2019

Major Subject: Civil Engineering

ABSTRACT

Soil variability is a complex but ubiquitous phenomenon that derived from many sources of uncertainty. This inherent in-homogeneous behavior can affect the accurate estimation of soil strength and ideally should be fully characterized for informed decision making. However, in traditional geotechnical engineering survey, quantification of soil variability is not routinely performed and materials are collectively considered as a homogenous body. This knowledge gap is likely to inhibit the true understandings of variations in soil properties, and lead the practical design compromised to conservative parameter values. Despite rapid proliferation of sensing techniques having enabled us to collect more detailed deformational evidence, to the author's knowledge, no statistical characterization has been performed on full field measurements. This research introduces a spatio-temporal statistical characterization of boundary kinematic phenomena captured by 3D digital image correlation (DIC) method. The combined interpretation of the displacement and kinematic operators provides a unique uncertainty quantification on the deforming granular media.

First, we introduce a multi-scale data ensemble populated from a series of nominally similar triaxial sand specimens. First- (marginal statistics) and second-order (correlation analysis) statistics are assessed on each data scenario. The results reveal that the presence of shear and expansion band can introduce deformation dependencies in space and time. Also, the uncertainty of deformation pattern is greatly affected by the variability of localization behaviors, which is started as early as hardening phase.

Second, the complete set of 3D kinematic operators under the Cylindrical coordinates-for the first time-applied to the assessment of meso-scale kinematics manifested on triaxial specimens. Our results suggest the kinematic patterns during the course of compression are influenced by factors such as confining pressure, initial density, varying composition, among others. Further statistical analysis of kinematic fields shows that different localization effects can interact with each other as evolved in both space and time. The results shed much light on systematically recognizing prevailing deteriorating mechanisms as well as uncertainty distributions during the process of shearing.

Finally, we include a case study of probabilistic calibration of a visco-elastoplastic model representing the rheological property of sandstone. This is aimed to showcase the methodology we will apply to uncertainty quantification of modeling heterogeneous material responses in our future work.

DEDICATION

I dedicate this work to my wife, and my dear daughter Christie

ACKNOWLEDGEMENTS

I would like to sincerely thank my advisor, Dr. Zenon Medina-Cetina, for his continuous support and conscientious guidance through the course of my doctoral program. Without his expertise, patience and assistance, this work is impossible to complete. I appreciate his constructive insights along this journey which has made my research very colorful and broad.

I would also like to extend my gratitude to my committee members, Dr. Charles Aubeny, Dr. Minsu Cha, Dr. Bani Mallick, and special thanks go to Dr. Julie Loisel who I am honored to work with on the X-grants project. The insightful comments and suggestions from my committee members are invaluable to me.

I am grateful to Dr. Jeff Hart and Dr. Suhasini Subba Rao for their unconditional help and guidance through my learning of advanced statistics. Those new topics have opened up new horizons for my research and it is a privilege to learn from them.

I would like to extend my appreciation to friends in Stochastic Geomechanics Laboratory-Jungrak Son, Tam Duong, Moslem Moradi, Miguel Fernando Ortiz Cahun, Alma Rosa Pineda Contreras, Qudama Albu Jasim, Juan Pablo Alvarado Franco, Jaechan Park, Alexander Abuabara, Guillermo Duran Sierra, Patricia Varela, Yasser Soltanpour, and many former members. I have learned from them and this group has made my life in A&M incredible. My sincere gratitude goes to Araceli Lopez, who provided invaluable support to the whole team.

My heartiest gratitude goes to my wife, Han Fang, to my sister, Jie Wang, to my parents, Bifang Zhu and Bishu Xu, and to all other family members. Thanks for keeping me company on this long walk.

CONTRIBUTORS AND FUNDING SOURCES

Contributors

This work is supervised by a dissertation committee consisting of Professor Zenon Medina-Cetina, Professor Charles Aubeny, and Professor Minsu Cha of Zachry Department of Civil & Environmental Engineering, and Professor of Julie Loisel of Department of Geography.

The experimental data used in Chapter 2, 3, and 4 was initially generated by Dr. Zenon Medina-Cetina's Ph.D. research titled “Probabilistic Calibration of a Soil Model” published in 2006, and later processed by Dr. Ahran Song's Ph.D. research titled “Deformation Analysis of Sand Specimens using 3D-Digital Image Correlation for the Calibration of an Elasto-Plastic Model” which was published in 2012.

The rock creep tests in Chapter 5 were conducted at Chinese University of Geosciences, by Dr. Hu Xinli and Dr. Lu Cong.

All other work conducted for the dissertation was completed by Yichuan Zhu independently.

Funding Sources

Graduate study was supported by a research assistantship provided by Dr. Medina-Cetina, and partly funded by X-grants program which is led by Dr. Julie Loisel from Department of Geography at Texas A&M University.

TABLE OF CONTENTS

Page

LIST OF FIGURES

Page

LIST OF TABLES

Page

1. INTRODUCTION

1.1. Problem statement

Soil variability is a complex but ubiquitous phenomenon that derived from many sources of uncertainties. The inherent variation is usually manifested as varying soil properties, stratigraphy, and spatio-temporal distributions that can be resulted from the synthesis of physical, hydrogeological, chemical and/or biological processes (Li *et al.*, 2014). In Geotechnical survey, such variability is crucial for the accurate estimation of soil strength and ideally should be fully characterized to permit informed decision making and risk management (Lacasse and Nadim, 1996; Phoon and Kulhawy, 1999). However, the practical constraints allow only limited standardized tests to be performed from which the soil parameters are estimated at discrete locations. This deterministic characterization would likely underestimate the varying properties of soils as well as its impact on constructions. Moreover, the conventional geotechnical tests taking the measurements such as global axial stress/strain, volumetric strains are implicitly assuming the testing sample as a homogeneous body. This simplification disregards local material heterogeneity and non-affine deformation patterns of natural sand, and yielded merely phenomenological evidence of global failure instead of physical process of particle-to-particle interactions (Andrade *et al.*, 2011).

To understand the mechanical behaviour of sand, one should realize the macro deformation is governed by failure mechanism at fine scales. Various experimental and numerical techniques have been developed to allow full-field measurement performed

on a deforming body. The foremost experimental investigation was carried out at Cambridge in 1960s. Roscoe (1970) used a 150kV X-ray apparatus to check the uniformity of the behaviour of soils at all stages of tests. The grain-scale density variation between localization zone and surrounding materials has been utilized in this sensing technique. Later from 1980s, several laboratories (Desrues, Lanier and Stutz, 1985; Desrues *et al.*, 1996; Alshibli *et al.*, 2000; Higo *et al.*, 2013) used X-ray tomography to study the localization patterns in sand. A special localization phenomenon, shear band, which encompass the major shear deformation of sand once it is fully formed, has drawn most attention in these research. The thickness, orientation, and volumetric behaviour of shear band have been of great interest among experimentalists since it is believed associated with governing failure mechanism in the post-peak regime (Desrues *et al.*, 1996). A further detailed exploration that can recognize particle morphology and interactions has been achieved by the advent of microscopic X-ray CT system (Oda and Kazama, 1998; Viggiani and Desrues, 2004; Alshibli and Alramahi, 2006), in-site X-ray scanning (Desrues *et al.*, 1996; Alshibli *et al.*, 2000), and ID-Track techniques (Hall *et al.*, 2010; Andò *et al.*, 2012). Overall, the X-ray method has been demonstrated as an effective tool to capture interaction maps and density variations in grain-scale. However, the technique limits resulted most tests performed over large increments, small specimens or large particle size. Note that strain bifurcation or the initial location is considered over very small strain step, hence low sampling frequency would tend to average instantaneous strain fluctuations over the

whole increment, and as a consequence the characterization of competing localization effects over a small period is difficult to carry out.

Digital Image Correlation (DIC) as a non-destructive, optical experimental technique has been extensively used over the last two decades. It analysis the surface displacement field from digital images taken from a process of interest, from which the overlapping subsets of pixels are tracked and meso-scale (soil clusters) displacements can be deduced (Sutton, Orteu and Schreier, 2009). Since the formation and collapse of 'soil particle columns', often referred as force chains, have been regarded as a signature mechanical phenomenon within the localization areas (Oda and Kazama, 1998), the meso-scale is deemed suitable for presenting local displacement field of soil tests (Rechenmacher, 2006). The yielded spatio-temporal nominally continuous observations also provide great opportunity to assess the onset and evolution of kinematic phenomena within the shear bands. Rechenmacher and her co-workers (2010, 2011, and 2012) used DIC method to evaluate shear, rotational and volumetric strains, build-up and collapse of force chains, as well as vortex structures during a plane strain compression test. In addition, the introduction of multiple cameras for DIC system (i.e., 3D DIC) makes it possible to perceive 3D surface deformation, and has been used for the description of 3D displacement field and calibration of constitutive parameters of a heterogeneous model (Rechenmacher and Medina-cetina, 2007; Medina-Cetina and Rechenmacher, 2010).

Although the advances in sensing technology have been improving our understanding of soil mechanism from micro- to macro-scales, the lack of statistical characterization of full field measurements is observed among current research

community. This knowledge gap is critical since non-unique material response have been reported (Song, 2012) and should be common due to various participating sources of uncertainty. The nature material heterogeneity, variation of testing apparatus, or human induced error can all exert certain amount of influence on the assessment result. The uncertainty may be also varying in space and time, and show distinct features when examined in different scales. In order to tackle this issue, a response population that sufficient to represent stochastic properties of physical process represents as a prerequisite before any serious characterization is about to make.

It is also worth noting that despite the rapid growth of 3D DIC technique, limited studies have been seen to correlate the displacement fields with kinematic operators (translation, rotation, expansion/contraction, etc.) under three-dimensional stress conditions. The technique difficulty lies in the internal measurements, which is necessary for quantifying motions of 3D object, is unable to be sampled by current digital images. Further, the choice of a proper coordinate system also represents a challenge. Because the sampled data by 3D DIC are displacements occurred to 'soil clusters' (i.e., in meso-scale) manifested on curvilinear spatial coordinates (non-rectangular layout). The previously adopted Spherical or Cartesian coordinates (Alshibli and Alramahi, 2006; Rechenmacher, 2006) cannot correctly accommodate the present specimen shape and show meso-scale kinematics without projecting to a rectangular plane. It is clear a systematic approach to account for 3D meso-scale kinematics under triaxial experimental conditions is still lacking.

In this work, we conduct a comprehensive statistical characterization towards a data ensemble populated from a series of nominally identical triaxial tests. First- and second-order statistics are calculated in a multi-scale framework. Following this, a complete set of first-order 3D kinematic operators under Cylindrical coordinates is introduced, and incorporated into the analysis of spatio-temporal evolution of kinematic behaviour of specimens under varying experimental conditions. Further, we perform again the statistical characterization towards kinematic fields generated from nominally similar tests, to reveal the prevailing localization mode among various competing ones, as well as uncertainty levels evolved in space and time.

The last chapter of this work is a separate research regarding probabilistic calibration of a visco-elastoplastic model. We incorporate this study for the aim of presenting the probabilistic calibration methodology that will be used to quantify the uncertainty and model performance to reproduce the heterogeneous material responses. The ultimate goal is to provide the full probabilistic description of spatially distributed constitutive parameters, and their dependencies in capturing stochastic behaviour of soil failure process.

1.2. Dissertation outline

Although the content of this dissertation is around the same topic, each chapter represents an independent journal article consisting of introduction, methodology, results and conclusion parts. Chapter 2 introduces the spatio-temporal statistical characterization of displacement fields in a multi-dimensional context. First- and second-order statistics are calculated for each data scenario. Chapter 3 introduces the 3D

kinematic operators under Cylindrical coordinates, and its application to 3D displacement fields captured on different triaxial compression tests. Chapter 4 further conducts the kinematic analysis but on a series of nominally similar tests, then mean and standard deviations are calculated across all participating tests. Chapter 5 introduces a Bayesian probabilistic calibration of a visco-elastoplastic model representing the rheological property of sandstone, to provide the methodology of uncertainty quantification that will be used in our future work of sand specimens.

1.3. References

Abedi, S., Rechenmacher, A. L. and Orlando, A. D. (2012) 'Vortex formation and dissolution in sheared sands', *Granular Matter*, 14(6), pp. 695–705. doi: 10.1007/s10035-012-0369-5.

Alshibli, K. A. *et al.* (2000) 'Assessment of Localized Deformations in Sand Using X-ray Computed Tomography', *ASTM Geotechnical Testing Journal*, 23(3), pp. 274–299.

Alshibli, K. A. and Alramahi, B. A. (2006) 'Microscopic Evaluation of Strain Distribution in Granular Materials during Shear', *Journal of Geotechnical and Geoenvironmental Engineering*, 132(1), pp. 80–91. doi: 10.1061/(ASCE)1090-0241(2006)132:1(80).

Andò, E. *et al.* (2012) 'Grain-scale experimental investigation of localised deformation in sand: A discrete particle tracking approach', *Acta Geotechnica*, 7(1), pp. 1–13. doi: 10.1007/s11440-011-0151-6.

Andrade, J. E. *et al.* (2011) 'Multiscale modeling and characterization of granular

matter: from grain kinematics to continuum mechanics', *Journal of the Mechanics and Physics of Solids*. Elsevier, 59(2), pp. 237–250.

Desrues, J. *et al.* (1996) 'Void ratio evolution inside shear bands in triaxial sand specimens studied by computed tomography', *Géotechnique*, 46(3), pp. 529–546. doi: 10.1680/geot.1996.46.3.529.

Desrues, J., Lanier, J. and Stutz, P. (1985) 'Localization of the deformation in tests on sand sample', *Engineering Fracture Mechanics*, 21(4), pp. 909–921. doi: 10.1016/0013-7944(85)90097-9.

Hall, S. A. *et al.* (2010) 'Discrete and continuum analysis of localised deformation in sand using X-ray μCT and volumetric digital image correlation', *Géotechnique*, 60(5), pp. 315–322. doi: 10.1680/geot.2010.60.5.315.

Higo, Y. *et al.* (2013) 'Investigation of localized deformation in partially saturated sand under triaxial compression using microfocus X-ray CT with digital image correlation', *Soils and Foundations*. Elsevier, 53(2), pp. 181–198. doi: 10.1016/j.sandf.2013.02.001.

Lacasse, S. and Nadim, F. (1996) 'Uncertainties in characterising soil properties', in *Uncertainty in the geologic environment: From theory to practice*, pp. 49–75. ASCE, New York.

Li, J. H. *et al.* (2014) 'Spatial variability of the soil at the Ballina National Field Test Facility', *Australian Geomechanics*, 49(4), pp. 41–48.

Medina-Cetina, Z. and Rechenmacher, A. (2010) 'Influence of boundary conditions, specimen geometry and material heterogeneity on model calibration from triaxial

tests', *International Journal for Numerical and Analytical Methods in Geomechanics*, 34(6), pp. 627–643. doi: 10.1002/nag.833.

Oda, M. and Kazama, H. (1998) 'Microstructure of shear bands and its relation to the mechanisms of dilatancy and failure of dense granular soils', *Géotechnique*, 48(4), pp. 465–481. doi: 10.1680/geot.1998.48.4.465.

Phoon, K.-K. and Kulhawy, F. H. (1999) 'Characterization of geotechnical variability', *Canadian Geotechnical Journal*. NRC Research Press, 36(4), pp. 612–624.

Rechenmacher, A., Abedi S. and Chupin, O. (2010) 'Evolution of force chains in shear bands in sands', *Géotechnique*, 60(5), pp. 343–351. doi: 10.1680/geot.2010.60.5.343.

Rechenmacher, A. L. (2006) 'Grain-scale processes governing shear band initiation and evolution in sands', *Journal of the Mechanics and Physics of Solids*, 54(1), pp. 22–45. doi: 10.1016/j.jmps.2005.08.009.

Rechenmacher, A. L. *et al.* (2011) 'Characterization of mesoscale instabilities in localized granular shear using digital image correlation', *Acta Geotechnica*, 6(4), pp. 205–217. doi: 10.1007/s11440-011-0147-2.

Rechenmacher, A. L. and Medina-cetina, Z. (2007) 'Calibration of soil constitutive models with spatially varying parameters', *Journal of Geotechnical and Geoenvironmental Engineering*, 133(12), pp. 1567–1576. doi: 10.1061/(ASCE)1090-0241(2007)133:12(1567).

Roscoe, K. H. (1970) 'The Influence of Strains in Soil Mechanics', *Géotechnique*, 20(2), pp. 129–170. doi: 10.1680/geot.1970.20.2.129.

Song, A. (2012) *Deformation analysis of sand specimens using 3D digital image correlation for the calibration of an elasto-plastic model*. PhD Dissertation. Texas A&M University, College Station, TX.

Sutton, M. A., Orteu, J. J. and Schreier, H. (2009) *Image Correlation for Shape, Motion and Deformation Measurements - Basic Concepts, Theory and Applications*. New York: Springer.

Viggiani, G. and Desrues, J. (2004) 'Experimental observation of shear banding in stiff clay', *Verlag Glückauf Essen*, pp. 649–658.

2. SPATIO-TEMPORAL STATISTICAL ANALYSIS OF BOUNDARY DISPLACEMENT FIELDS CAPTURED BY 3D DIGITAL IMAGE CORRELATION METHOD

2.1. Introduction

Nature soil in its complexity offers a wide range of variability and heterogeneity of stratigraphy and material properties, this essential stochastic being complicated each geotechnical task with finite amount of uncertainty. For instance, in a typical laboratory triaxial compression test of soil, various failure modes can be observed among parallel groups even though experimenting process has been carefully controlled (Desrues and Viggiani, 2004; Song, 2012). The observed uncertainty may arise from inherent heterogeneity of material, variations associated with testing apparatus, human introduced errors, or a combination of those. This non-uniqueness behavior poses a challenge to anyone who intend to comprehend the underlying failure mechanism, and introduces several questions such as: "which failure mechanism is dominating, or most likely to occur?" Or, "What is the correlation amidst varying failure modes, and mechanisms evolved in the space and time?" For a systematic characterization of uncertainty associated with the process of interest, a statistical description is not only desirable but necessary complement to the conventional analysis methods.

In order to understand the failure mechanism of soil material, one should recognize the continuum failure initiates from local material anomalies as fine as grain scale. However, in tradition plane or triaxial compression test, materials are collectively

considered as a homogeneous body-only global, averaged material responses are obtained. To proper characterize the heterogeneous deformation of granular material, full field measurement of testing specimen is necessary. The foremost experimental effort conducted can be traced back as early as 1960s. Roscoe (1970) firstly used a 150 kV X-ray apparatus to check the non-uniform behaviour of specimens. Starting from 1980s, Desrues and his co-workers (Desrues, Lanier and Stutz, 1985; Desrues *et al.*, 1996) used X-ray tomography to investigate strain localization patterns in sand, including orientation, thickness, and volumetric behaviour, etc. A further observation of microstructure and evolving mechanism inside of shear band has been achieved by the advent of microfocus X-ray CT system (Oda and Kazama, 1998; Oda, Takemura and Takahashi, 2004). These studies provide valuable insights towards showing particle interaction maps and density variations happened to specimen. Nevertheless, limitations in data acquisition resources have led to mainly post-mortem analysis or data captured over wide strain increments. This could smear out chronologically occurred localized strain over each short period of time, and resulted strain localizations may appear simultaneously in all regions (Desrues and Viggiani, 2004). One improved solution is to perform in-situ X-ray scanning during the course of loading (Desrues *et al.*, 1996; Alshibli *et al.*, 2000). More recent studies had even incorporated particle identification and tracking algorithms to assess the link between grain morphology and localization effects (Matsushima *et al.*, 2006; Andò *et al.*, 2012; Alshibli *et al.*, 2016). However, the computational effort is proved expensive, and bifurcation initiates over a very small strain increments is still difficult to characterize.

Over the last two decades, Digital Image Correlation (DIC) has been extensively used as an alternative reliable experimental technique for non-destructive full-field measurements. It is essential a computational tool assessing consecutive digital images taken from a process of interest, from which meso- or micro-scale displacements can be deduced (Sutton, Orteu and Schreier, 2009). In terms of its application in soil mechanics, Rechenmacher and Medina-Cetina (2003, 2006) inferred thickness and inclination of shear band through direct delineation of grain-scale displacement fields within deforming sand specimens captured by 3D DIC. These approximate spatial-temporal continuous observations also provide opportunities to elucidate kinematic behaviour associated within shear bands (Abedi, 2012; Omidvar, Chen and Iskander, 2015), and evolution of force chains and vortex-structures through the course of specimen deformation (Rechenmacher, Abedi S. and Chupin, 2010; Rechenmacher *et al.*, 2011). Note that the current DIC technique used for boundary displacement measurements only availed 2D kinematic analysis, which disregards out of plane translation or rotation.

In spite of rapid proliferation of experimental techniques and processing skills as introduced above, the study accounts for uncertainty associated with failure modes, and a statistical characterization of soil deformation patterns are lacking in present research. As we mentioned previously, soil is heterogeneity in its nature, non-unique soil failure mechanisms should be expected for any research considering local heterogeneity of material, contrary to otherwise homogeneous assumptions. Further, in order to avoid the disadvantage of "can't see the forest for the trees", a multi-level inspection of deformation process is also preferred. Based on these concerns, the present paper use the

3D DIC technique to populate database from a series of nominally identical triaxial compression specimens. Then, the datasets were processed into "0D-T" data ensemble (axial stress-strain and axial strain-volumetric strain), 1D-T data ensemble (boundary vertical and radial displacements), and 3D-T data ensemble (either in Cartesian or Cylindrical coodinates). First- (mean and standard deviation analysis) and second-order statistics (correlation analysis) are calculated on each case, and the results were served to provide the insights of spatio-temporal deformation trend and dependencies of axisymmetric specimen under triaxial compression condition, in a spatio-temporal fashion.

The paper is organized in three main parts: firstly, we give a brief account of laboratory experiments, comprised of triaxial compression tests coupling with 3D DIC technique. In following sections, multi-dimensional data ensembles (0D-T, 1D-T, and 3D-T) were sequentially introduced and analysed through first- and second-order statistics. Finally, the paper is concluded according to obtained statistical results, as well as its interpretations in regards to uncertainty and associations among different failure modes during soil failure process, which reflects our exact intention to address the questions proposed at the beginning.

2.2. Laboratory experiments

2.2.1. Triaxial compression test

Experimental results presented in this study come from a series of drained, vacuum-consolidated triaxial compression tests carried out at the John Hopkins University. Sieved construction sand ($G_s = 2.63, D_{50} = 0.50mm, C_u = 2.34$ and $C_c = 1.11$),

graded as SP, was selected to reconstitute sand specimen owing to its color spectrum appropriate for pattern recognition during DIC analysis. Table 2.1 gives sample characteristics of 17 selected nominally similar tests in terms of aspect ratio, initial density, relative density, friction angle, and stress ratio at peak state. Most specimens were constituted through vibratory compaction in three uniformly compacting layers; 4 additional ones were prepared using dry pluviation by controlling drop height to reach the similar initial density.

Table 2.1 Summary of sample characteristics of 17 tests

Test name	Aspect ratio	Initial density (kg/m^3)	Relative density (%)	Friction angle (deg)	Peak (σ_1'/σ_3')	Sample preparation
092903b	2.18	1,710.95	91.09	49.51	7.35	Vibratory compaction
093003b	2.19	1,696.00	85.96	47.98	6.78	Vibratory compaction
100103a	2.21	1,702.22	88.10	48.66	7.03	Vibratory compaction
100103b	2.19	1,717.13	93.18	47.96	6.77	Vibratory compaction
100103d	2.18	1,702.41	88.17	47.37	6.57	Vibratory compaction
100203a	2.20	1,715.32	92.57	48.90	7.12	Vibratory compaction
100203b	2.17	1,711.91	91.41	47.96	6.77	Vibratory compaction
100303b	2.22	1,718.70	93.71	48.56	6.98	Vibratory compaction
120604c	2.25	1,717.48	93.30	48.89	7.11	Vibratory compaction
120904b	2.25	1,720.40	94.28	48.76	5.86	Vibratory compaction
120904c	2.25	1,713.13	91.83	48.77	5.86	Vibratory compaction

Table 2.1 Continued

Test name	Aspect ratio	Initial density (kg/m^3)	Relative density (%)	Friction angle (deg)	Peak (σ_1'/σ_3')	Sample preparation
120904d	2.24	1,707.89	90.04	47.68	5.44	Vibratory compaction
120904e	2.25	1,718.70	93.71	47.79	5.51	Vibratory compaction
101204a	2.24	1,708.03	90.09	48.03	6.89	Dry pluviation
120604a	2.23	1,721.06	94.50	49.46	7.33	Dry pluviation
120604b	2.25	1,715.13	92.50	48.54	6.98	Dry pluviation
121304a	2.24	1,721.73	94.73	49.30	7.27	Dry pluviation
Basic statistics						
Mean	2.22	1712.83	91.72	48.48	6.68	-
Standard deviation	0.03	7.20	2.45	0.62	0.61	-

The triaxial apparatus is practically similar to the conventional system, except Plexiglas cell was removed and specimen was subjected to a 40KPa confinement by making use of vacuum pump. This apart from conventional settings was designed for avoiding optical distortion which could occur to digital images that were taken during the course of shearing. All specimens were compressed under a strain control rate of 0.2%/min until critical state was ensured reached (beyond 12% of strain level). Figure 2.1 presents the global stress-strain and volumetric strain responses of 17 tests, variations are seen gradually emerged after elastic portion. However, in post-peak regime, data variability seems homoscedastic for stress-strain curves (Figure 2.1(a)), while continuing scattering for the other case (Figure 2.1(b)). A further investigation of bifurcating process and post-peak behavior will require a detailed description of full

field displacement, and a statistical inspection that is capable to assess the uncertainty inherent in the process of interest.

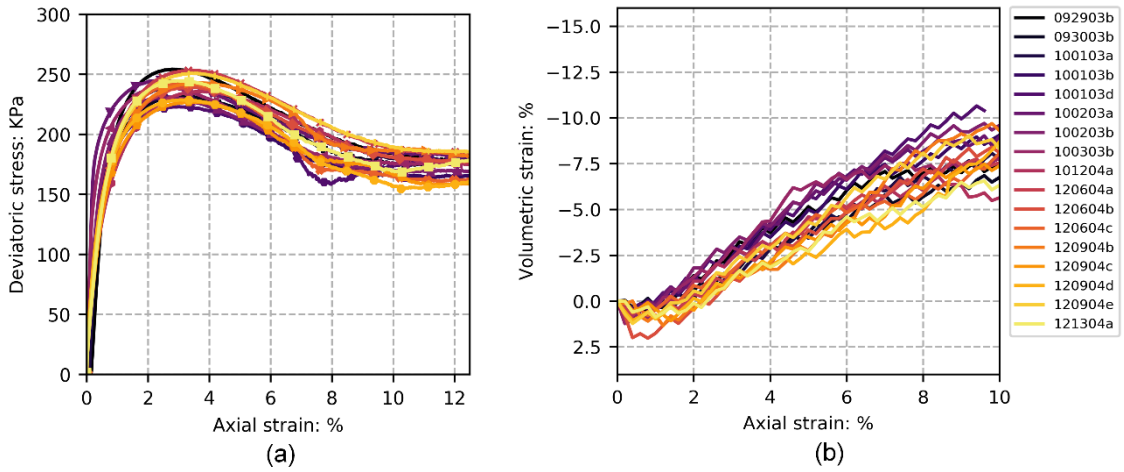

Figure 2.1 (a) Triaxial stress-strain curves of 17 tests; (b) axial strain-volumetric strain curves of 17 tests

2.2.2. 3D DIC

In present study, we use *3D DIC* technique to populate boundary displacement field during the course of shearing of 17 testing specimens. The full details of using 3D DIC technique to sample full field spatio-temporal datasets can be found in Medina-Cetina (2006). Herein, we only review the most relevant sections regarding the analysis. Along with standard triaxial compression test, a 3D imaging system comprised two digital cameras were setup in front of soil specimen to provide access to 3D surface data throughout all compression processes. Synchronous images were captured every 15s (0.05% of axial strain) and digitalized through software VIC-Snap, by Correlated Solutions, Inc. To assimilate graphical information into full-field displacements, subsets

of pixels between two digital images were identified and correlated, through the algorithm such as normalized cross-correlation that is adopted in this study (Sutton, Orteu and Schreier, 2009). This will generate a batch of incremental (Eulerian) DIC displacement data. For accommodating Lagrangian-based strain and kinematic analysis mapping from undeformed to deformed state of specimen, consecutive image increments were accumulated through cubic spline interpolation referenced at the initial material coordinates. The resulted description of full-field displacements featured with a grain-scale resolution of 0.4mm, over a sector approximate 85 degree around the specimen circumference.

Figure 2.2 gives an example of 3D DIC displacement fields superimposed over a specimen's deformed boundary shape, of test 092903b at strain level 7%. First row are measured 3D displacement field decomposed in Cartesian coordinates. From left to right are *u*, *v*, and *w* fields which represent local displacements in horizontal, vertical and out-of-plane directions, respectively. Asymmetric deformation in *u* field and budging phenomena described in *w* field indicate strain localization has well developed in specimen at present shear stage. The layered deformation in vertical direction implies specimen's varying density in depth which may be caused by preparation method (vibratory compaction in three layers).

Instead of analyzing in Cartesian system, displacement vectors can also be decomposed in other orthogonal systems. For instance, radial, tangential, and axial displacement fields can be obtained if analysis performed in Cylindrical coordinate. Figure 2.2(b) gives corresponding results in Cylindrical coordinates based on the same

DIC measurements presented in Figure 2.2(a). Radial displacement as shown in the first plot demonstrates sample is mainly expanding in the middle and less evident towards two ends of the specimen. The second plot presents tangential displacement field indicating angular motion of subsets along specimen surface. Negative quantities denote clockwise rotations, which presented mainly in the middle height of specimen and following main diagonal direction (top-left to bottom-right). This associates well with intense particle rotation inside of shear band was previously found during softening stage (Oda and Iwashita, 2000). Note that the observations herein are merely depend on measurements obtained from one test and one specific loading stage. A proper characterization of behavior will require a statistical database, to present full populations of the process.

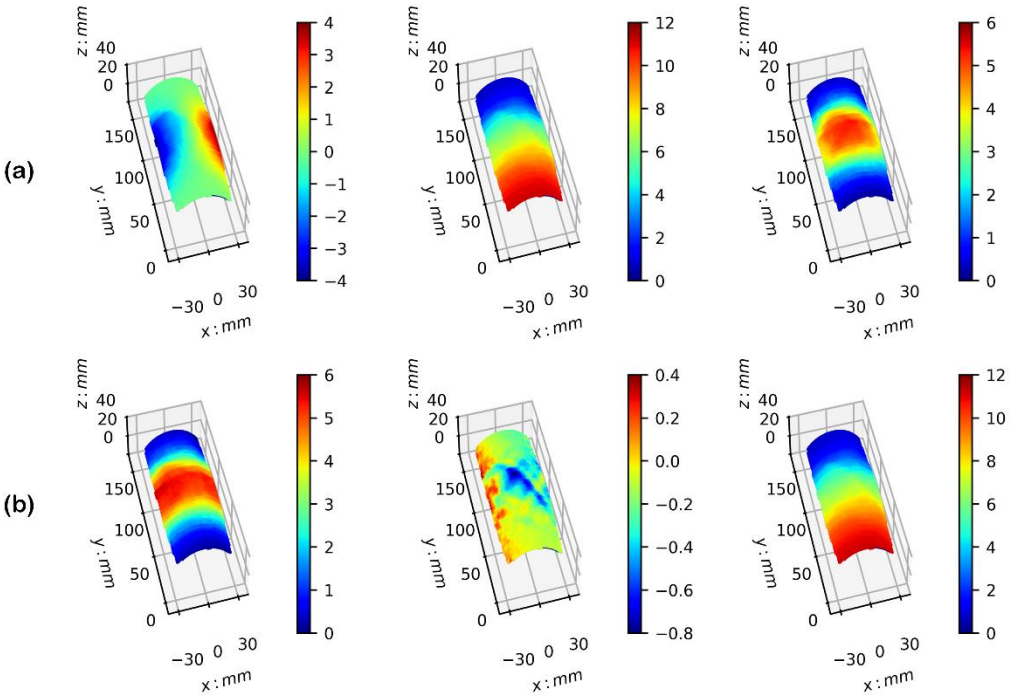

Figure 2.2 (a) 3D displacement field of test 092903b at strain level 7% decompose into in horizontal, vertical and out-of-plane directions (left to right); (b) Same displacement field decompose into radial, tangential, and axial directions in Cylindrical coordinate

2.3. Statistical characterization of multi-scale data ensembles

2.3.1. '0D-T' data assembling

Our first analyzing effort lies in statistical characterization of conventional global material responses, including axial stress-strain and axial strain-volumetric strain relationships. Due to the volumetric strain was not directly measured throughout the tests, an alternative method was employed to calculate sample volume by assuming specimen is composed of an assembly of 'stacked disks' (Macari, Parker and Costes, 1997). The height *H* is determined as 1mm for each disk, while the diameter is derived

based on averaged radius measurements *R* captured through *DIC* images along the specimen boundary. The specimen volume can then be integrated as the sum of all disks volume, i.e.,

$$V = \int_0^H \int_0^{2\pi} \int_0^R r dr d\theta dz = \pi \int_0^H R^2 dz \tag{2.1}$$

The global deviatoric stress and volumetric strain, as a function of axial strain for all tests, are depicted in Figure 2.3 (a) and (b), respectively. Selected axial strain range is from 0 to 9.6%, which in accordance with the maximum extent of sampled *DIC* data that is available for all tests. It shows in Figure 2.3 (a) that averaged stress response reached its peak at 3.2% of axial strain, with mean and standard deviation equal to 237.89 and 8.92KPa, respectively. After this clear peak, the variation of deviatoric stress shows constant behaviour through the critical state. In Figure 3 (b), global dilatancy is clearly seen after initial volumetric straining. Unlike the constant trend showed in Figure 2.3 (a), an increase of uncertainty can be observed with the progression of the tests. Several constitutive parameters can be deduced from this mean plot of processes, for instance, the mean of Poisson's ratio ν and dilation angle ψ were estimated as 0.123 and 22.62°, respectively.

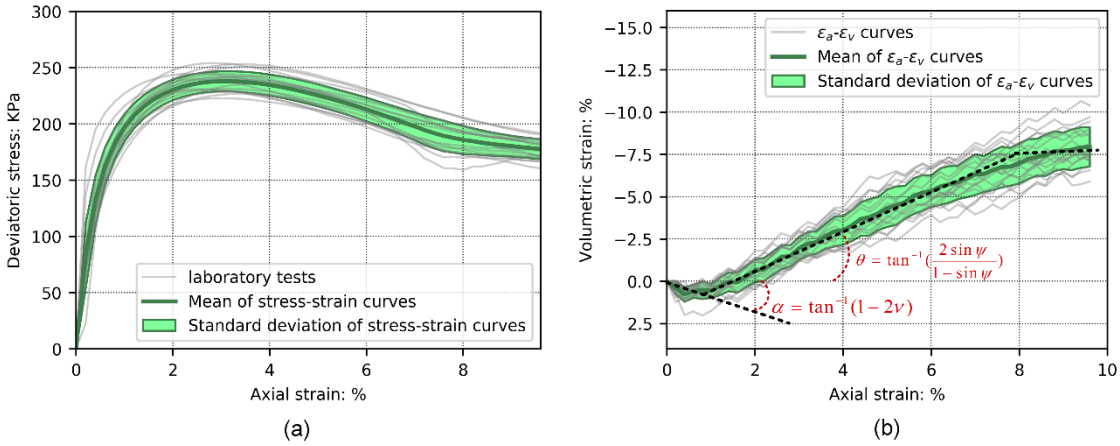

Figure 2.3 (a) First order statistics of stress-strain curves; (b) First order statistics of axial strain-volumetric strain curves

2.3.2. 1D-T data assembling

2.3.2.1. 1D-T vertical displacements

1D-T datasets herein refers to averaged vertical or radial displacement across specimen heights. Selected strain levels are from 0.0% to 9.6%, with 0.2% (1 minute) incremental steps. Figure 2.4 (a) presents 1D vertical displacements data ensembles at 4 loading stages – 0.8%, 3.2%, 7.0%, and 9.6%, representing states regarding hardening, peak, softening, and critical, respectively. Specimen height has been normalized based on initial sample geometry, where we abandoned the top 10% data due to several tests suffered from the loss of material coordinates close to the critical state. Figure 2.4 (b) and (c) are first order statistics of datasets presented in Figure 2.4 (a). After the peak ($\varepsilon_a = 3.2\%$), specimen is seen deformed non-linearly in the vertical direction as shown in Figure 2.4 (b). The bottom portion, nearly 20% of specimen height, soil exhibit somewhat homogeneous upward displacement. This "rigid body movement" can be

associated with relatively high density at the bottom, and the region separated from shearing and bulging plane developed primarily in the middle of specimen. Above this area, deforming presents with a linear decreasing trend which is believed to coincide with expansion band. The end of this portion is then connected with a non-linear zone, where displacement is gradually curve into zero at the top. Note that all testing specimens have been fixed at the top and loaded with the same strain rate from the bottom, it explains why uncertainty is small when it approaches to both ends, and the standard deviation (Figure 2.4 (c)) is seen mostly evident in the middle portion.

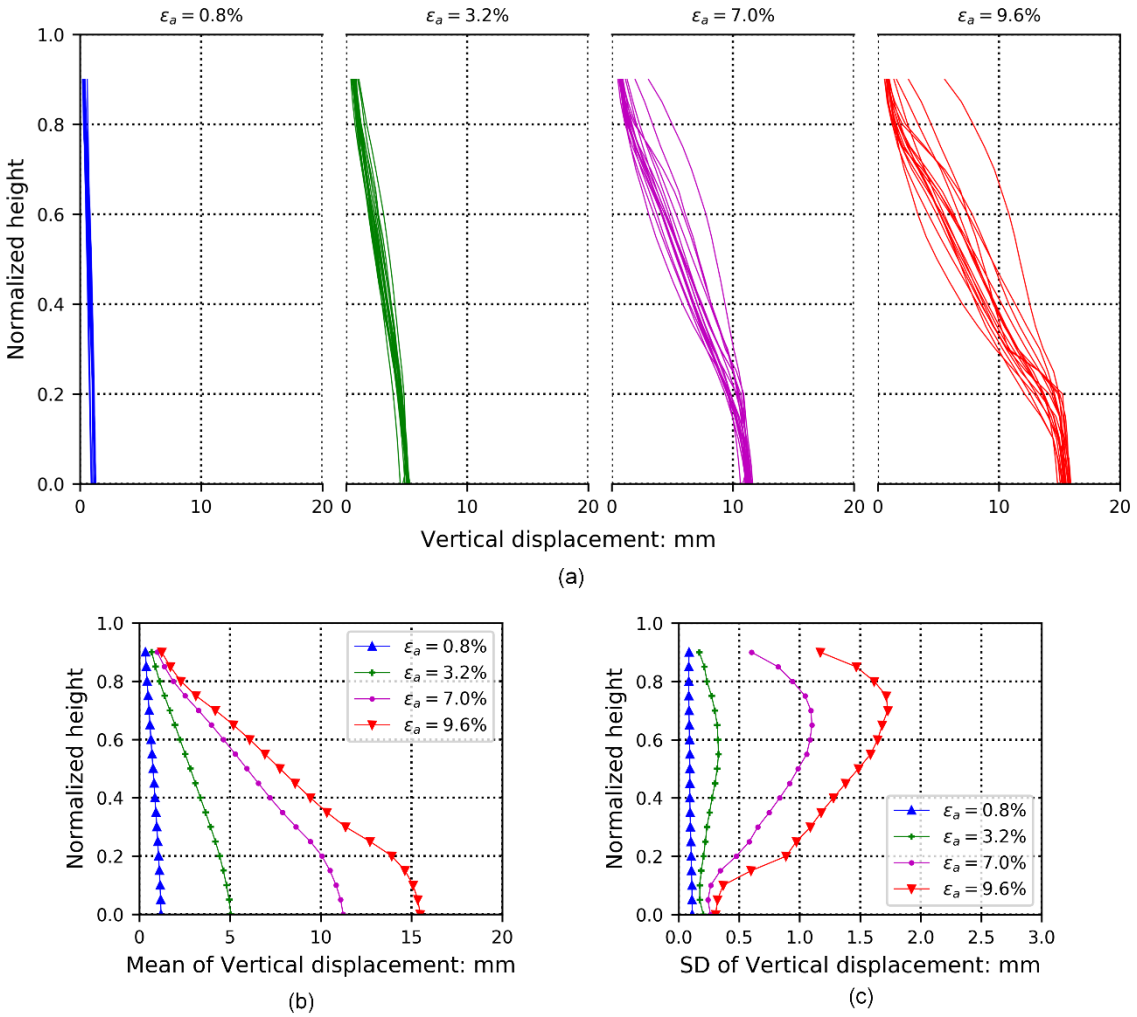

Figure 2.4 (a) 1D-T vertical data ensembles at 4 loading stages – 0.8%, 3.2%, 7.0%, and 9.6% of axial strain; (b) Mean of data ensembles; (c) Standard deviation of data ensembles

Further, correlation analysis (second order statistics) are performed on the same data ensembles aiming at revealing spatio-temporal dependencies of local displacements. We use classical Pearson correlation coefficient to index this relationship, i.e.,

$$\rho(k) = \frac{\sum_{i=1}^{N}(x_i - \bar{x})(y_{(i+k)} - \overline{y_{(i+k)}})}{\sqrt{\sum_{i=1}^{N}(x_i - \bar{x})^2}\sqrt{\sum_{i=1}^{N}(y_{(i+k)} - \overline{y_{(i+k)}})^2}} \tag{2.2}$$

Where x_i and $y_{(i+k)}$ are two random variables, and k represent lags between x_i and $y_{(i+k)}$, which can be defined in space or time. Figure 2.5 (a) and (b) offer two illustrating cases for auto- and cross-correlation calculations. "Cross" herein denotes correlations are computed based on displacement fields obtained at different loading stages, namely, time lags $\delta_t \neq 0\,\text{min}$. In the situation that first random variable is lagging behind second in space, as case highlighted by red triangles in Figure 2.5 (a), spatial lag δ_{ynorm} would be positive. Otherwise spatial lag δ_{ynorm} can be negative for instance showcased by blue squares. For auto-correlation, the generated correlation coefficients must be symmetric with respect to axis $\delta_{ynorm} = 0$, due to the identical data ensembles are used for computing correlations. But this is not hold for cross-correlation cases because different data ensembles are presented as shown in Figure 2.5 (b).

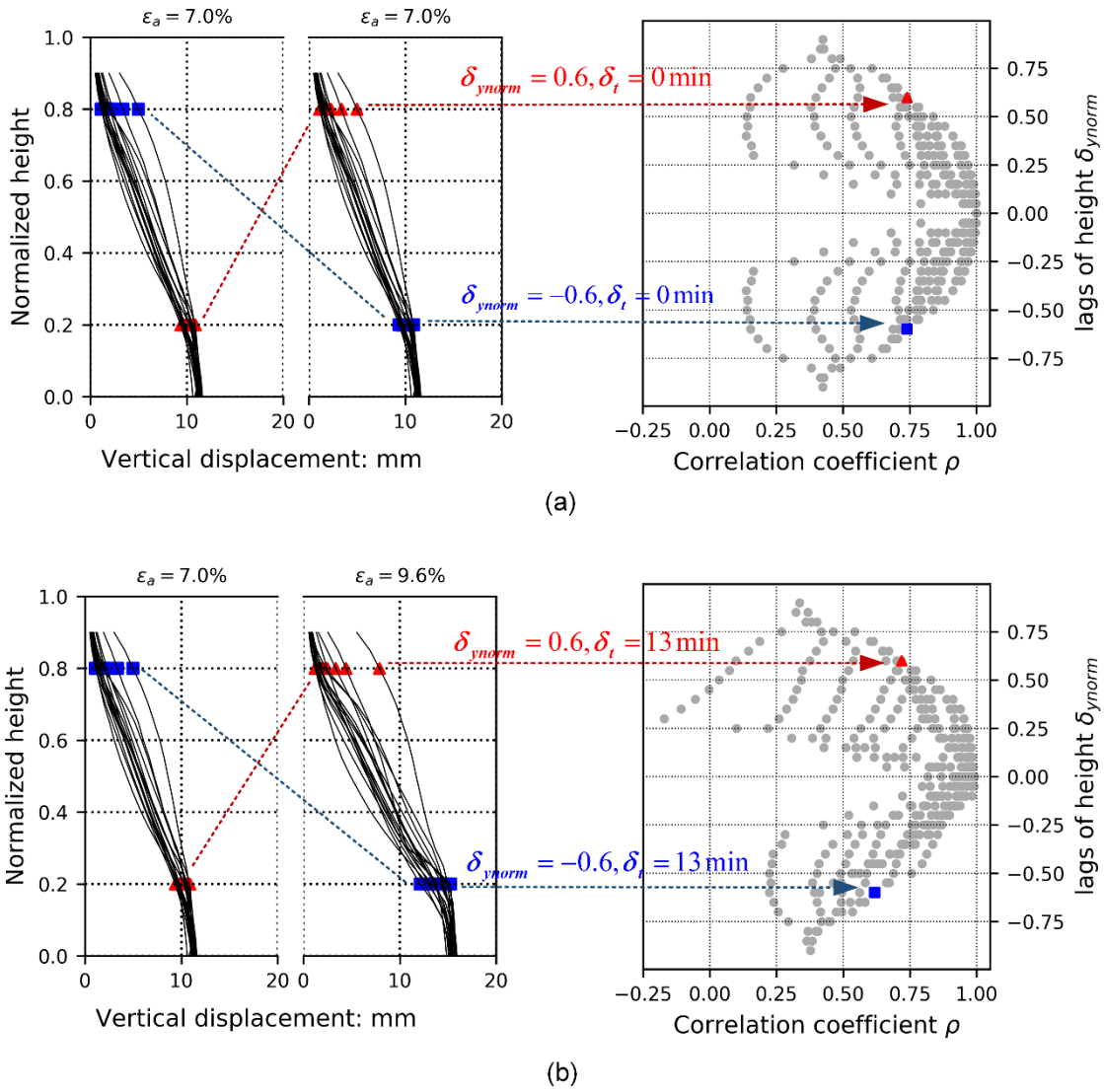

Figure 2.5 Illustrative cases of computing correlation coefficients towards 1D-T vertical displacement field: (a) auto-correlation coefficient versus lags of height δ_{ynorm} ; (b) cross-correlation coefficient versus lags of height δ_{ynorm}

For the aim of obtaining the whole picture of correlation relationships in space and time, we calculated completely 48 stages correlation fields. A surface is then searched through cubic spline interpolation trying to best fit all coefficient clouds, as

shown in Figure 2.6. *X* and *Y* axes represent temporal and spatial lags, and the colours indicate the intensity of correlations. It follows the approximate symmetric shape as we have seen in Figure 2.5. However, a downward skewness is gradually emerged beyond 10 minutes in time lag (equals to $\Delta\varepsilon_a = 2\%$). It can be interpreted physically, that a significant upper part displacement at early stage tends to positively associate with considerable lower part displacement if two phases apart at least 10 minutes. This quantitative conclusion is likely a consequence of porosity change in local areas of specimen during the tests. Because our testing specimens are all presented with high relative density (as shown in Table 2.1), local dilations should be evident inside of expansion band. Such behaviour can supposedly provide the accommodating ability of significant lower portion movement at later stages.

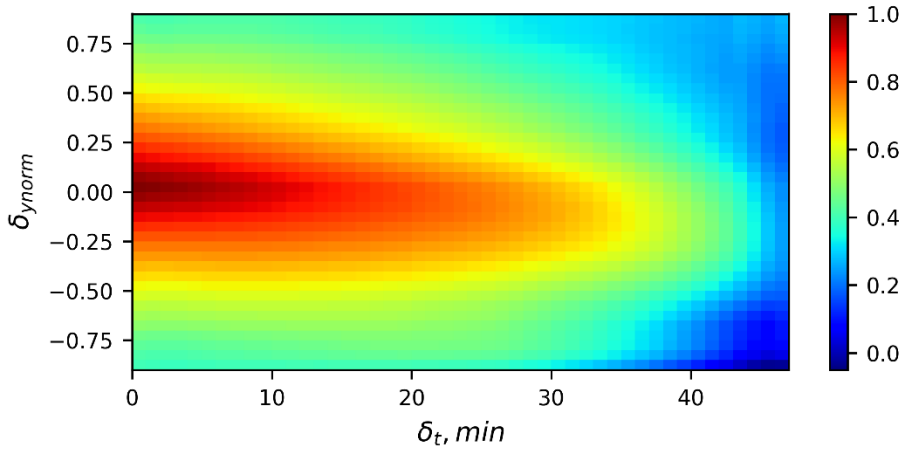

Figure 2.6 Spatio-temporal empirical correlation map of 1D-T vertical data ensemble

2.3.2.2. 1D-T radial displacement

1D-T radial displacement is mainly indicative of specimen's bulging effect. Figure 2.7 (a) and (b) show the anticipated deforming pattern that the magnitude of expansion is most evident about the middle of specimen. However, in Figure 2.7 (c), the higher uncertainty areas are seen located approximately 0.3 and 0.8 of normalized specimen height. This is also reflected on heterogeneous data ensembles in the last sub-plot of Figure 2.7 (a). Even though most tests reach the local maximums about the same height of specimen, various decline gradients are observed towards the upper and bottom limits of specimen, suggesting that variability of expanding profile, instead of maximum bulging point, is the main contributing source of uncertainty at this stage of loading.

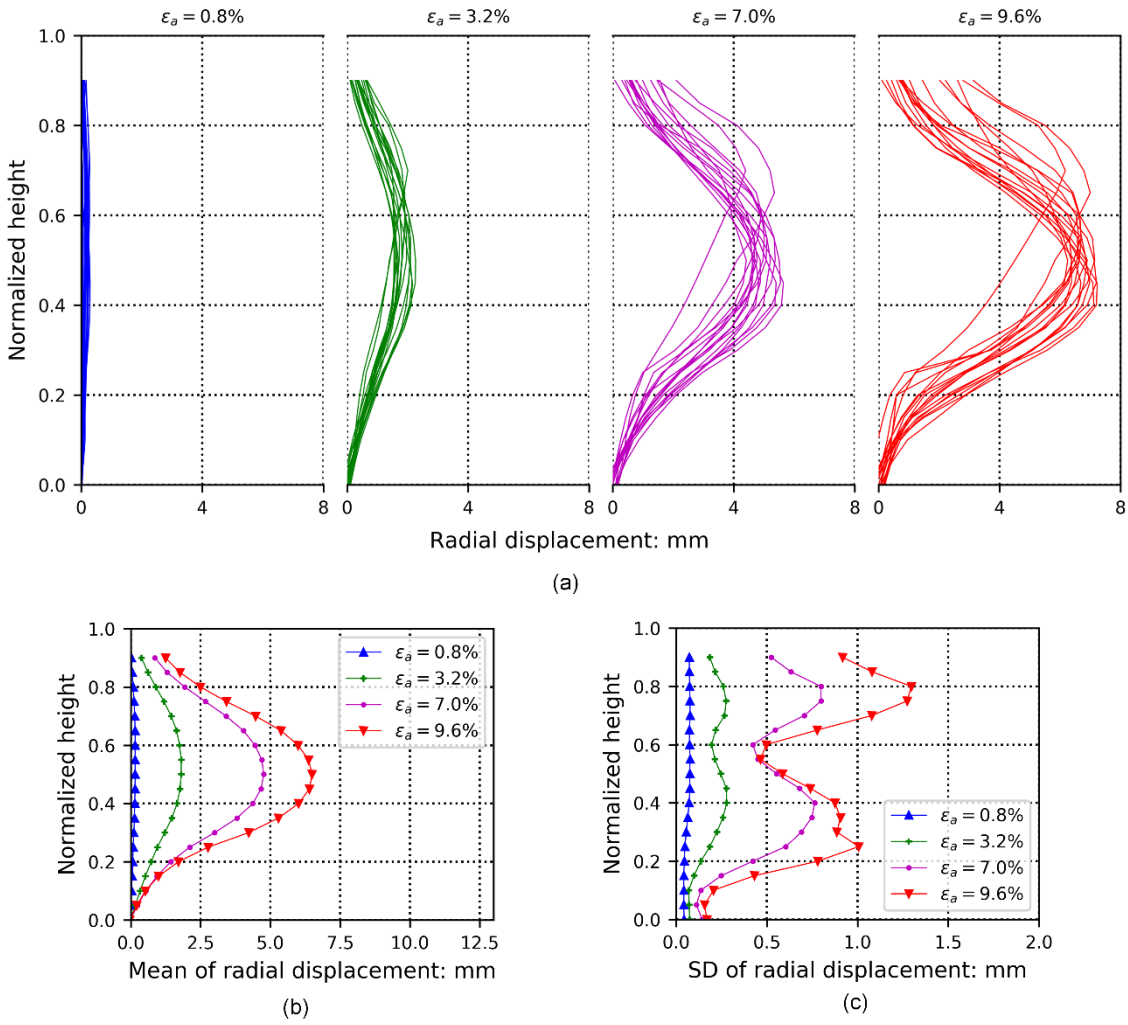

Figure 2.7 (a) 1D-T radial data ensembles at 4 loading stages – 0.8%, 3.2%, 7.0%, and 9.6% of axial strain; (b) Mean of data ensembles; (c) Standard deviation of data ensembles

Figure 2.8 shows the spatio-temporal correlation map generated in the same manner as that of Figure 2.6. Interestingly, negative correlation arise where $\delta_{ynorm} = \pm 0.5$, indicating a general opposite radial deforming trend if two random variables spacing around half of specimen height. Such pattern can be understood as, if loading energy is greatly mobilized due to large deformation in one area, local deformation would be less

significant in other areas, and consequently leads to non-erratic volume change in the global sense.

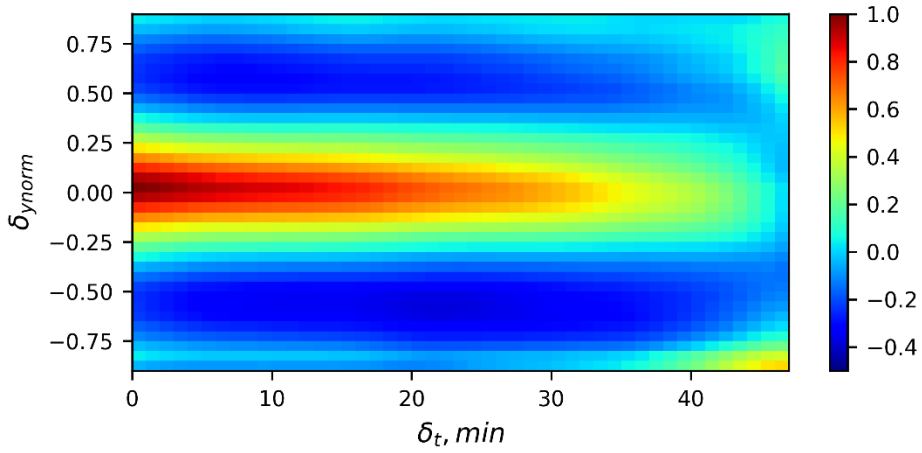

Figure 2.8 Spatio-temporal empirical correlation map of 1D-T radial data ensemble

2.3.3. 3D-T data assembling

3D-T data-sets consist of full-field spatio-temporal boundary displacement measurements by making use of 3D DIC technique. The raw data was processed through cubic spline interpolation on a prescribed mesh-grid for the sake of a consistent initial configuration (i.e., material coordinates) across all tests. In present research, we generated two 3D-T data ensembles from the identical set of digital image information, as shown in Figure 2.9 and 2.10, respectively. One is under the conventional Cartesian coordinates (named as 3D-T-Ca), another is processed through the Cylindrical coordinates (3D-T-Cy) which defines the analysing system consistent with specimen geometry. The comparative setting is intend to examine the first- and second-order statistics of 3D-T displacement fields from different perspectives, and the results are

anticipated to offer the insights of trend and variability of boundary deforming process, as well as local deformation dependencies characterized in space and time.

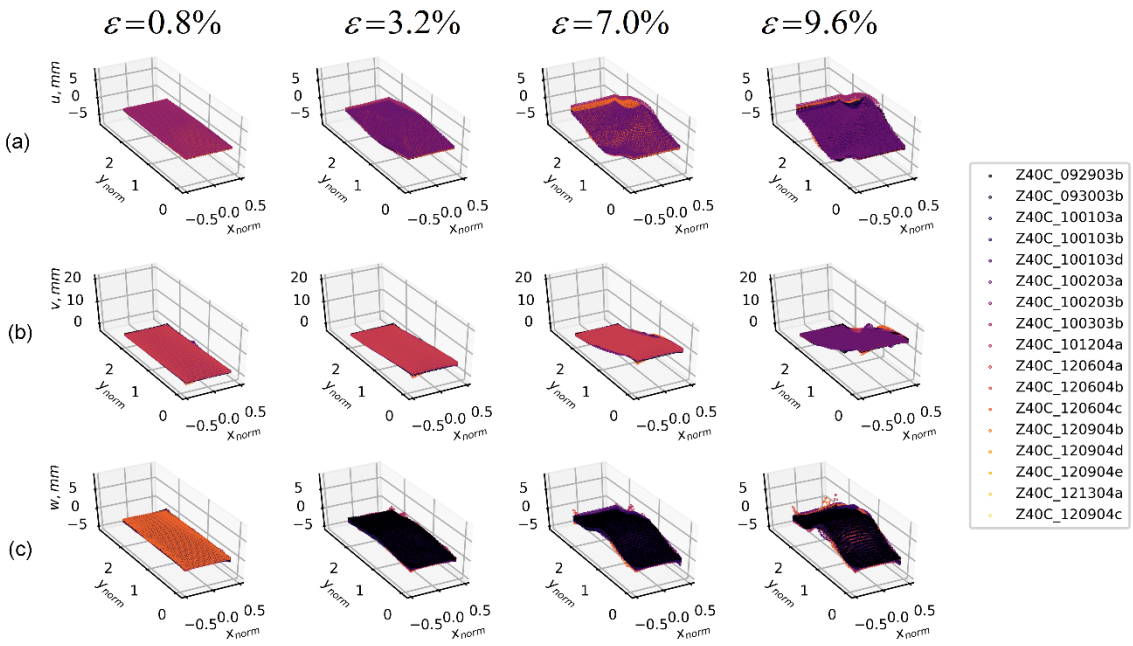

Figure 2.9 3D-T-Ca data ensembles: (a) u displacement data ensembles (horizontal) at 4 loading stages – 0.8%, 3.2%, 7.0%, and 9.6% of axial strain; (b) v displacement data ensembles (vertical); (c) w displacement data ensembles (out-of-plane)

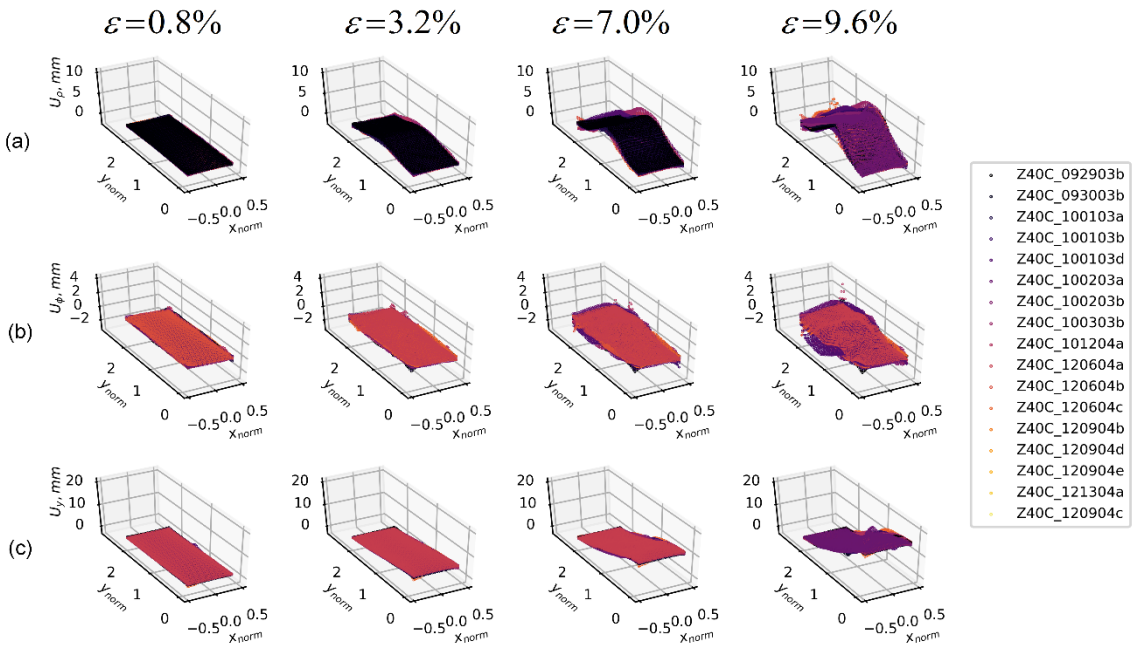

Figure 2.10 3D-T-Cy data ensembles: (a) U_ρ displacement data ensembles (radial) at 4 loading stages – 0.8%, 3.2%, 7.0%, and 9.6% of axial strain; (b) U_ϕ displacement data ensembles (tangential); (c) U_y displacement data ensembles (axial)

2.3.3.1. First order marginal statistics

Figure 2.11 and 2.12 represent mean and standard deviation fields of data ensembles presented in previous section. In these plots, each column defines a specific loading stage, while each row indicate either mean or standard deviation of a particular ensemble displacement field. In Figure 2.11, the mean plot of u fields show that specimen are primarily expanded in the middle which caused the material movement toward two opposite directions if viewed in horizontal plane. The mean surfaces of v displacement fields can well correspond to patterns seen in Figure 2.4 that three distinct 'moving blocks' started to form since 7.0% of axial strain. For the last loading phase

($\varepsilon_a = 9.6\%$), standard deviation are clearly seen more evident along the diagonal direction of the specimen surface, suggesting that uncertainty of vertical displacement could be a result of various banding mechanisms. Patterns in w field also reflect some similarities when compared to 1D-T data ensembles as presented in Figure 2.7. A clear bulging effect can be observed at the middle of specimen, however, again, the higher uncertainty regions are manifested at the places above and below the maximum bulging point, which demonstrate the bulging uncertainty are primarily influenced by the curvature of expanding profile, instead of relative position of maximum bulging point.

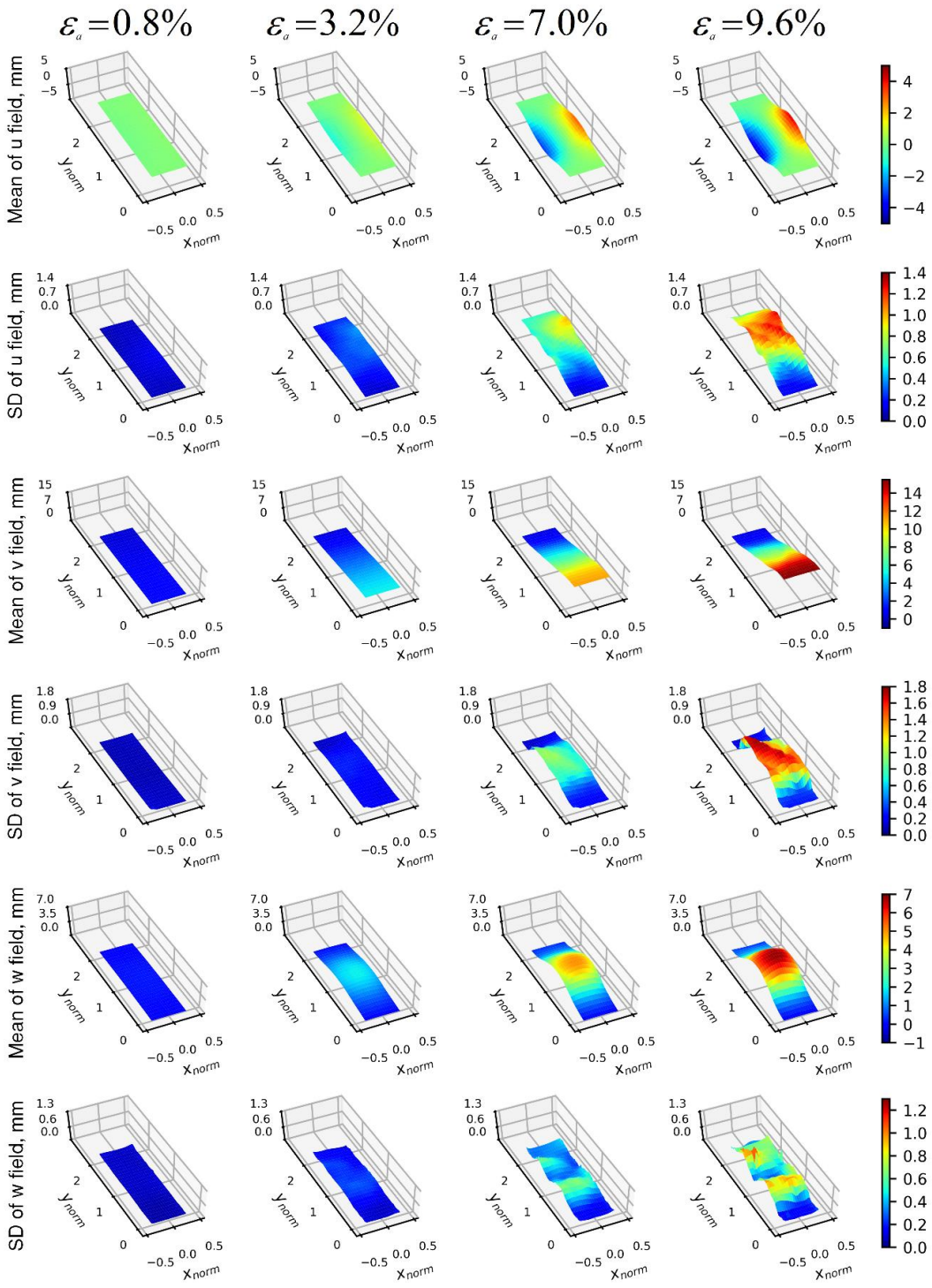

Figure 2.11 Mean and standard deviation distributions of 3D-T-Ca data ensembles, where column define each specific loading stage, and row denotes either mean or standard deviation of the data ensemble

Figure 2.12 presents analysing results of 3D-T-Cy data ensembles under the Cylindrical coordinates. Mean radial displacements, as shown in the first row, are most evident in the middle of specimen. However, the quantities are seen uniform across the same height of specimen, in contrast with bulging effect as depicted in the mean field of w fields. This is due to radial displacement reflects the part of displacement that would cause specimen's radius change, and such change as presented is constant along the same height of specimen. The mean field of U_ϕ (tangential displacement) indicates that following off-diagonal direction, the specimen surface tends to rotate counter-clockwise. This associates well with intense particle rolling inside of shear band which was reported through experimental or modelling studies (Oda and Iwashita, 2000; Rechenmacher, 2006). The uncertainty of tangential displacement field, contrarily, concentrate along a diagonal direction opposed to off-diagonal direction as manifested in the mean field of U_ϕ. Given only 6 out of 17 specimens were presented with diagonal shear bands at the end of the test, the highlighted diagonal uncertainty band may as a consequence of insufficient data regarding diagonal shear bands among all obtained testing results.

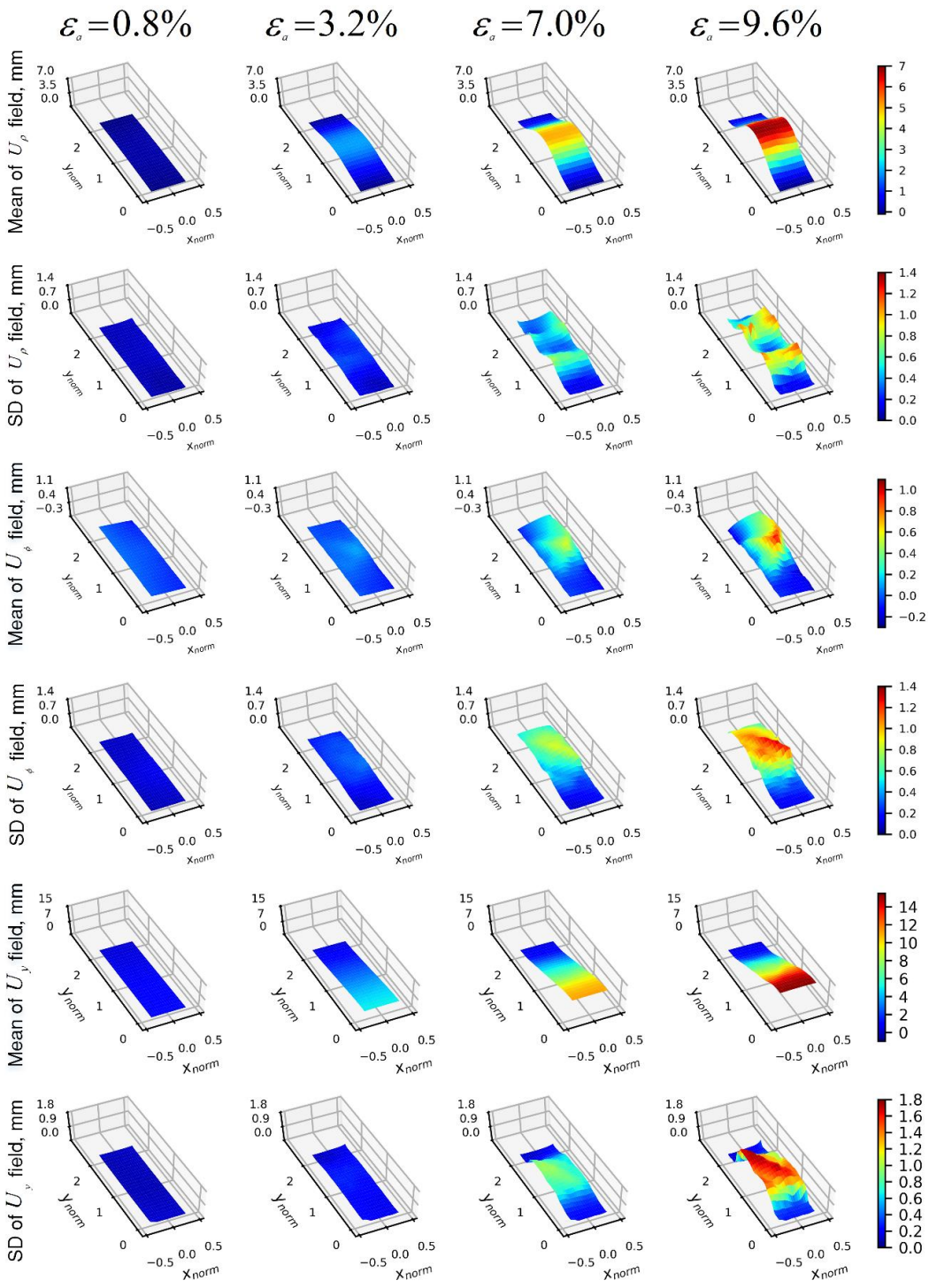

Figure 2.12 Mean and standard deviation distributions of 3D-T-Cy data ensembles, where column define each specific loading stage, and row denotes either mean or standard deviation of the data ensemble

2.3.3.2. Second order correlation statistics

For the calculation of empirical correlation structure of 3D-T displacement fields, we assume each coordinate p_i is a random variable defined in space and time $p_i = (x_{norm,i}, y_{norm,i}, t_i)$. Thereby, the computation of correlation coefficient becomes a function of spatio-temporal lag distance ($\delta_x, \delta_y, \delta_t$) between two random variables. The calculation of empirical covariance, for example in u displacement field, is defined as:

$$\begin{aligned} cov_u(p_1, p_2) &= E\{[u(p_1) - \bar{u}(p_1)][u(p_2) - \bar{u}(p_2)]\} \\ &= \frac{1}{N}\sum_{i=1}^{N}[u_i(p_1) - \bar{u}(p_1)][u_i(p_2) - \bar{u}(p_2)] \end{aligned} \tag{2.3}$$

Where p_1 and p_2 respectively represent two coordinates ($x_{norm,1}, y_{norm,1}, t_i$) and ($x_{norm,2}, y_{norm,2}, t_i$), u represents the data at point p_i, and $\bar{u}$ represents the data mean at point p_i. The empirical correlation coefficient is thus calculated as:

$$\rho_u(p_1, p_2) = \frac{cov_u(p_1, p_2)}{\sigma_u(p_1)\sigma_u(p_2)} \tag{2.4}$$

Where $\sigma_u(p_i)$ denotes the standard deviation of the samples at point p_i.

Figure 2.13 illustrates the process of computing spatio-temporal correlation coefficient from the 3D-T data ensembles, by taking the example of u displacement fields at two different deforming stages (7.0% and 9.6%). As shown in Figure 2.13 (a) and (c), we randomly select two example spatial variables *P1* and *P2* in two displacement fields, with each variable consists of 17 entries resulted from triaxial compression tests. The spatial lags $\delta_{xnorm} = -0.475$ and $\delta_{ynorm} = -1.042$ can be explicitly presented if we project

these two spatial variables in $< x_{norm}, y_{norm} >$ plane, as shown in Figure 2.13(b). Aided by time lag can be determined by the difference of axial strain, the calculation of correlation coefficient will result a data point in the correlation field, characterized by lags $\delta_{xnorm} = -0.475, \delta_{ynorm} = -1.042$ and $\delta_t = 13\,\text{min}$. By iterating this process through each pair of spatial variables, we can obtain the coefficient cloud field as shown in Figure 2.13 (d).

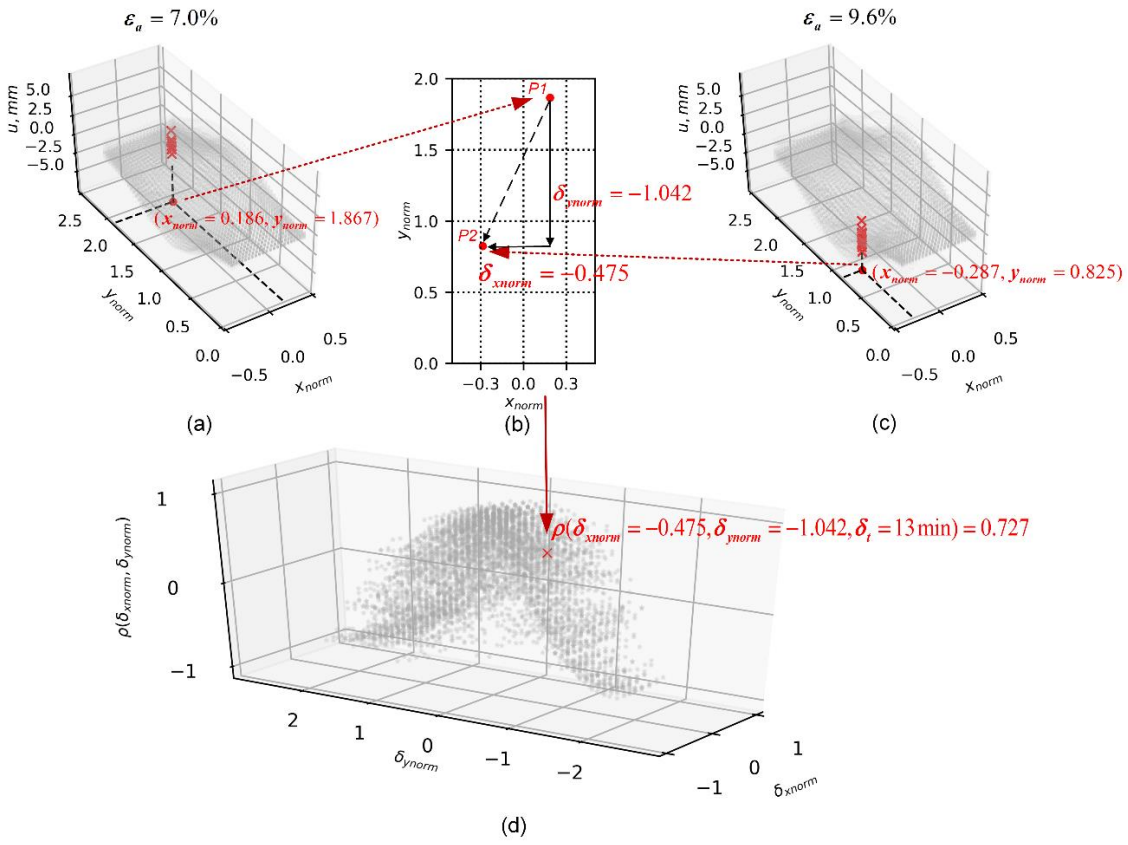

Figure 2.13 Illustration of computing spatio-temporal correlation coefficients for 3D-T data ensembles: (a) spatial coordinates of first variable P1; (b) spatial lags between P1 and P2; (c) spatial coordinates of second variable P2; (d) Resulted correlation coefficient defined by spatio-temporal lags

Once the empirical correlations calculated for all loading phases (0.2 to 9.6%), it is then aimed to construct a smooth correlation structure to estimate the spatio-temporal correlations further than the empirical knowledge. The process is similar to spatio-temporal correlation maps we generated for 1D-T datasets (Figure 2.6 and 2.8), except one more dimension is added to the definition of lags. The 4D volume fitting all empirical correlation coefficients for u, v, and w displacement fields are presented in Figure 2.14, and for U_ρ, U_ϕ and U_y fields are presented in Figure 2.15. Not surprisingly, correlation gradually collapse with the increase of time lag for all displacement fields. The sub-plots in second row of Figure 2.14 and 2.15 are spatial correlations when time lag equals to zero ($\delta_t = 0\,\text{min}$). In first sub-plot of Figure 2.14 (b), two intense correlation bands showing along diagonal and off-diagonal directions implies shear bands have caused material translation dependencies in horizontal directions. Comparing correlation structures of v and w fields, positive values exhibit for nearly the entire domain for the former due to the upward compression process, yet significant out of plane correlation merely exist in a small circle centred at zero spatial lags, suggesting that bulging effect only evident inside of expansion band. In Figure 2.15 (b), we can observe negative correlation distributed along the normalized heights of -1 and 1 in the first sub-plot. This corresponds well with our finding in correlation analysis of 1D-T radius displacement, which shows an opposite radial deforming trend if two local spots on specimen surface spacing around half of specimen height. In second sub-plot of Figure 2.15 (b), the correlations of the tangential displacements seems to be affected by diagonal and off-diagonal shear bands, but the patterns are not distinct. Note

that tangential displacement relates with surface rotation centred along specimen axis. However, in a 3D system, any particle rotation can be analysed with respect to three orthogonal axes. Thus, the further investigation of relationship between soil failure mechanism and localization effects would require the proper characterization of local kinematics in a 3D coordinates system, ideally should be consistent with specimen shape and principle stress directions.

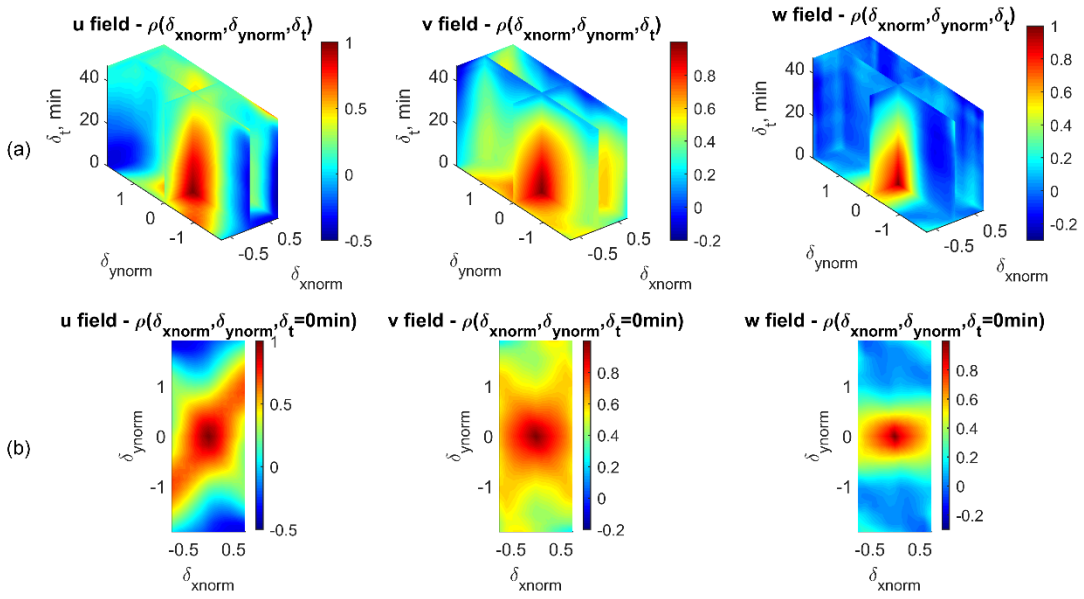

Figure 2.14 Spatio-temporal empirical correlation structures of 3D-T-Ca data ensembles: (a) smooth representation of correlation structures for *u*, *v*, and *w* displacement fields (left to right); (b) spatial correlation maps for *u*, *v*, and *w* displacement fields when $\delta_t = 0\,\text{min}$ (i.e. basis of Figure 2.14 (a))

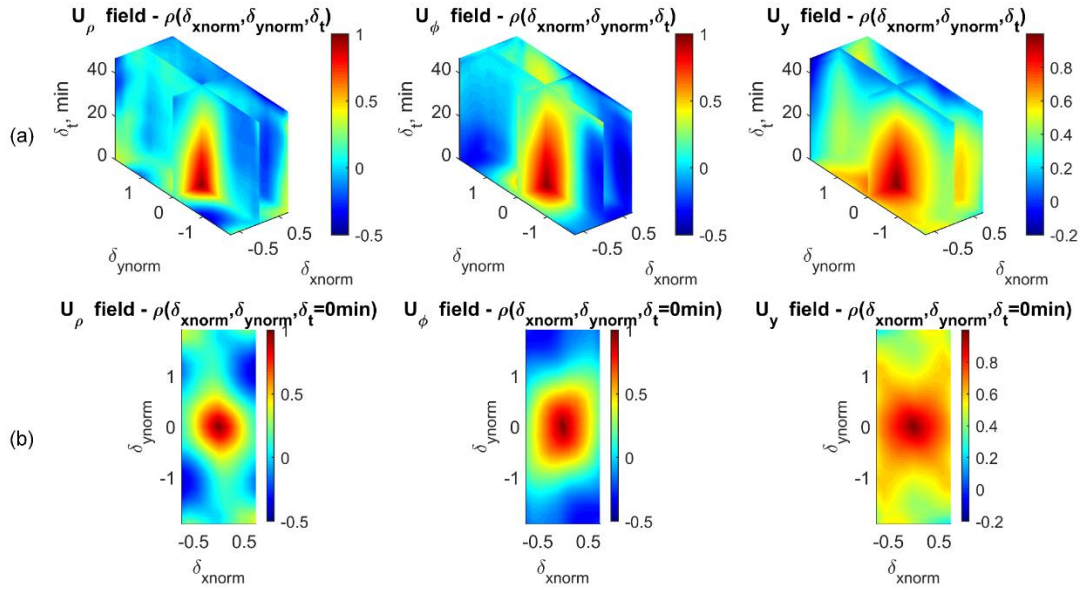

Figure 2.15 Spatio-temporal empirical correlation structures of 3D-T-Cy data ensembles: (a) smooth representation of correlation structures for U_ρ , U_ϕ and U_y displacement fields (left to right); (b) spatial correlation maps for U_ρ , U_ϕ and U_y displacement fields when $\delta_t = 0\,\text{min}$ (i.e. basis of Figure 15 (a))

In light of above results, the impact are not only offer the statistical insights of data ensembles, the obtained first- and second-order statistics are indeed essential elements for simulating these random displacement fields. If the studying random field satisfies the Gaussian stationary criteria, one can simply reproduce these random responses by Gaussian random simulation accounting for uncertainty and spatio-temporal dependencies of the process (Medina-Cetina, 2006). However, if the empirical correlation structure does not present asymptotic Gaussian properties (non-Gaussian), and its first- and second- moments are varying in temporal domain (non-stationary), one must resort to some other non-Gaussian non-stationary simulation methods, such as *Polynomial Chaos Expansion* (PCE) (Ghanem and Spanos, 1991; Medina-Cetina, 2006).

Although the present authors' work has not yet proceeded to the quantification of these properties, the potential benefit of simulating material responses under multi-scale scopes is anticipated to alleviate burdens on experimental efforts to reproduce soil failure process, and likely to be able used as a surrogate in further studies.

2.4. Conclusions

This study introduces a general first- and second-order statistical research framework applied to boundary displacement observations sampled from a series of nominally similar triaxial compression tests. To the authors' knowledge, the statistics of localization patterns revealed in triaxial compression test has not been thoroughly considered previously. Even though the advances in non-destructive sampling technique has enabled us to gain detailed deforming information beyond global stress-strain responses, it is not certain which failure mechanism would occur, or dominate among several competing mechanisms. The results of this study provide insights toward the overall deformation patterns and inherent uncertainties of specimen undergoing three-dimensional stress conditions, as well as spatio-temporal correlation patterns of displacement fields. The conclusion can be drawn as follows:

(a) The first order statistics of boundary 1D-T vertical displacements shows that specimen is deformed with three distinct patterns along vertical direction–the rigid body upward movement at the bottom, the linear decreasing zone in the middle, and non-linear decreasing area at the top. Further, spatio-temporal correlation analysis reveals the trend that a significant upper part displacement at early stage would associate with afterwards large lower part displacement if two phases apart at least 10 minutes (2% of

axial strain). We argued herein it may due to the development of expansion band which had caused local volumetric dilation of specimen at early phase, and it consequently created accommodating ability for significant lower portion movement at later stages.

(b) The similar analysis performed on 1D-T radial displacement demonstrates the bulging uncertainty are primarily influenced by the curvature of expanding profile, instead of relative positions of banding area. Second order statistics of radial displacements presents the negative deformation dependency if two studying areas spacing around half of specimen height, which leads to the non-erratic volume change of specimen in the global sense.

(c) Statistics of 3D-T full field measurements suggests that uncertainty of deformation pattern are greatly affected by the variability of localization behaviour, such as the development of expansion band and shear band, which is started as early as hardening phase. The presence of shear and expansion bands can also introduce deformation dependencies in space and time. However, a key element of elucidating these deformation dependencies and its relationship with soil failure mechanism would further require the illustration of local kinematic properties of testing specimen, including local translation, rotation, dilation or contraction behaviours as well as their uncertainties evolved in space and time.

2.5. References

Abedi, S. (2012) *Meso-scale kinematics in shear bands and impact of material heterogenerity on shear band development in sand*. PhD Dissertation. University of Southern California, Los Angeles, CA.

Alshibli, K. A. *et al.* (2000) 'Assessment of Localized Deformations in Sand Using X-ray Computed Tomography', *ASTM Geotechnical Testing Journal*, 23(3), pp. 274–299.

Alshibli, K. A. *et al.* (2016) 'Influence of Particle Morphology on 3D Kinematic Behavior and Strain Localization of Sheared Sand', *Journal of Geotechnical and Geoenvironmental Engineering*, 143(2), p. 04016097. doi: 10.1061/(ASCE)GT.1943-5606.0001601.

Andò, E. *et al.* (2012) 'Grain-scale experimental investigation of localised deformation in sand: A discrete particle tracking approach', *Acta Geotechnica*, 7(1), pp. 1–13. doi: 10.1007/s11440-011-0151-6.

Desrues, J. *et al.* (1996) 'Void ratio evolution inside shear bands in triaxial sand specimens studied by computed tomography', *Géotechnique*, 46(3), pp. 529–546. doi: 10.1680/geot.1996.46.3.529.

Desrues, J., Lanier, J. and Stutz, P. (1985) 'Localization of the deformation in tests on sand sample', *Engineering Fracture Mechanics*, 21(4), pp. 909–921. doi: 10.1016/0013-7944(85)90097-9.

Desrues, J. and Viggiani, G. (2004) 'Strain localization in sand: An overview of the experimental results obtained in Grenoble using stereophotogrammetry', *International Journal for Numerical and Analytical Methods in Geomechanics*, 28(4), pp. 279–321. doi: 10.1002/nag.338.

Ghanem, R. G. and Spanos, P. D. (1991) *Stochastic Finite Elements: A Spectral Approach*. New York: Springer-Verlag. doi: 10.1007/978-1-4612-3094-6.

Macari, E., Parker, J. and Costes, N. (1997) 'Measurement of Volume Changes in Triaxial Tests Using Digital Imaging Techniques', *Geotechnical Testing Journal*, 20(1), pp. 103–109. doi: 10.1520/GTJ11424J.

Matsushima, T. *et al.* (2006) 'Micro X-Ray CT at spring-8 for granular mechanics', in *Soil Stress-Strain Behavior: Measurement, Modeling and Analysis*. New York: Springer, pp. 225–234. doi: 10.1007/978-1-4020-6146-2.

Medina-Cetina, Z. (2006) *Probabilistic calibration of a soil model*. PhD Dissertation. The John Hopkins University, Baltimore, MD.

Oda, M. and Iwashita, K. (2000) 'Study on couple stress and shear band development in granular media based on numerical simulation analyses', *International Journal of Engineering Science*, 38(15), pp. 1713–1740. doi: 10.1016/S0020-7225(99)00132-9.

Oda, M. and Kazama, H. (1998) 'Microstructure of shear bands and its relation to the mechanisms of dilatancy and failure of dense granular soils', *Géotechnique*, 48(4), pp. 465–481. doi: 10.1680/geot.1998.48.4.465.

Oda, M., Takemura, T. and Takahashi, M. (2004) 'Microstructure in shear band observed by microfocus X-ray computed tomography', *Géotechnique*, 54(8), pp. 539–542. doi: 10.1680/geot.2004.54.8.539.

Omidvar, M., Chen, Z. (Chris) and Iskander, M. (2015) 'Image-Based Lagrangian Analysis of Granular Kinematics', *Journal of Computing in Civil Engineering*, 29(6), p. 04014101. doi: 10.1061/(ASCE)CP.1943-5487.0000433.

Rechenmacher, A., Abedi S. and Chupin, O. (2010) 'Evolution of force chains in shear

bands in sands', *Géotechnique*, 60(5), pp. 343–351. doi: 10.1680/geot.2010.60.5.343.

Rechenmacher, A. L. (2006) 'Grain-scale processes governing shear band initiation and evolution in sands', *Journal of the Mechanics and Physics of Solids*, 54(1), pp. 22–45. doi: 10.1016/j.jmps.2005.08.009.

Rechenmacher, A. L. *et al.* (2011) 'Characterization of mesoscale instabilities in localized granular shear using digital image correlation', *Acta Geotechnica*, 6(4), pp. 205–217. doi: 10.1007/s11440-011-0147-2.

Rechenmacher, A. L. and Finno, R. J. (2003) 'Digital Image Correlation to Evaluate ShearBanding in Dilative Sands', *Geotechnical Testing Journal*, 27(1), pp. 1–10. doi: https://doi.org/10.1520/GTJ11263J.

Roscoe, K. H. (1970) 'The Influence of Strains in Soil Mechanics', *Géotechnique*, 20(2), pp. 129–170. doi: 10.1680/geot.1970.20.2.129.

Sutton, M. A., Orteu, J. J. and Schreier, H. (2009) *Image Correlation for Shape, Motion and Deformation Measurements - Basic Concepts, Theory and Applications*. New York: Springer.

3. ASSESSMENT OF 3D BOUNDARY KINEMATIC PHENOMENA IN SAND SPECIMENS UNDER VARYING EXPERIMENTAL CONDITIONS

3.1. Introduction

Strain localization in sand is a ubiquitous process associated with non-homogeneous deformation occurred to material when subjected to compressive or tensile stress. In a typical soil failure process, the accumulating of strain localization commonly manifested as the onset and evolution of intense straining fields, such as shear or compaction band, which encompass the main material responses from softening to critical state in a deforming body (Borja, 2000; Rechenmacher and Finno, 2003). The analysis of such localization phenomena requires the access to full displacement field, and the selection of representative features of grains that is sufficient to contrast unique mechanical behaviour within the localization zone from the outside areas. The proliferation of simulation and sensing technology in the last few decades has enabled researchers to sample the whole boundary or volume of a deforming body, to a fine scope (meso- or micro-scale) that allows one to measure particle-scale mechanical properties. In modelling of micromechanics of granular material, DEM (Cundall and Strack, 1979; Bardet and Proubet, 1991) has played a vital role since the method based on particle-particle interactions and particle morphology so the strain localization can be revealed in micro-scale (Bardet and Proubet, 1991; Ng, 1994; Oda and Iwashita, 2000; Alonso-Marroquin *et al.*, 2006; Mohamed and Gutierrez, 2010; Jiang *et al.*, 2011). In addition, multiscale frameworks have been proposed by some authors (Andrade *et al.*,

2011; Nitka *et al.*, 2011), to bridge different material scales and allow discrete physics can be conveyed into continuum modelling. However, in spite of enormously improvement on computational power, such methods still suffer from high computational cost and difficulty in accounting for particle geometry. Additionally, the implementation of accurate models needs to be established on the foundation of exact knowledge of the physical process of interest, which largely depends on laboratory tests, otherwise the credibility of numerical simulations would be diminished and merely regarded as "virtual evidence".

In experimental investigation of full displacement field, different techniques have been utilized to track the evolution of strain localization, including X-ray tomography (Desrues *et al.*, 1996; Alshibli *et al.*, 2000), synchrotron X-ray micro tomography (Viggiani *et al.*, 2004; Matsushima *et al.*, 2006; S.A. Hall *et al.*, 2010), 2D or 3D digital image correlation (DIC) (Rechenmacher and Finno, 2003; Medina-Cetina, 2006), among others. The advantage of using X-ray related methods lies in its ability to reveal particulate movement that essentially as underlying mechanism governing macro-scale deformation, which can occur internally or along the boundary of specimen. However, the practical constraints have resulted relevant analyses conducted only over large increments, small specimens or large particle size. Theoretically, strain bifurcation prior to or at the peak state is anticipated to initiate over very small time step, thus sampling frequency is crucial to disclose the true process of band initiation. Behavior accumulated over wide increments, on the contrary, would tend to smear any instantaneous strain

fluctuations, or strain localization features, over the whole increment (Desrues and Viggiani, 2004).

The DIC technique coupled with experimental exploration has proved as a promise method to elucidate grain-scale displacement field with a nominally spatial-temporal continual configuration. The result of DIC analysis usually reflects meso-scale displacement field (smaller than global-scale and bigger than particle-scale), which derived from pixel analysis between two digital images to indicate deformation features of soils within subgroups. The relatively convenient implementation and nearly temporal continuous description of the motion makes it increasingly popular to be adpoted in the study of geomaterial mechanism (White, Take and Bolton, 2003; Liu and Iskander, 2004; Stephen A Hall *et al.*, 2010). For example, Rechenmacher (2006) used DIC to quantify the triggering of the formation of persistent shear bands and initially investigated kinematic properties within shear bands of sand specimen undergoing plane strain deformation. Following this, Rechenmacher and her co-workers (2010, 2011, and 2012) further evaluated shear, rotational and volumetric strains, build-up and collapse of force chains, as well as vortex structures in a spatial-temporal manner. Note that all these work were carried out under two-dimensional stress conditions, which disregards out of plane translational or rotational behaviours.

Even though 3D-DIC (stereovision system) has seen remarkable growth and used in the characterization of material response in recent years (Medina-Cetina, 2006; Sutton *et al.*, 2008), to the author's knowledge, no relevant research has been found to address local kinematics (translation, rotation, expansion/contraction, etc.) under three-

dimensional stress conditions. This is attributed to the basic characteristic of DIC as an approach that perform non-intrusive sampling, thus internal deformation gradient, which is necessary for quantifying 3D object motions, is hard to determine. In addition, in order to effectively reveal the desired kinematic properties of materials, the appropriate selection of a coordinate system is also a challenge. For example, under micro-scale that is able to accounts for particulate motions, Alshibli and Alramahi (2006) employed Spherical coordinates to compute rotational angles of soil particles. While in aforementioned two-dimensional stress conditions, Rechenmacher (2006) used conventional 2D rectangular Cartesian coordinates for calculating corresponding kinematics. These analysis frameworks, unfortunately, are not suitable for the present research due to the observed data in this research are displacements occurred to 'cluster of soil particles' (i.e. in meso-scale) manifested on curved specimen boundary (non-rectangular layout). It is clear a systematic approach to account for 3D meso-scale kinematics of displacement field is still lacking.

Here, we provide the complete set of first order 3D kinematic operators under Cylindrical coordinates that are consistent with specimen geometry and suitable to characterize meso-scale kinematics comprising translational, rotational and volumetric behaviours throughout triaxial compression process. The paper is outlined in four parts. First, we give a brief introduction of laboratory triaxial compression tests, and the 3D DIC techniques used in this research. Then, 3D kinematic operators under Cylindrical coordinates are explained, as well as the method to incorporate those into current research framework. Next, we provide the experimental design of kinematic

characterization, and the corresponding results composed of kinematic phenomena calculated under different experimental conditions. Finally, the paper is concluded on synthesis of obtained results, and the insights provided to help advance the current understanding of different deteriorating mechanisms that contribute to the failure process of sand.

3.2. Experimental method

3.2.1. Triaxial test

Specimens of dry sand, classified as SP, were tested under three dimensional stress conditions. The coefficients of uniformity and curvature are 2.34 and 1.11 respectively. Total five tests are selected in present kinematic analysis, the main sample features are summarized in Table 3.1. All specimens are approximately 160mm in height, and 70mm in diameter. Three specimens with relative density more than 90.00%, while one loose specimen and one layered specimen presented with much lower density than the rest. The layered specimen herein were designed as bottom half "dense" and the top half "loose", with the purpose of investigating the effect of varying specimen density on kinematics during the compression. Dry pluviation was used to prepare this layered specimen, and the loose part was constituted by carefully dropping sand at zero height of specimen top.

Table 3.1 Summary of main features of testing specimens

Test name	Height (mm)	Diameter (mm)	Relative density (%)	Friction angle (deg)	Peak (σ_1'/σ_3')	Notes
092903b	155.50	71.33	91.09	49.51	7.35	40kPa confinement
121304d	159.50	71.38	99.71	50.95	7.95	20kPa confinement
121304c	160.00	70.48	93.72	48.59	7.00	60kPa confinement
121304b	158.17	70.86	46.39	40.88	4.79	Loose specimen (40kPa)
120704c	157.67	70.88	68.90	43.71	5.43	Layered specimen (40kPa)
	79.50	71.27	98.87	-	-	Lower: dense sand
	78.17	70.68	30.54	-	-	Upper: loose sand

The testing apparatus is similar to that normally used in conventional triaxial compression test, except Plexiglass cell was removed and specimens were vacuum consolidated, for the purpose of avoiding light refraction or reflection that may disturb the proper image acquisition. Most tests were consolidated to 40kPa isotropic confining pressure, but two tests were consolidated at confining pressures of 20kPa (121304d) and 60kPa (121304c) respectively. Axial compression was carried out at a constant axial strain rate of 0.2%/min until specimen was fully sheared. Global stress-strain and axial strain-volumetric strain responses were given in Figure 31. In Figure 3.1 (a), peak stress is evident for dense specimen (tests 092903b, 121304d and 121304c), but not for loose or layered specimen. Figure 3.1 (b) shows volumetric strain behaviors of all tests. Because confining cell was removed which makes it difficult to conduct direct

measurements of volume change, an indirect approach was adopted where volumetric strain was derived by calculating averaged radial and vertical displacement along the vertical direction of specimen, and then the global volumetric strain can be estimated as the accumulation of strains along each height of specimen. The technique details and validations can be found in Macari, Parker and Costes (1997) and Medina-Cetina (2006). In Figure 3.1 (b), the clear dilation is seen among dense specimens, and layered specimen again present with approximate loose specimen's behavior.

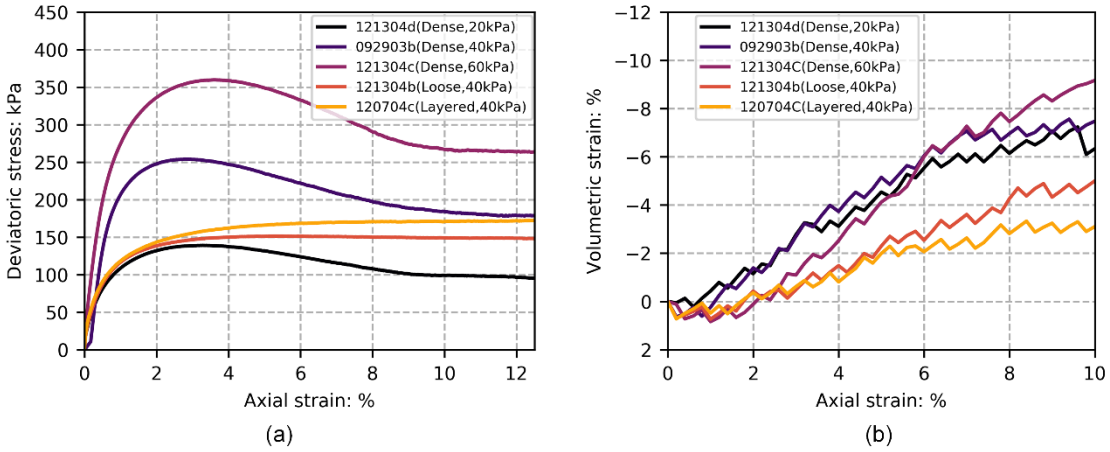

Figure 3.1 Global material responses: (a) triaxial stress-strain curves (b) axial strain-volumetric strain curves

3.2.2. 3D DIC

The DIC method is a non-contact, optical method for measuring displacement field on a deforming body. The object tracked by DIC analysis is a cluster of coloured pixels, called subset. When studying material evolved from initial state to deformed state, DIC measures the translational and rotational behaviours of overlapping subsets

between the reference image and target image. These captured pixel subsets are essentially composed of colours of sand reflected on the latex membrane. Due to the innate heterogeneity of sand colours, the distinct greyscale patterns of each subset can be directly recognized through matching algorithm without any artificial intervention. In present work, two digital cameras were obliquely setup in front of specimen to construct a 3D scene, which is similar to how human eyes acquire an object's shape and position. The calibration of lenses involves capture synchronous images of a standard grid oriented at different angles. From obtained images, key camera parameters (e.g. position and orientations, focal length, lenses distortions, etc.) were calibrated. After confirming the object's 3D spatial information, 3D displacements can be computed as comparing overlapping pixel subsets between reference and target images as described above.

The software VIC-3D, by Correlated Solutions, Inc., were utilized to extract 3D displacement fields from the stereo images. The error measure for best match of subsets was implemented through normalized cross-correlation criterion (Sutton *et al.*, 2000). To enable the continuous displacement distribution and thus accommodating evaluations of subsets contraction/expansion, rotation, and other kinematic characteristics on a continuum scale, displacement vectors were interpolated to cubic order which resulted a resolution of spaced center-to-center around 0.4mm. The stereo images were taken every 15 seconds corresponding to 0.05% of axial strain through the course of compression, but an increment of 0.2% of axial strain was deemed sufficient to represent the evolution of localization effects (Rechenmacher *et al.*, 2011; Song, 2012), thereby incremental displacement were updated every 4 images, i.e. 0.2% of axial strain. The measurement

accuracy was assessed by comparing averaged vertical displacement through DIC data with global readings by LVDT transducers, and the difference was found approximately $\pm 0.02mm$.

Figure 3.2 presents displacement fields of test 092903b between axial strain 3.2% and 7.0% in Eulerian description (superimposed on deformed body) resulted from 3D DIC analysis. The first row is displacement vectors decomposed into horizontal, vertical, and out-of-plane directions. The horizontal displacement as anticipated related to the development of expansion band, which concentrate in the middle of specimen and drive the soil moving towards opposite directions if viewed in horizontal plane. The vertical displacement field (second sub-plot) suggests the specimen was compressed approximately as three separate "moving blocks" that possess different deforming rate. This can associate with variation of specimen stiffness along the vertical direction (Medina-Cetina and Rechenmacher, 2010). The bulging effect of specimen was depicted well in the plot of out-of-plane displacement field (third sub-plot), and maximum value was seen appeared to the centre of specimen. The second row in Figure 3.2 is the same displacement vector but decomposed under the Cylindrical coordinates, yielded radial, tangential and axial displacement fields. Amidst three, tangential displacement shows interesting intensified region along the diagonal direction, suggesting local areas tend to rotate clockwise along the specimen circumference. This agrees well with previous findings that intense rolling of particles within the shear band (Oda and Iwashita, 2000; Rechenmacher, 2006).

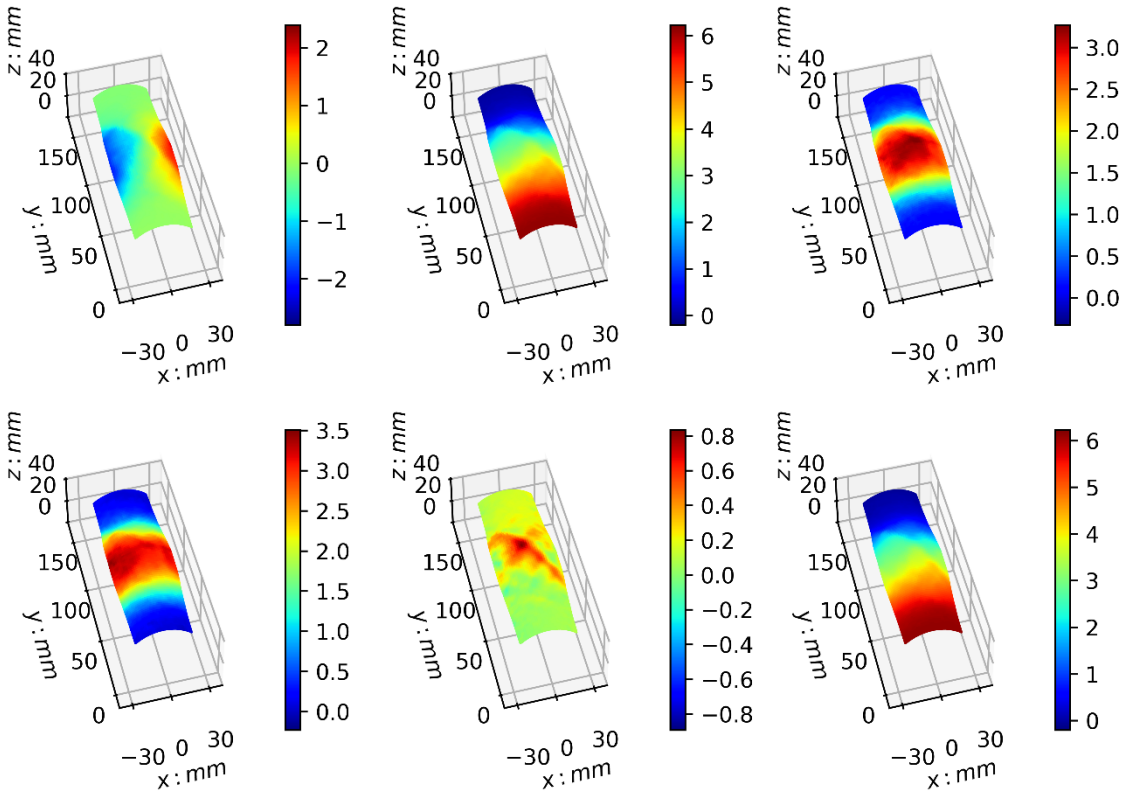

Figure 3.2 (a) Incremental displacement fields of test 092903b between axial strain 3.2% and 7.0%, left to right are displacements along horizontal, vertical and out-of-plane directions; (b) Same displacement field decompose into radial, tangential, and axial directions in Cylindrical coordinates

3.3. 3D kinematic operators under Cylindrical coordinates

One of the special interest of present research is to link the localization effects with kinematic behavior of specimen, such as compression, rotation, and/or translation, which can be derived from the raw displacement measurements. Herein, we choose Cylindrical coordinate consistent with specimen geometry and suitable for presenting three-dimensional stress condition. The observed displacement fields across the specimen boundary are decomposed in radial, tangential, and axial directions, as described in preceding section. Figure 3.3 shows the steps to construct the 3D objects for

kinematic investigation. In sub-plot Figure 3(a), a surface area $abcd$ schematically represents sampled boundary coordinates by 3D DIC method. However, this does not allow us to directly compute kinematic quantities since no consecutive measurements along $\hat{\rho}$ axis, which makes the calculation of gradient component along $\hat{\rho}$ direction impossible. In order to overcome this issue, we introduced a series of auxiliary origins distributed along center axial of specimen, as depicted in Figure 3.3 (b). The radial and tangential displacements are assumed zero for these origins, while the axial displacements are estimated by averaging sampled vertical displacements along the boundary at the corresponding specimen height. This assumption is inspired by experimental evidence provided in Desrues *et al.* (1996) and Alshibli *et al.* (2000), where the failure mode in triaxial specimen was found comprised of a rigid cone located along the center axial line, and multiple shear planes linked the boundary of cone and extended to the specimen surface, implying the radial and tangential displacement occurred to the axial line should be trivial. The final step, as shown in Figure 3.3 (c), is to connect the introduced origins with the material coordinates at the specimen surface, a series of 3D studying objects are consequently established as the demonstrative one shaded in blue color.

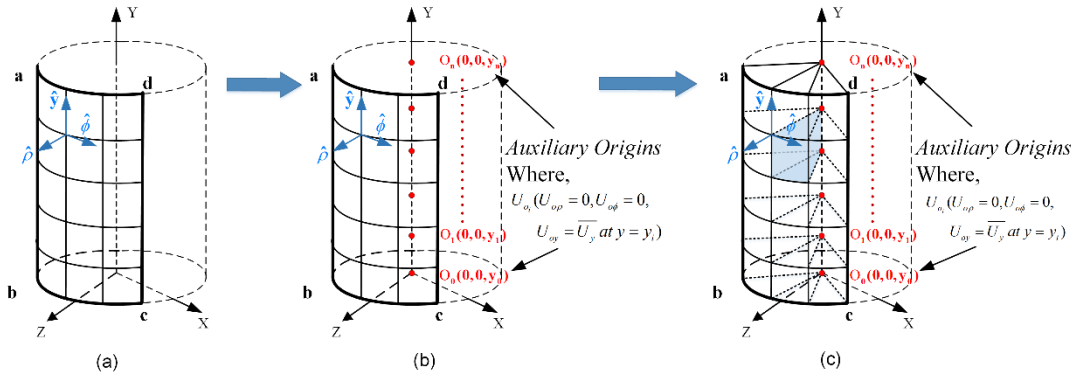

Figure 3.3 Schematic illustration of 3D studying objects that produced by connecting boundary coordinates with introduced auxiliary origins

After establishing the studying objects, next, is to identify the kinematic operators under current configuration. The conventional first-order kinematics includes *gradient*, *divergence*, and *curl* operators acting on the vector field U. The definition of these quantities is through an operator called *del*, or *nabla*, and its tensor, dot, and cross product with the vector field U. Equation 3.1 to 3.3 provide the expressions of *gradient*, *divergence*, and *curl* under Cylindrical coordinates. Gradient of a 3D vector field U would generate a deformation tensor F, comprised of nine components representing translational or rotational changing rate of local area affected by the vector field U. Sum of diagonal terms presented in F is the divergence indicating the magnitude of sink or source of local area. Moreover, the difference between every two off-diagonal terms in F gives each component of curl representing local rotational tendency with respect to every axis. Full derivation of first-order kinematic operators under Cylindrical coordinates can be found in Appendix A. By making use of these operators, we can

obtain a direct description of local straining or rotating kinematic behavior occurred to specimen during the course of shearing.

$$gradU = [F] = [\nabla \otimes U] = \begin{bmatrix} \frac{\partial U_\rho}{\partial \rho} & \frac{1}{\rho}\left(\frac{\partial U_\rho}{\partial \phi} - U_\phi\right) & \frac{\partial U_\rho}{\partial z} \\ \frac{\partial U_\phi}{\partial \rho} & \frac{1}{\rho}\left(\frac{\partial U_\phi}{\partial \phi} + U_\rho\right) & \frac{\partial U_\phi}{\partial z} \\ \frac{\partial U_z}{\partial \rho} & \frac{1}{\rho}\frac{\partial U_z}{\partial \phi} & \frac{\partial U_z}{\partial z} \end{bmatrix} \tag{3.1}$$

$$divU = \nabla \bullet U = \frac{1}{\rho}\frac{\partial}{\partial \rho}(U_\rho \bullet \rho) + \frac{1}{\rho}\frac{\partial U_\phi}{\partial \phi} + \frac{\partial U_z}{\partial z} \tag{3.2}$$

$$curlU = \nabla \times U = \left(\frac{1}{\rho}\frac{\partial U_z}{\partial \phi} - \frac{\partial U_\phi}{\partial z}\right)\hat{\rho} + \left(\frac{\partial U_\rho}{\partial z} - \frac{\partial U_z}{\partial \rho}\right)\hat{\phi} + \left(\frac{1}{\rho}\frac{\partial}{\partial \rho}\left(U_\phi \cdot \rho\right) - \frac{1}{\rho}\frac{\partial U_\rho}{\partial \phi}\right)\hat{z} \tag{3.3}$$

Figure 3.4 provides an example of nine components of gradient field based on one test's result (092903b), from undeform stage to critical state (axial strain 0.0% to 9.6%). The coordinates has been normalized according to specimen's diameter. The first two sub-plots along diagonal direction F_{11} and F_{22}, indicate local expansions in radial and tangential directions within the shear band. However, in axial direction, compression is observed inside of shearing zone, especially located at the top-left portion as shown in F_{33}. The overall volumetric behavior in terms of these two competing phenomenon can be found in the plot of divergence field as shown in Figure 3.5. A general volumetric dilation is seen in the middle of specimen, further a local concentrating zone can be found coincide with area of shear band. On the other hand, inside of compaction band,

which expressed as negative divergence regions in Figure 5, intense volumetric contraction is found matching with areas of large axial compression as presented in F_{33}. It demonstrates the shear band can introduce highly volumetric expansion or compaction, depends on its overlapping with expansion band or compaction band. This observation can complement the previous studies about volumetric change influenced by shear band, which focused on the large voids (volumetric dilation) generated by intense rolling of soil particles under the plane strain conditions. (Oda and Kazama, 1998; Rechenmacher, 2006).

Figure 3.6 presents the curl fields with respect to three axes. Sub-plots (d), (e), and (f) illustrate the positive rotation directions for each case. In Figure 3.6 (a), a shear band is explicitly depicted by highlighted clockwise rotation areas observed along the diagonal direction. It corroborates, again, intense rolling of soil particles occurred inside of shear band (Oda and Kazama, 1998; Rechenmacher, 2006). For rotation with respect to $\hat{\phi}$ axis (as shown in Figure 3.6 (b)), two bands are seen rotating in opposite directions and separated by a neutral zone in the middle, suggesting the "barrel" shape of expansion band. As for curl along $\hat{y}$ axis, an approximate zero rotation is seen across the whole domain, except some deviations are found along the shear band. It is indicative of a general axisymmetric deformation of specimen at current loading stage, yet shear band can cause some global imperfections due to strain localizations.

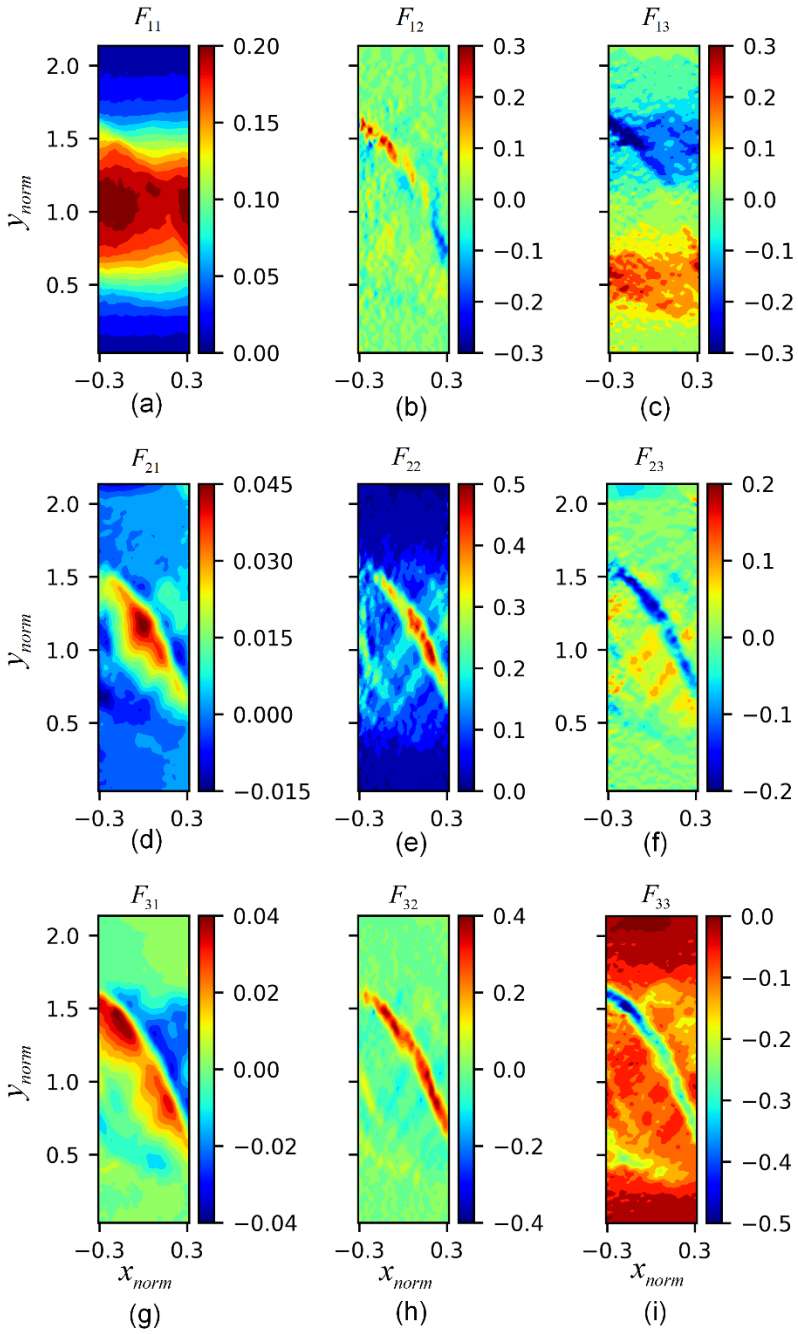

Figure 3.4 Nine components of gradient deformation tensor F based on test 092903b from undeformed stage to loading level of $\varepsilon_a = 9.6\%$

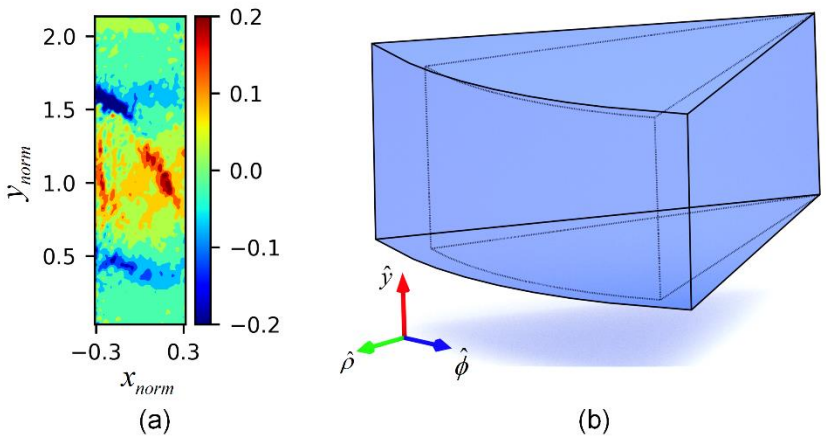

Figure 3.5 Divergence field based on test 092903b at loading level of $\varepsilon_a = 9.6\%$

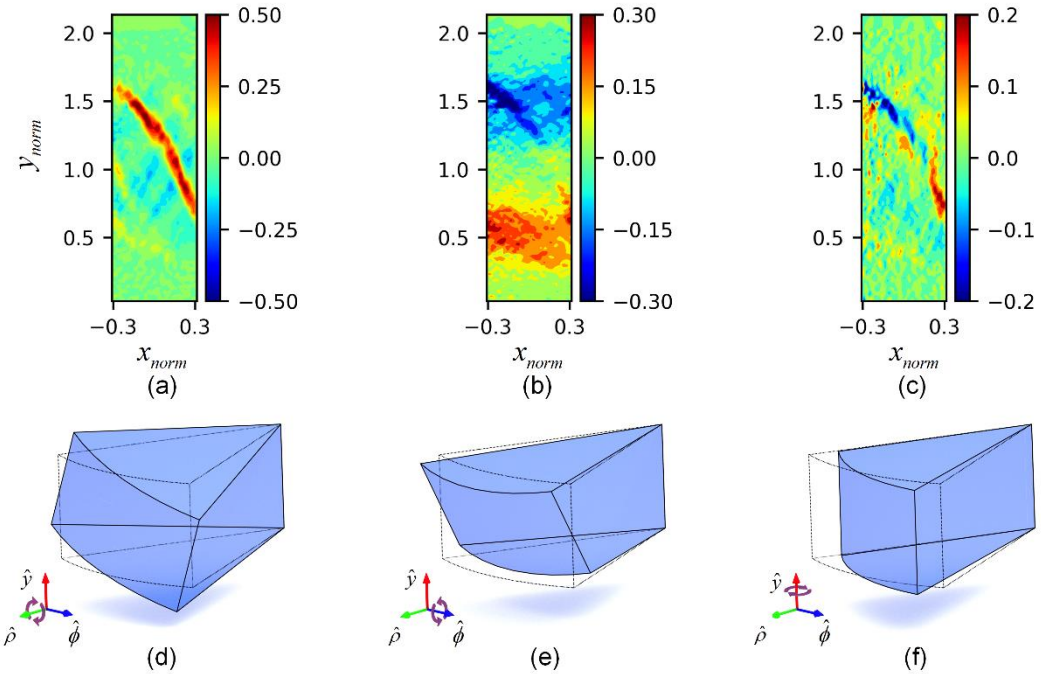

Figure 3.6 Curl components calculated based on test 092903b at loading level of $\varepsilon_a = 9.6\%$: (a) curl field with respect to $\hat{\rho}$ axis; (b) curl field with respect to $\hat{\phi}$ axis; (c) curl field with respect to $\hat{y}$ axis; (d) illustration of positive rotation for curl along $\hat{\rho}$ axis; (e) illustration of positive rotation for curl along $\hat{\phi}$ axis; (f) illustration of positive rotation for curl along $\hat{y}$ axis

3.4. Spatio-temporal evolution of 3D kinematics

3.4.1. Experimental design

In this section, we investigate the onset and evolution of localization effects on varying experimental conditions. Figure 3.7 shows the accumulated strain windows of every analysing increment, specifically, axial strains between 0.0 and 1.0%, 1.0 and 3.0%, 3.0 and 5.0%, 5.0 and 7.0%, 7.0 and 9.0%, respectively. The first two windows, 0.0-1.0% and 1.0-3.0%, are corresponding to elastic and hardening phases for most of tests. After peak stress reached approximately 3.0% of axial strain, dense specimens entered softening stage persisted to the last frame of interest, whereas no clear softening was seen on the loose and layered specimen. Figure 3.8 illustrates experimental design of proposed kinematic analysis. Four identical kinematic quantities, gradient along $\hat{\rho}$ axis (Grad_ρ), gradient along $\hat{y}$ axis (Grad_y), divergence (Div), and curl along $\hat{\rho}$ axis (Curl_ρ), are desired across all tests. The criteria of choosing these properties lie in their denoting processes, such as volumetric behaviour, or rotational tendency along specimen surface, are proved tightly associated with localization effects in sand specimen (Oda and Iwashita, 2000; Rechenmacher, Abedi S. and Chupin, 2010). For each test, and each increment, the kinematic quantities will be tracked over a certain number of consecutive images and referenced to the initial image of that particular increment. Thus, the result will be plotted based on Lagrangian description.

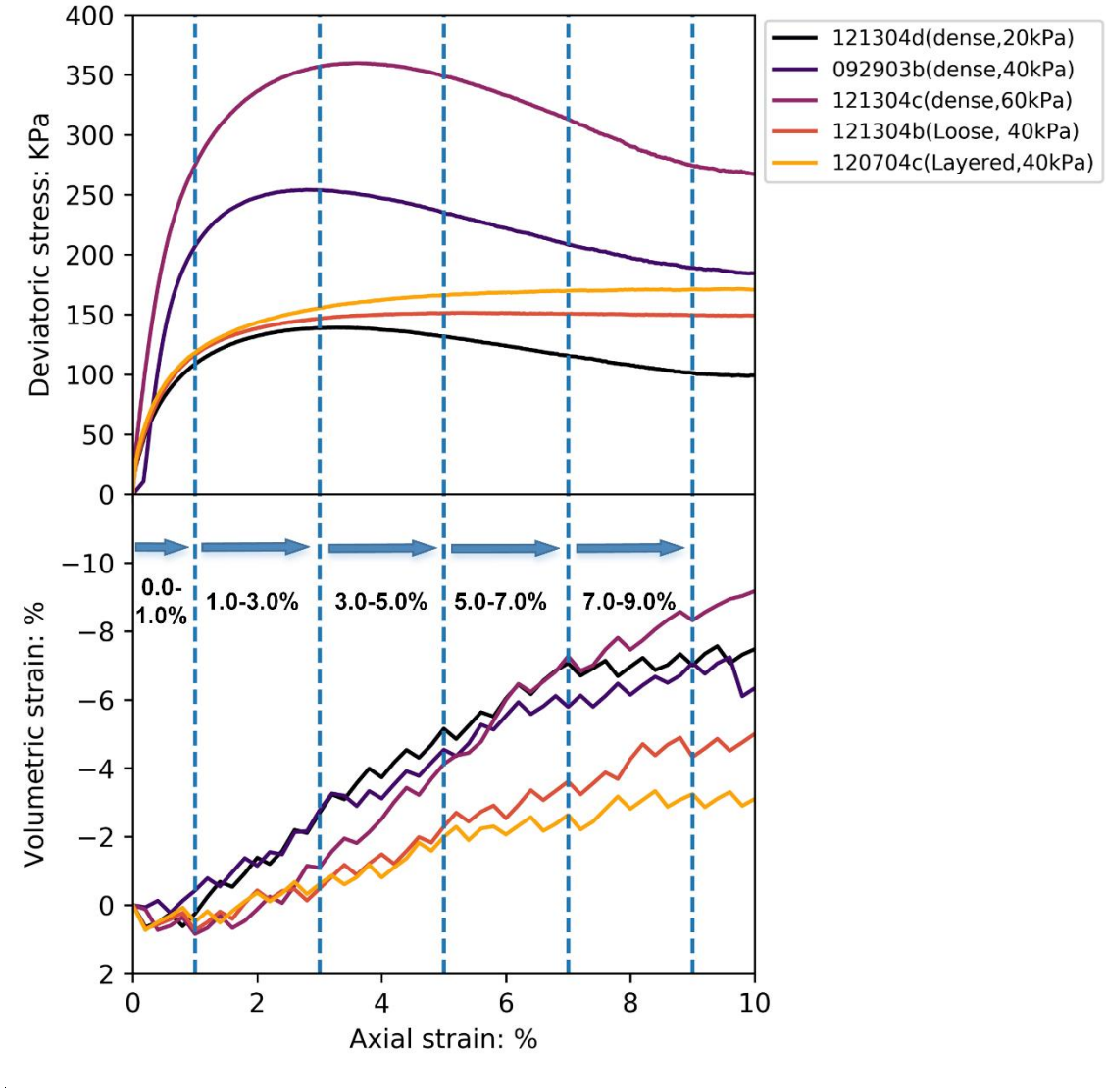

Figure 3.7 Accumulated strain windows for kinematic analyses: 0.0~1.0%, 1.0~3.0%, 3.0~5.0%, 5.0~7.0%, 7.0~9.0%

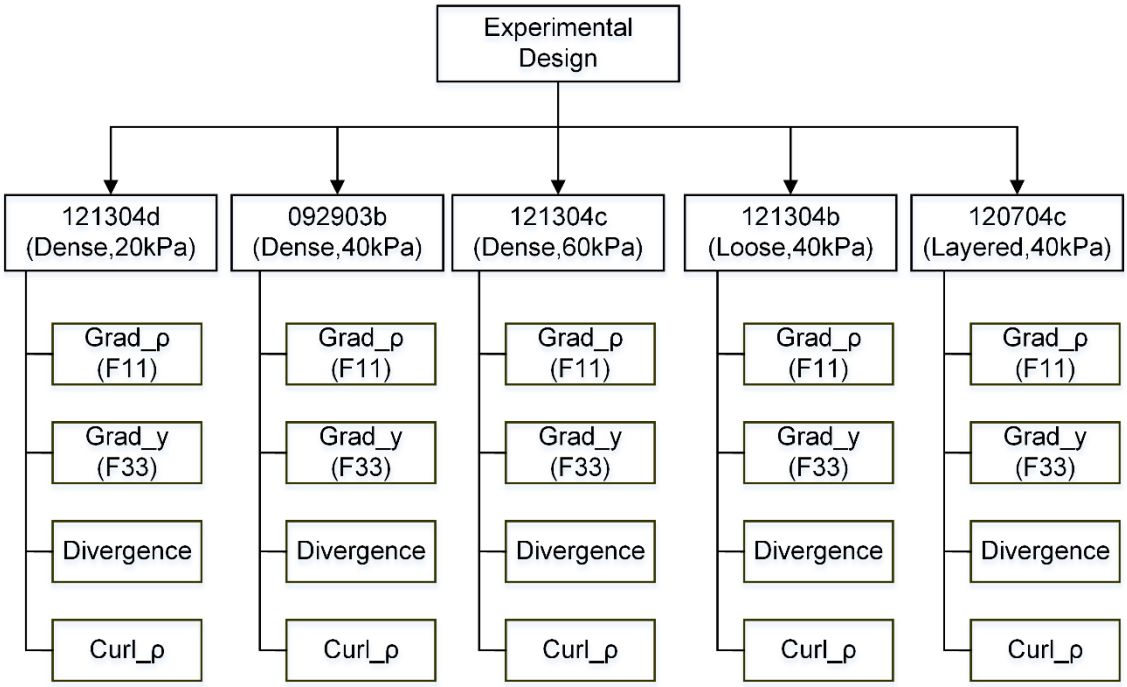

Figure 3.8 Four kinematic properties: Grad_ρ (F11), Grad_y (F33), Divergence, and Curl_ρ, are designed to be calculated for all tests

3.4.2. Spatio-temporal evolution of gradient component along $\hat{\rho}$ axis

Figure 3.9 presents the spatio-temporal evolution of Grad_ρ fields across all tests, which is indicative of the development of expansion bands. It generally started from the hardening phase, distributed uniformly along the middle of specimen until the occurrence of dominant shear band that breaks the symmetry of intensity contour. For dense specimens, it is interesting to find the magnitude of expansion diminished in the last frame (7.0-9.0%), suggesting that radial dilation rate is decreasing when loading approach to the critical state. The main localization effect at this moment is shearing along one or multiple band directions that is essentially mobilize the energy formerly accumulated in the middle expansion band. In loose and layered specimens, the radial deformation is much less evident compared to former ones, indicating budging effect is

not significant in these low density specimens. The expansion in layered specimen is seen taking place at the upper part of specimen, which is comprised of loose material composition, suggesting the governing radial dilation/compaction behaviour is controlled by the weak portion of the specimen. Additionally, it is noted that the layered specimen has the magnitude of radial deformation similar to that of loose specimen, which is also reflected in accumulated global volumetric behaviours as depicted in Figure 3.1.

3.4.3. Spatio-temporal evolution of gradient component along $\hat{y}$ axis

Figure 3.10 shows the spatio-temporal evolution of gradient component along $\hat{y}$ across all tests. The shear bands are highlighted by this kinematic field in the tests 121304d and 092903b, indicating the collapse of 'soil particle columns' (force chains), which caused the local compression parallel to principle stress direction (Oda and Iwashita, 2000), is evident within the banding area. It is also noted that the shape of shear band is not exactly straight, and almost horizontally oriented at its lower end. This agrees well with previous observations through X-ray method (Oda and Kazama, 1998), that the boundary shape of shear band was found gently curved with varying inclination angles with respect to axial direction. In addition, comparing banding phenomena under varying experimental conditions, it is found multiple shear bands emerged when confinement is high (test 121304c), whereas no clear shear band presented when specimen's density is low (loose and layered compositions), consistent with that of Alshibli *et al.* (2000) who showed that active localization effects are usually associated with dense material composition, and high confinement.

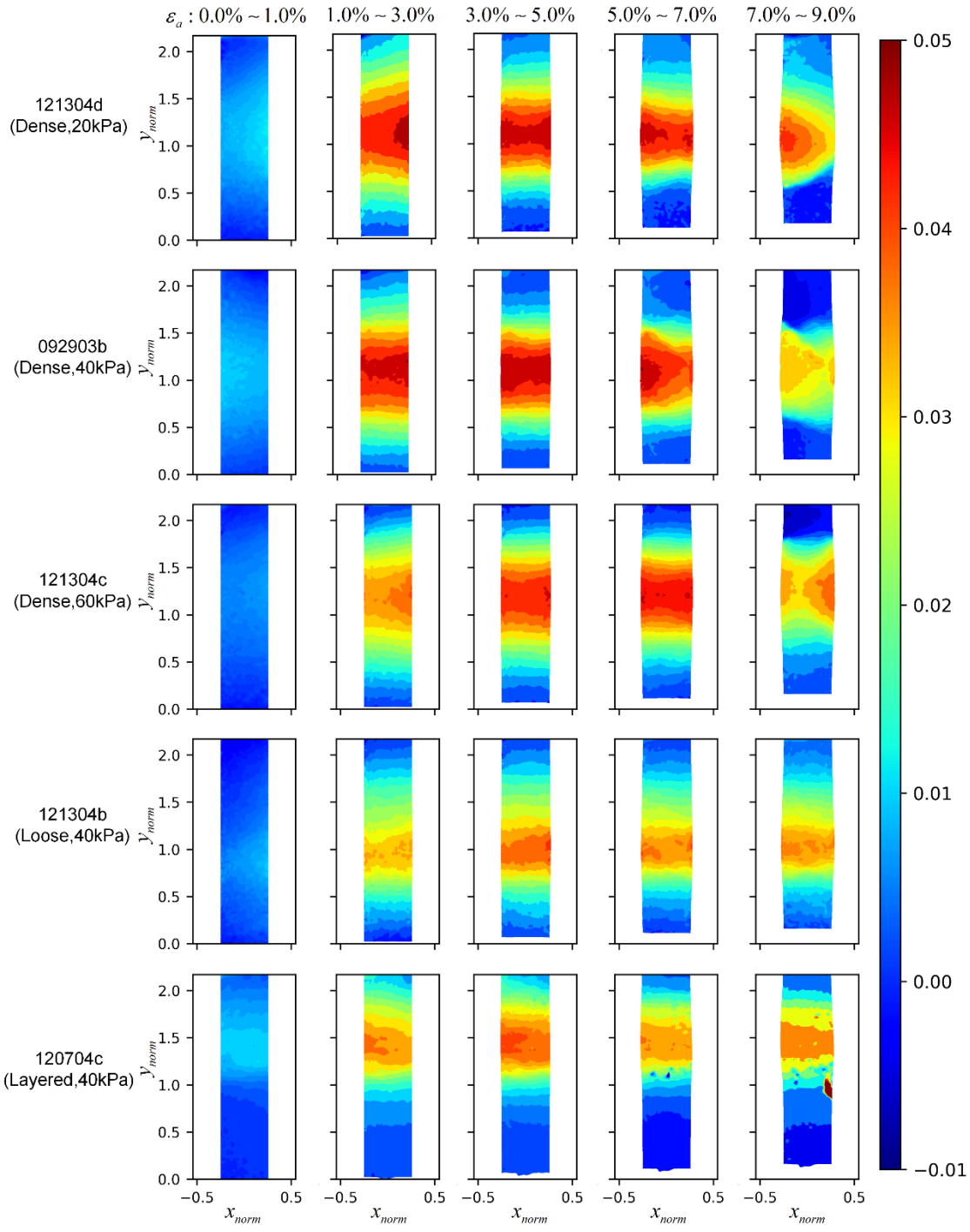

Figure 3.9 Evolution of gradient component along $\hat{\rho}$ axis of all tests

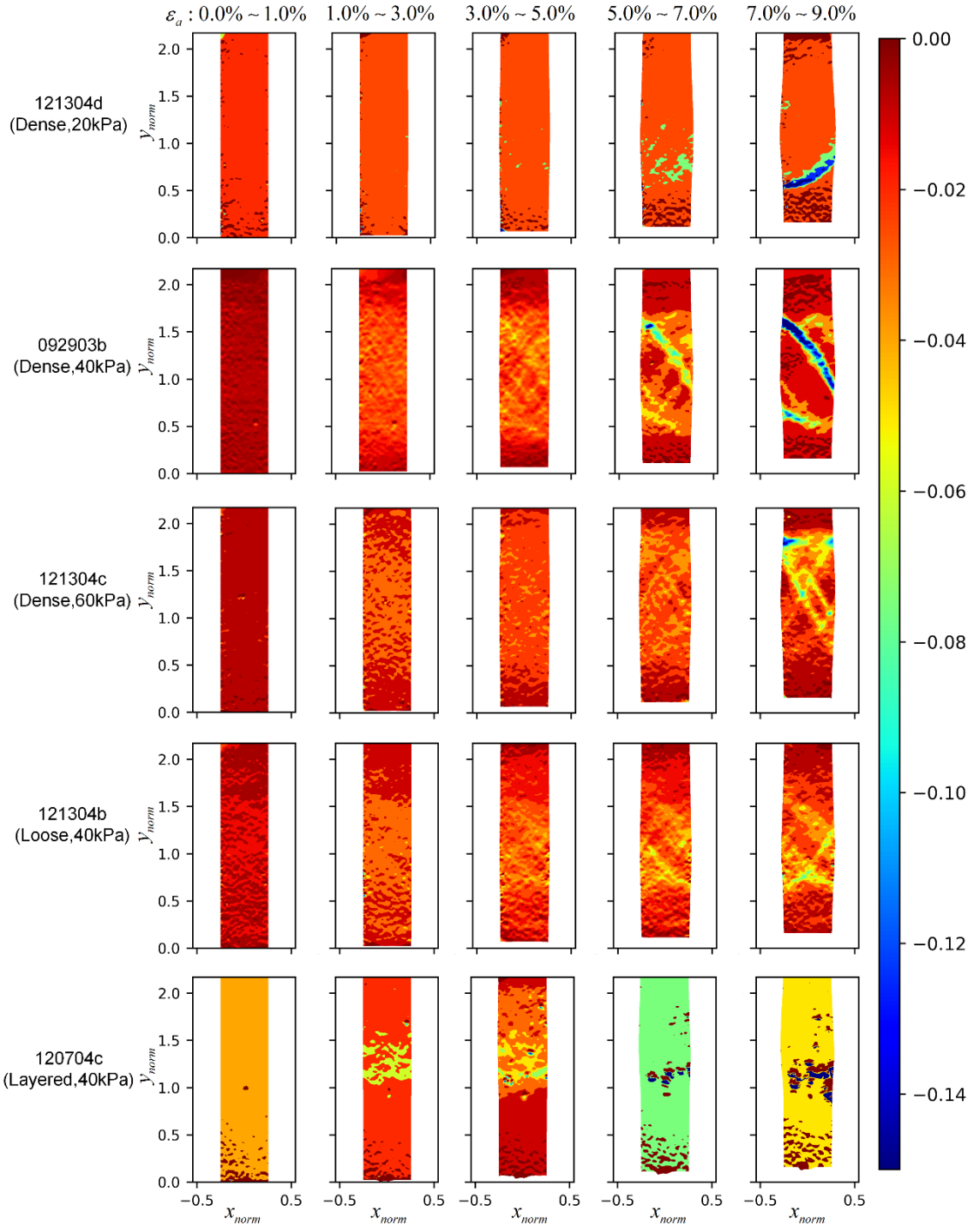

Figure 3.10 Evolution of gradient component along $\hat{y}$ axis of all tests

3.4.4. Spatio-temporal evolution of divergence fields

Figure 3.11 shows the progress of divergence fields based on all testing conditions. For dense specimens, it reveals that local dilation started as early as hardening phase (axial strain 1.0-3.0%) which happened to all three tests. Yet, the later developed compaction bands showed distinct features among different tests. Under low confining pressure (20kPa), the compacting zone is exclusively inside of shear banding area. However, two horizontal compaction bands simultaneously developed after the peak stress when specimen under confinement of 40kPa. Under the confining pressure of 60kPa, two compaction bands seemingly appeared during the strain increment 3.0-5.0%, nonetheless, only one at the top persisted to the end of softening stage. For loose and layered specimens, both volumetric dilation and compaction are mild, which in accordance with our observations in other kinematic fields.

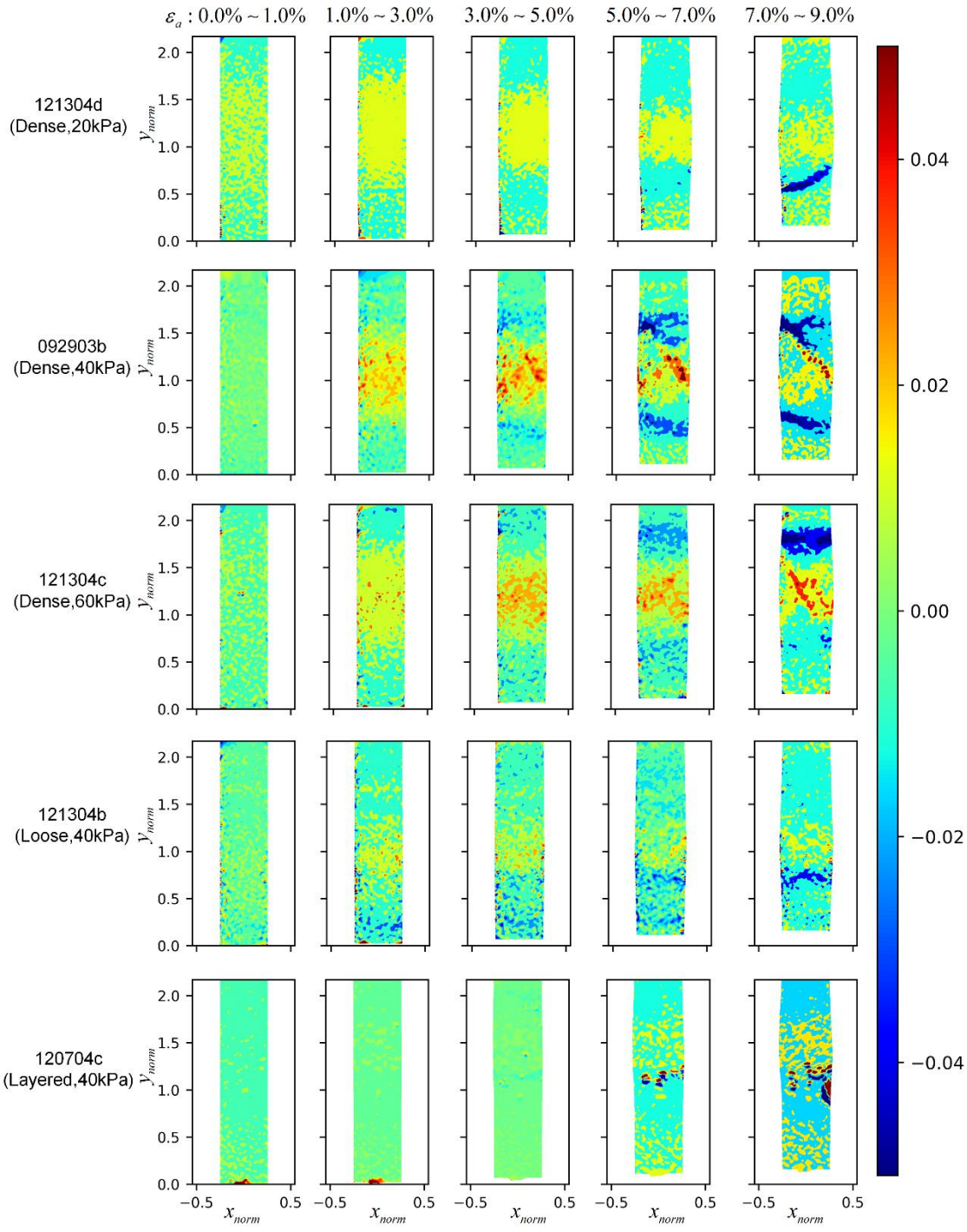

Figure 3.11 Evolution of divergence field of all tests

3.4.5. Spatio-temporal evolution of curl component along $\hat{\rho}$ axis

Finally, we examine the curl component along $\hat{\rho}$ axis which is indicative of rotation with respect to radial axis. This kinematic behaviour is evident within shear band which is caused by intense particle rolling and leads to the formation and collapse of force chains after the peak stress (Oda and Kazama, 1998; Rechenmacher, 2006). Figure 3.12 shows the evolution of this kinematic field occurred to all tests. Under the dense specimen composition, confining pressure is seen playing an important role in determining the shear banding phenomena. Under low confining pressure (first row), shear band developed only at very last stage (7.0-9.0%). On the other hand, the high confining pressure can lead to multiple shear bands progressing simultaneously (third row). For loose and layered specimens, again, no obvious sign of fully developed shear band was observed during all studying periods, suggesting a more homogeneous deformation trend compared to dense speicmens.

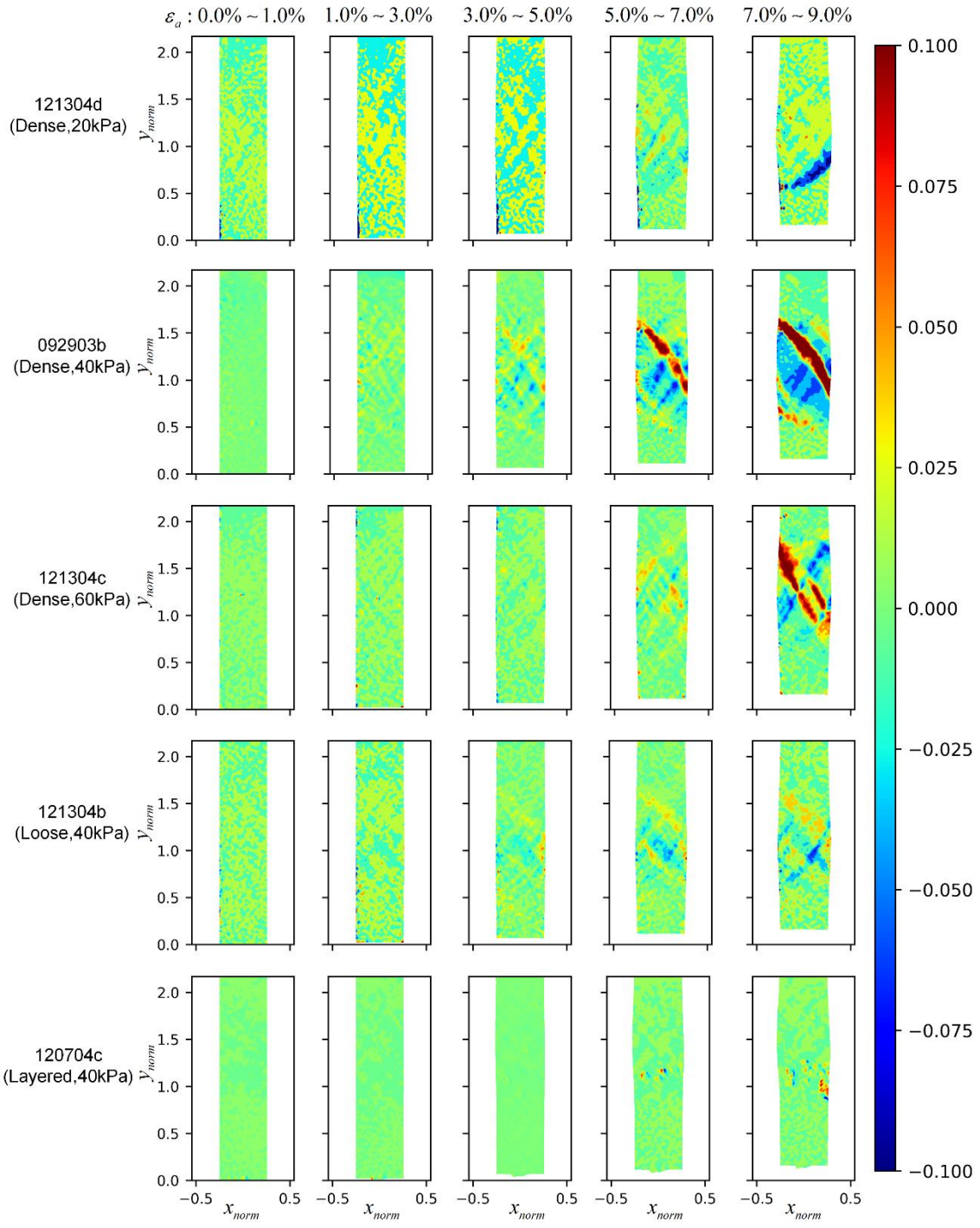

Figure 3.12 Evolution of curl component along $\hat{\rho}$ axis of all tests

3.5. Conclusion

In this paper, a sptio-temporal kinematic analysis has been conducted on a series of triaxial sand specimens sheared under different experimental conditions. This has been achieved by making use of 3D kinematic operators under the Cylindrical coordinates, which can appropriately accommodate specimen geometry. The introduced new tool can faithfully represent 3D meso-scale kinematics occurring to triaxial specimens, and leads to the following conclusions drawn from the calculating results:

(1) The development of expansion band and compaction band are occurred at different temporal windows. Expansion band is seen initiated as early as hardening stage. With strain started softening, the expanding rate was gradually declined, whereas the compaction band began to emerge in the vicinity of expansion band.

(2) When shear band is fully formed, it can alter the radial deformation of specimen according to its shape and orientation. Also, local axial strain become concentrate exclusively within the shear band.

(3) The localization effects is less evident when confinement is low, or experimented on loose specimen. On the other hand, the high confining pressure can lead to multiple shear bands progressing simultaneously.

(4) The kinematic characterization of varying density specimen shows the similar behavior of loose specimen rather than that of dense one. Also, the failure mode is governed by the material response within the loose part of the specimen.

3.6. References

Abedi, S., Rechenmacher, A. L. and Orlando, A. D. (2012) 'Vortex formation and dissolution in sheared sands', *Granular Matter*, 14(6), pp. 695–705. doi: 10.1007/s10035-012-0369-5.

Alonso-Marroquin, F. *et al.* (2006) 'Effect of rolling on dissipation in fault gouges', *Physical Review E*. APS, 74(3), p. 31306.

Alshibli, K. A. *et al.* (2000) 'Assessment of Localized Deformations in Sand Using X-ray Computed Tomography', *ASTM Geotechnical Testing Journal*, 23(3), pp. 274–299.

Alshibli, K. A. and Alramahi, B. A. (2006) 'Microscopic Evaluation of Strain Distribution in Granular Materials during Shear', *Journal of Geotechnical and Geoenvironmental Engineering*, 132(1), pp. 80–91. doi: 10.1061/(ASCE)1090-0241(2006)132:1(80).

Andrade, J. E. *et al.* (2011) 'Multiscale modeling and characterization of granular matter: from grain kinematics to continuum mechanics', *Journal of the Mechanics and Physics of Solids*. Elsevier, 59(2), pp. 237–250.

Bardet, J.-P. and Proubet, J. (1991) 'Adaptative dynamic relaxation for statics of granular materials', *Computers & Structures*. Elsevier, 39(3–4), pp. 221–229.

Borja, R. I. (2000) 'A finite element model for strain localization analysis of strongly discontinuous fields based on standard galerkin approximation', *Computer Methods in Applied Mechanics and Engineering*. Elsevier, 190(11–12), pp. 1529–1549.

Cundall, P. A. and Strack, O. D. L. (1979) 'A discrete numerical model for granular

assemblies', *Geotechnique*, 29(1), pp. 47–65.

Desrues, J. *et al.* (1996) 'Void ratio evolution inside shear bands in triaxial sand specimens studied by computed tomography', *Géotechnique*, 46(3), pp. 529–546. doi: 10.1680/geot.1996.46.3.529.

Desrues, J. and Viggiani, G. (2004) 'Strain localization in sand: An overview of the experimental results obtained in Grenoble using stereophotogrammetry', *International Journal for Numerical and Analytical Methods in Geomechanics*, 28(4), pp. 279–321. doi: 10.1002/nag.338.

Hall, S. A. *et al.* (2010) 'Discrete and continuum analysis of localised deformation in sand using X-ray μCT and volumetric digital image correlation', *Géotechnique*, 60(5), pp. 315–322. doi: 10.1680/geot.2010.60.5.315.

Hall, S. A. *et al.* (2010) 'Localised deformation patterning in 2D granular materials revealed by digital image correlation', *Granular Matter*. Springer, 12(1), pp. 1–14.

Jiang, M. J. *et al.* (2011) 'Modeling shear behavior and strain localization in cemented sands by two-dimensional distinct element method analyses', *Computers and Geotechnics*. Elsevier, 38(1), pp. 14–29.

Liu, J. and Iskander, M. (2004) 'Adaptive cross correlation for imaging displacements in soils', *Journal of Computing in Civil Engineering*. American Society of Civil Engineers, 18(1), pp. 46–57.

Macari, E. J., Parker, J. K. and Costes, N. C. (1997) 'Measurement of volume changes in triaxial tests using digital imaging techniques', *Geotechnical Testing Journal*. ASTM International, 20(1), pp. 103–109.

Matsushima, T. *et al.* (2006) 'Micro X-Ray CT at spring-8 for granular mechanics', in *Soil Stress-Strain Behavior: Measurement, Modeling and Analysis*. New York: Springer, pp. 225–234. doi: 10.1007/978-1-4020-6146-2.

Medina-Cetina, Z. (2006) *Probabilistic calibration of a soil model*. PhD Dissertation. The John Hopkins University, Baltimore, MD.

Medina-Cetina, Z. and Rechenmacher, A. (2010) 'Influence of boundary conditions, specimen geometry and material heterogeneity on model calibration from triaxial tests', *International Journal for Numerical and Analytical Methods in Geomechanics*, 34(6), pp. 627–643. doi: 10.1002/nag.833.

Mohamed, A. and Gutierrez, M. (2010) 'Comprehensive study of the effects of rolling resistance on the stress--strain and strain localization behavior of granular materials', *Granular Matter*. Springer, 12(5), pp. 527–541.

Ng, T.-T. (1994) 'Numerical simulations of granular soil using elliptical particles', *Computers and Geotechnics*. Elsevier, 16(2), pp. 153–169.

Nitka, M. *et al.* (2011) 'Two-scale modeling of granular materials: a DEM-FEM approach', *Granular Matter*. Springer, 13(3), pp. 277–281.

Oda, M. and Iwashita, K. (2000) 'Study on couple stress and shear band development in granular media based on numerical simulation analyses', *International Journal of Engineering Science*, 38(15), pp. 1713–1740. doi: 10.1016/S0020-7225(99)00132-9.

Oda, M. and Kazama, H. (1998) 'Microstructure of shear bands and its relation to the mechanisms of dilatancy and failure of dense granular soils', *Géotechnique*, 48(4),

pp. 465–481. doi: 10.1680/geot.1998.48.4.465.

Rechenmacher, A., Abedi S. and Chupin, O. (2010) ‘Evolution of force chains in shear bands in sands’, *Géotechnique*, 60(5), pp. 343–351. doi: 10.1680/geot.2010.60.5.343.

Rechenmacher, A. L. (2006) ‘Grain-scale processes governing shear band initiation and evolution in sands’, *Journal of the Mechanics and Physics of Solids*, 54(1), pp. 22–45. doi: 10.1016/j.jmps.2005.08.009.

Rechenmacher, A. L. *et al.* (2011) ‘Characterization of mesoscale instabilities in localized granular shear using digital image correlation’, *Acta Geotechnica*, 6(4), pp. 205–217. doi: 10.1007/s11440-011-0147-2.

Rechenmacher, A. L. and Finno, R. J. (2003) ‘Digital Image Correlation to Evaluate ShearBanding in Dilative Sands’, *Geotechnical Testing Journal*, 27(1), pp. 1–10. doi: https://doi.org/10.1520/GTJ11263J.

Song, A. (2012) *Deformation analysis of sand specimens using 3D digital image correlation for the calibration of an elasto-plastic model*. PhD Dissertation. Texas A&M University, College Station, TX.

Sutton, M. A. *et al.* (2000) ‘Advances in two-dimensional and three-dimensional computer vision’, in *Photomechanics*. Springer, pp. 323–372.

Sutton, M. A. *et al.* (2008) ‘The effect of out-of-plane motion on 2D and 3D digital image correlation measurements’, *Optics and Lasers in Engineering*. Elsevier, 46(10), pp. 746–757.

Viggiani, G. *et al.* (2004) ‘X-ray microtomography for studying localized deformation in

fine-grained geomaterials under triaxial compression', *Comptes rendus Mécanique*. Elsevier, 332(10), pp. 819–826.

White, D. J., Take, W. A. and Bolton, M. D. (2003) 'Soil deformation measurement using particle image velocimetry (PIV) and photogrammetry', *Geotechnique*. Thomas Telford Ltd, 53(7), pp. 619–631.

4. STATISTICAL CHARACTERIZATION OF BOUNDARY KINEMATIC PHENOMENA OBSERVED ON TRIAXIAL SAND SPECIMENS

4.1. Introduction

Strain localization in sand is often associated with development of various banding phenomena (e.g., shear or compaction band) that caused by heterogeneous deformational feature of granular materials when subjected to drained compression. In a failure process of geotechnical structures, the differential settlement may occur over a scale of meters. However, the initiation of this process which is known often related to material anomalies and localization effects can happen to a scale of millimetre or smaller (Mulilis *et al.*, 1977; Liang *et al.*, 1997; Rechenmacher and Finno, 2003). This pose a great challenge for engineers to properly characterize and predict the materials behaviour from their constitutive parameters. The conventional solution of this problem is to constitute a '3 in. by 6 in.' soil body in laboratory, and then measure the material response under the controlled experimental conditions needed to estimate constitutive parameters which is assumed also applied to the field scale. However, the global measurements of these tests can yield only volume-averaged deformational characteristics. The inherent non-homogeneous feature of nature sand, and its associated micro failure mechanisms, are smeared out in such analyses and consequently lead to rough or unrealistic representations.

A viable method to overcome this issue is to perform full-field measurements across a deforming body over the course of failure. The common methods in this

category include Discrete-Element Method (DEM), Finite-Element Method (FEM) or multi-scale modelling (Bardet and Proubet, 1991; Borja, 2000; Oda and Iwashita, 2000; Andrade and Borja, 2006; Jiang *et al.*, 2011), X-ray tomography or synchrotron X-ray tomography (Roscoe, 1970; Oda, Takemura and Takahashi, 2004; Alshibli and Alramahi, 2006; Viggiani and Hall, 2008), 2D or 3D digital image correlation (DIC) (Rechenmacher and Finno, 2003; Medina-Cetina, 2006; Hall *et al.*, 2010), among others. Recent trend has been focusing more on linking kinematic aspects of displacement fields with the evolution of failure mechanisms. For example, Oda and Iwashita (2000) used DEM to simulate the micro- and macro behavior of granular media, and concluded that the formation and collapse of column-like structure by means of particle rolling comprise one of the most important kinematic signature after the peak stress. Rechenmacher and her co-workers (2010, 2011, and 2012) quantified the presence and evolution of force chains throughout the softening and critical state by calculating shear, rotational and volumetric kinematic components under plane strain conditions. Alshibli and his team (2016, 2018) identified and tracked the 3D particles translational and rotational behaviours, as well as the evolution of micro shear bands during hardening phase by making use of in-situ synchrotron microcomputed tomography. These work have provided precious insight of micro- or meso-scale kinematics associated with the localization effects.

In spite of advances in sensing techniques provided access to much abundant information of material response at fine scales, however, no research is seen accounting for uncertainty involved in the varying bifurcation process. This absence of knowledge is

critical since non-unique material responses should be expected if testing specimen is viewed as a heterogeneous body. In addition, varying shape, thickness, and angle of shear bands, as well as variation of localizations in temporal domain have been repeatedly reported in many previous research (Desrues and Viggiani, 2004; Song, 2012). The lack of statistical inspection of existing laboratory results inhibits us from better understanding the dominant failure mechanism among many competing ones, as well as the uncertainty evolved in space and time.

In the present paper, the author conducted the first order statistics towards 3D kinematic fields sampled by DIC on 17 nominally similar triaxial tests. Mean and standard deviation fields were investigated over four selected kinematic properties across all tests. The objective is to reveal the prevailing localization mode among various competing ones, as well as uncertainty levels evolved in space and time.

4.2. Laboratory test

4.2.1. Triaxial compression test

Dry sand, classified as SP, was used to constitute the testing specimens for triaxial compression tests. The median particle size is 0.50mm, and coefficients of uniformity and curvature are 2.34 and 1.11 respectively. Table 4.1 presents specimen characteristics of 17 tests and basic statistics of each parameters. The relatively small standard deviation as shown in the bottom row indicates experimental condition was well controlled and all tests were nominally similar in the global sense.

Table 4.1 Summary of specimen characteristics of all participating tests

Test name	Aspect ratio	Initial density (kg/m^3)	Relative density (%)	Friction angle (deg)	Peak (σ_1'/σ_3')	Sample preparation
092903b	2.18	1,710.95	91.09	49.51	7.35	Vibratory compaction
093003b	2.19	1,696.00	85.96	47.98	6.78	Vibratory compaction
100103a	2.21	1,702.22	88.10	48.66	7.03	Vibratory compaction
100103b	2.19	1,717.13	93.18	47.96	6.77	Vibratory compaction
100103d	2.18	1,702.41	88.17	47.37	6.57	Vibratory compaction
100203a	2.20	1,715.32	92.57	48.90	7.12	Vibratory compaction
100203b	2.17	1,711.91	91.41	47.96	6.77	Vibratory compaction
100303b	2.22	1,718.70	93.71	48.56	6.98	Vibratory compaction
120604c	2.25	1,717.48	93.30	48.89	7.11	Vibratory compaction
120904b	2.25	1,720.40	94.28	48.76	5.86	Vibratory compaction
120904c	2.25	1,713.13	91.83	48.77	5.86	Vibratory compaction
120904d	2.24	1,707.89	90.04	47.68	5.44	Vibratory compaction
120904e	2.25	1,718.70	93.71	47.79	5.51	Vibratory compaction
101204a	2.24	1,708.03	90.09	48.03	6.89	Dry pluviation
120604a	2.23	1,721.06	94.50	49.46	7.33	Dry pluviation
120604b	2.25	1,715.13	92.50	48.54	6.98	Dry pluviation
121304a	2.24	1,721.73	94.73	49.30	7.27	Dry pluviation
Basic statistics						
Mean	2.22	1712.83	91.72	48.48	6.68	-
Standard deviation	0.03	7.20	2.45	0.62	0.61	-

The compression process was practically similar to conventional triaxial test. However, the Plexiglas cell was removed and specimen was consolidated at 40kPa confining pressure through vacuum pump. The loading applied to the specimen via the strain control approach ($\dot{\varepsilon} = 0.2\%/\min$) which follows the direction from the bottom up. Two digital cameras placed in front of testing sample, namely Q-Imaging PMI-4201, capturing synchronous images of the deforming specimen at every 0.05% axial strain. Figure 4.1 gives stress-strain and volumetric strain responses of all 17 tests. Since the confining cell was removed, volumetric strain cannot be directly measured and alternatively estimated through digital imaging data as detailed in Song (2012). The dashed intervals indicate strain windows for incremental kinematic analysis, which will be described in below sections.

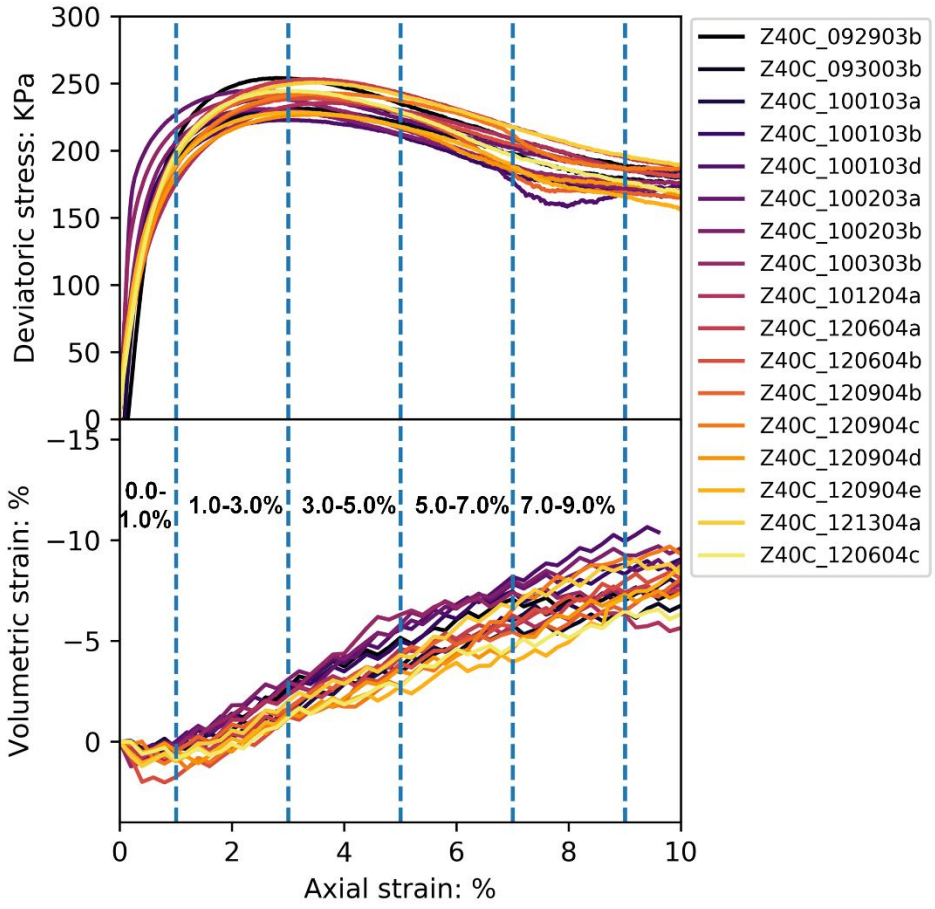

Figure 4.1 Triaxial stress-strain and axial strain-volumetric strain curves of 17 tests. Dashed intervals indicate temporal increments for kinematic analysis.

4.2.2. 3D DIC

DIC is a non-intrusive experimental method to measure displacements on a deforming surface. The basic unit of DIC analysis is a subgroup of image pixels, called subset, which comprised by a cluster of sand colours manifested through the latex specimen membrane in present case. Due to sand grains naturally characterized with colour variations, each subset in stereo images possessing unique mathematical entity that can be easily identified through pattern recognition. In present research, two digital

cameras were setup in front of specimen with different orientation angles while focusing on the common area of the studying surface. The 3D specimen boundary can be constructed through synchronous images capture by these two cameras during the compression, based on the similar principle of how human eyes perceive position and shape of an object. Displacement is derived by mapping the overlapping subsets between two digital images, and consequently the deforming vectors are defined by translational and rotational quantities of subsets in 3D space. Cubic spline interpolation was used to track the trajectory of subsets over several incremental images referenced to the initial material coordinates of interest and accommodated local straining data in a continuum domain. In all, displacement measurements covered a sector about 85 degree around the specimen circumference, and yielded approximate 40,000 displacement vectors with a resolution of 0.4mm from center to center of subsets.

Figure 4.2 plots a typical 3D DIC result of displacement field between global axial strain 3.0% and 9.0%. The contours that indicate displacement intensity (in millimeters) along each axis are superimposed on the deformed body (Eulerian description), specifically, the shape of specimen surface at axial strain 9.0%. First row from left to right shows displacements along horizontal, vertical, and out-of-plane directions. A shear band can be barely observed following diagonal direction, whereas expansion band is clearly depicted in the out-of-plane displacement field. The second row of the plot is the same displacement vector but decomposed under the Cylindrical coordinates, yielded displacement fields along radial, tangential, and axial directions. A shear banding area, suggested by intense clockwise rotation in tangential displacement

field, has been proved prevailed at this stage of loading. Because Cylindrical coordinates can correctly accommodate specimen shape, and the unit vectors under such definition are consistent with principle stress directions (axial and radial), we consequently chose this system for the following kinematic analysis.

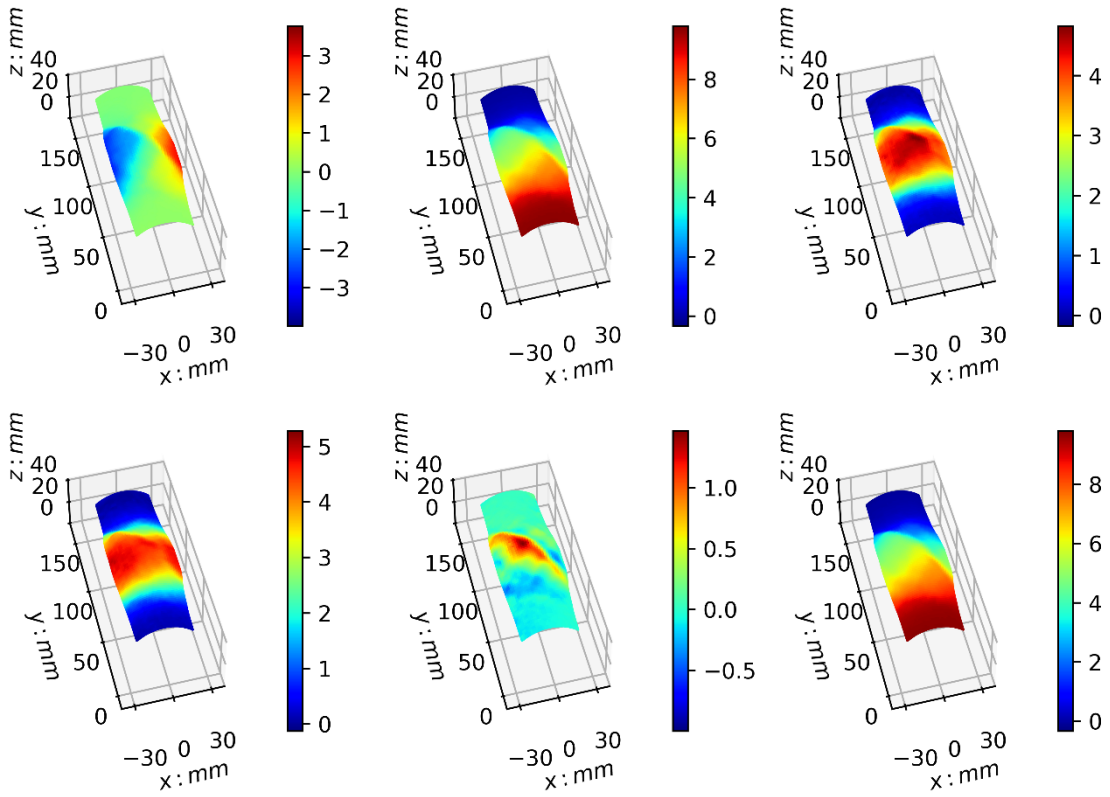

Figure 4.2 (a) Incremental displacement fields of test 092903b between axial strain 3.0% and 9.0%, left to right are displacements along horizontal, vertical and out-of-plane directions; (b) Same displacement field decompose into radial, tangential, and axial directions in Cylindrical coordinates

4.3. 3D kinematics in meso-scale analysis

In this section, we explain 3D kinematic operators under the Cylindrical coordinates and how these can help investigate the onset and evolution of strain

localizations. Equations 4.1 to 4.3 offer the definition of first-order kinematics under the Cylindrical coordinates. The derivation of these quantities is through an operator called *del*, or *nabla*, and its tensor, dot, and cross product with the vector field U. Mathematically, the *gradient* of a 3D vector field is a second-order tensor, which indicate the straining (diagonal) and rotating (off-diagonal) tendency along each direction. A scalar that sums the diagonal terms in F is called *divergence*, which represent volumetric sink or source (negative or positive) of local area. The difference between each two off-diagonal terms in F defines *curl* component along each axis, as expressed in Equation 3. Note under current system, the unit vector $(\hat{\rho}, \hat{\phi}, \hat{z})$ is as a function of position, meaning that they will point to difference directions if two were checked at different locations. Owing to this dynamic setting, the specimen shape is well incorporated and the calculated results can reflect 'authentic' kinematic phenomenon occurred to the curvilinear surface.

$$grad U = [F] = [\nabla \otimes U] = \begin{bmatrix} \frac{\partial U_\rho}{\partial \rho} & \frac{1}{\rho}\left(\frac{\partial U_\rho}{\partial \phi} - U_\phi\right) & \frac{\partial U_\rho}{\partial z} \\ \frac{\partial U_\phi}{\partial \rho} & \frac{1}{\rho}\left(\frac{\partial U_\phi}{\partial \phi} + U_\rho\right) & \frac{\partial U_\phi}{\partial z} \\ \frac{\partial U_z}{\partial \rho} & \frac{1}{\rho}\frac{\partial U_z}{\partial \phi} & \frac{\partial U_z}{\partial z} \end{bmatrix} \tag{4.1}$$

$$div U = \nabla \bullet U = \frac{1}{\rho}\frac{\partial}{\partial \rho}(U_\rho \bullet \rho) + \frac{1}{\rho}\frac{\partial U_\phi}{\partial \phi} + \frac{\partial U_z}{\partial z} \tag{4.2}$$

$$curlU = \nabla \times U = \left(\frac{1}{\rho} \frac{\partial U_z}{\partial \phi} - \frac{\partial U_\phi}{\partial z} \right) \hat{\rho} + \left(\frac{\partial U_\rho}{\partial z} - \frac{\partial U_z}{\partial \rho} \right) \hat{\phi} + \left(\frac{1}{\rho} \frac{\partial}{\partial \rho} \left(U_\phi \cdot \rho \right) - \frac{1}{\rho} \frac{\partial U_\rho}{\partial \phi} \right) \hat{z} \tag{4.3}$$

One challenge in calculating 3D kinematics lies in the difficulty of computing directional derivative along radial direction, since no consecutive measurements beyond boundary is allowed by DIC sampling method. In order to address this issue, we introduce a series of auxiliary origins along axis of specimen, where radial and tangential displacements are assumed zero, and axial displacements are estimated by averaging vertical displacements captured on the specimen boundary at each specimen height. This assumption is supported by experimental evidence revealed in Desrues *et al* (1996), where the localization involves a rigid cone delimited by a circular shear surface, and multiple sets of plane extended outwards from the cone to specimen boundary, implying the radial and tangential displacement along the axis should be insignificant. Figure 4.3 gives the illustration of studying objects, we transform the sampling area from spatial surface to a series of 3D wedges by incorporating this set of auxiliary origins, and, hence, the localization effects can be properly evaluated in the kinematics of these 3D shapes.

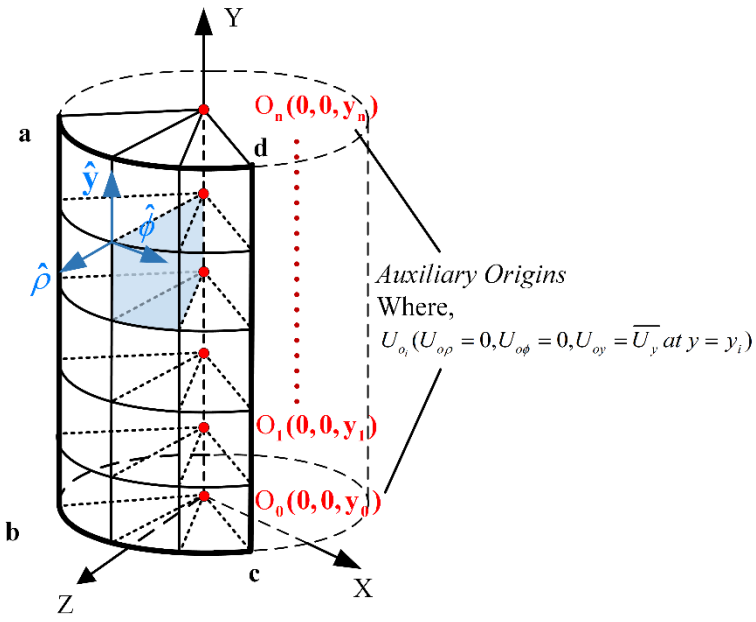

Figure 4.3 Schematic illustration of 3D studying objects that produced by connecting boundary coordinates with introduced auxiliary origins

Figure 4.4 provides an example of nine components of gradient field depicted in Langrangian frame, based on one test's result (092903b) between axial strain 3.0% and 9.0%. Figure 4.5 presents divergence field which is essentially the total of three diagonal terms in Figure 4.4. A clear expansion zone, coupled with two compacting areas are presented in the divergence plot. In addition, the presence of shear band caused local variation of volumetric behavior. Specifically, when shear band coincide with expansion band, it causes great local dilation that is believed associated with intense particle rolling within the shear band (Oda and Iwashita, 2000). However, when shear band intersect compaction band, local volumetric compaction will tend to tremendous as showed within the upper compaction band. This can be explained by F_{33} in Figure 4.4, that local axial compression is seen severe and has outperformed expansion in radial and

tangential directions (F_{11} and F_{22}) which ultimately leads to local volumetric sink in the specific area. Figure 4.6 gives the corresponding curl fields with respect to three axes. Sub-plots (d), (e), and (f) illustrate the positive rotation directions for each case. Shear band is well depicted with intense surface rotation as in the first sub-plot. Moreover, the existence of shear band also caused variations of kinematic fields as shown in the plots of rotational behaviors along other two axes ($\hat{\phi}$ and $\hat{y}$).

4.4. Statistical characterization of 3D kinematics fields

4.4.1. Experimental design

The experimental design of statistical analysis consists of spatial and temporal parts. As mentioned in Figure 4.1, five strain windows, comprised of 0.0 to 1.0%, 1.0 to 3.0%, 3.0 to 5.0%, 5.0 to 7.0%, and 7.0 to 9.0%, are selected as analysing increments of interest. Four kinematic properties, divergence (div), curl along $\hat{\rho}$ axis (curl_ρ), gradient along $\hat{\rho}$ axis (grad_ρ), and gradient along $\hat{y}$ axis (grad_y), are calculated across all tests, as illustrated in Figure 4.7. Then, mean and standard deviation fields will be computed as indicative of prevailing localization mode and inherent uncertainty evolved in space and time. These statistical quantities are intended to plot over material coordinates for each increment. However, because every specimen has its own distinct deforming shape, we take the strategy by averaging specimen shape across all tests and use it as the basis to present statistics of kinematic fields. Note that this does not affect the merit of calculation results, since each kinematic field is computed based on the mesh of specific test. Only final presentation used averaged specimen shape, and it is actually provide further averaged boundary deformation over all tests.

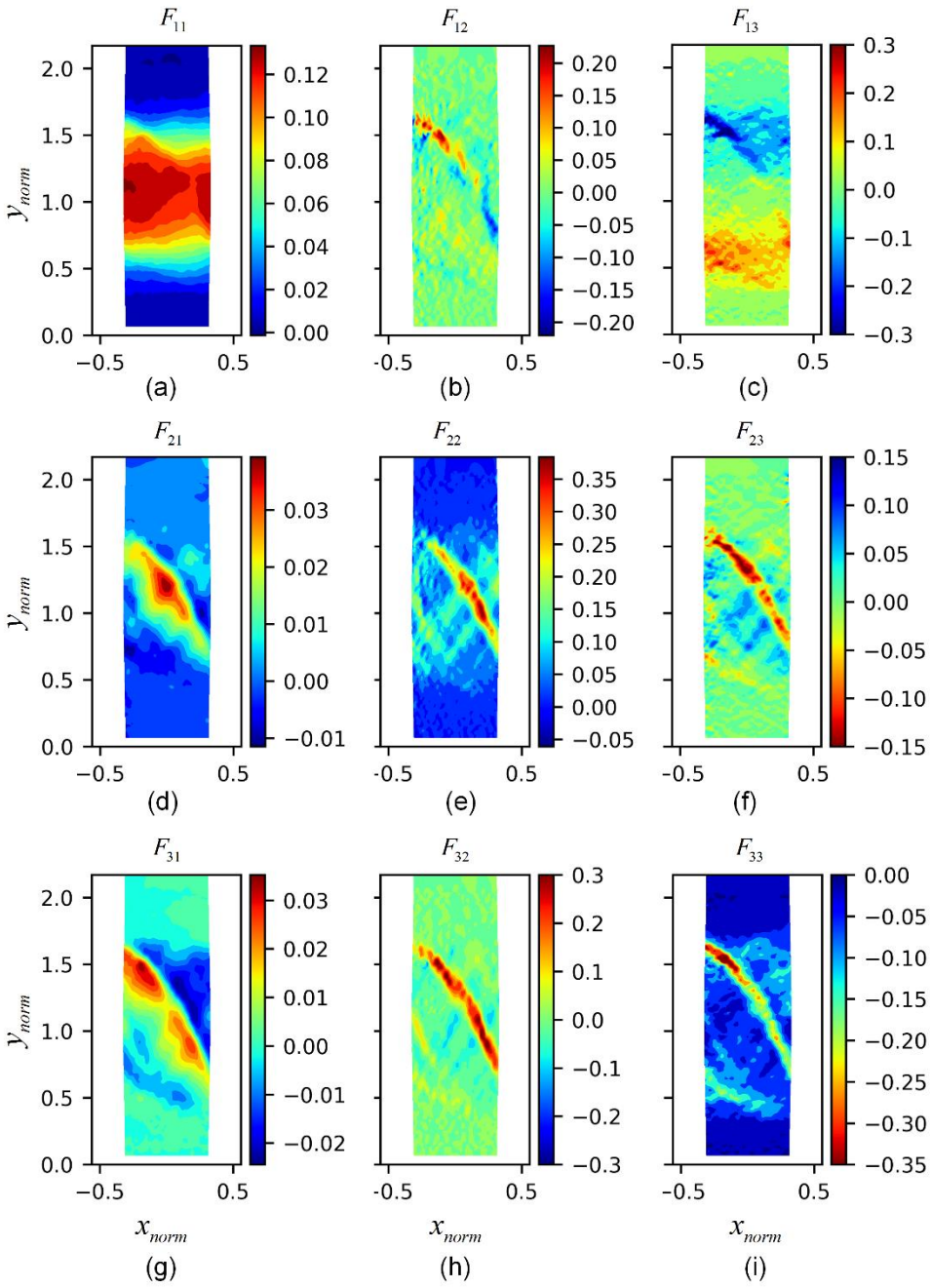

Figure 4.4 Nine components of gradient deformation tensor F based on test 092903b between axial strain 3.0% and 9.0%

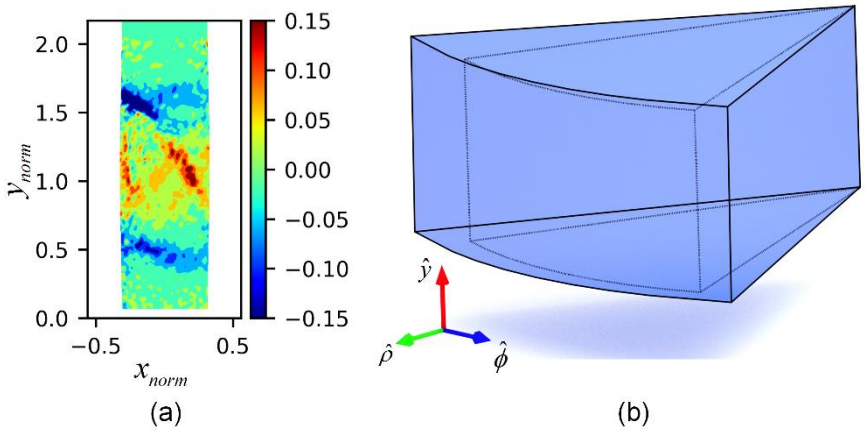

Figure 4.5 Divergence field based on test 092903b between axial strain 3.0% and 9.0%

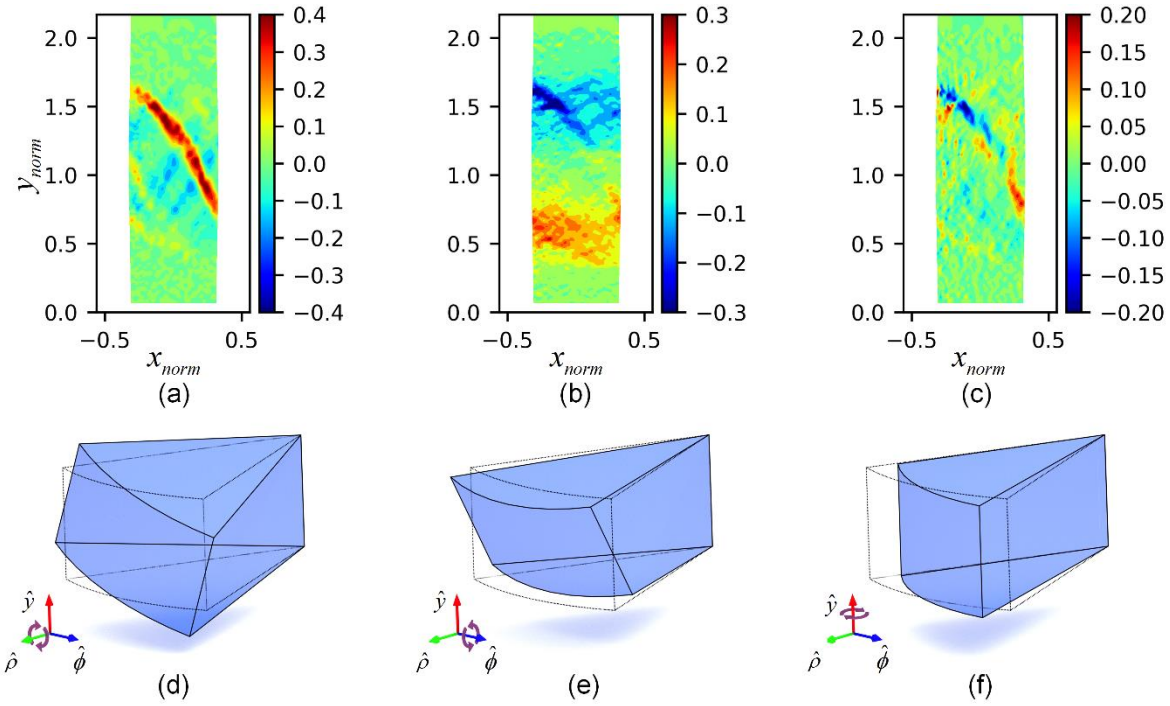

Figure 4.6 Curl components calculated based on test 092903b between axial strain 3.0% and 9.0%: (a) curl field with respect to $\hat{\rho}$ axis; (b) curl field with respect to $\hat{\phi}$ axis; (c) curl field with respect to $\hat{y}$ axis; (d) illustration of positive rotation for curl along $\hat{\rho}$ axis; (e) illustration of positive rotation for curl along $\hat{\phi}$ axis; (f) illustration of positive rotation for curl along $\hat{y}$ axis

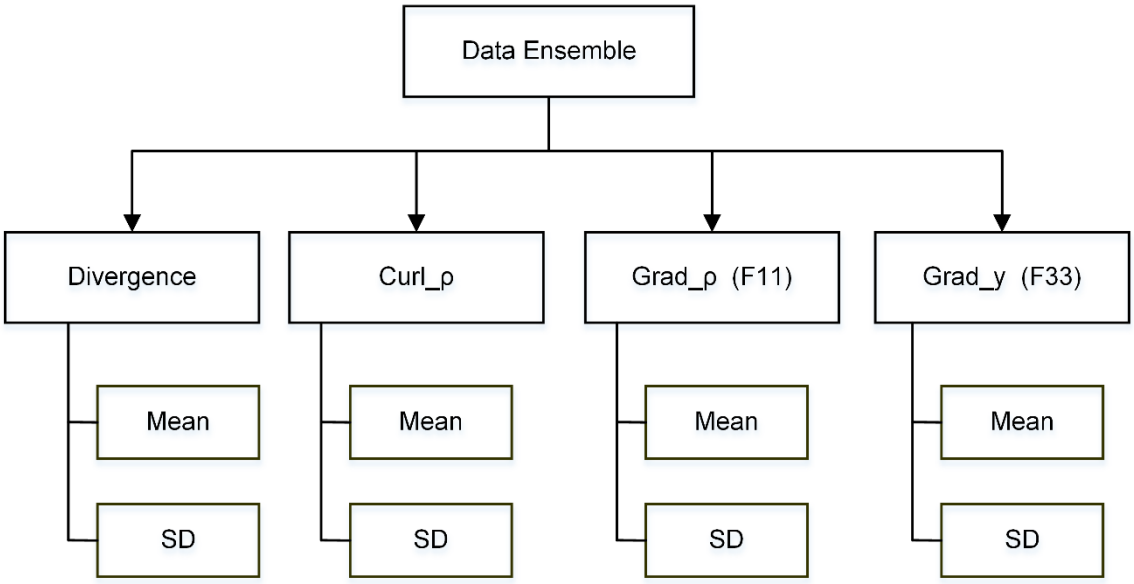

Figure 4.7 Kinematic properties Divergence, Curl_ρ, Grad_ρ (F11), and Grad_y (F33) are selected to be calculated across all tests, and used for statistical analysis

4.4.2. Statistical evolution of divergence field

Figure 4.8 shows spatio-temporal evolution of mean field of divergence calculated from data ensemble. The first row are figures plotted in varying scales, for clear presenting small magnitudes of values especially those during initial steps. Second row are plots in the same scale so that observations evolved in different strain windows can be compared in a consistent framework. It is interesting to see that volumetric behavior takes place in a sequential order. The volumetric dilation, which mainly concentrated at the middle portion, was started as early as elastic regime (0.0-1.0%). Later, the diffuse bifurcation localized in a banding area at the middle of specimen, and step dilation reached its peak around the starting phase of softening (3.0-5.0%). Afterwards, the expanding trend was gradually diminished, and local contraction that manifested as two compaction bands around expansion area became the dominate

volumetric phenomenon of the specimen. It may indicate the compaction zone is essentially mobilized energy formerly accumulated in the middle expansion band, and leads to the softening of specimen in the global sense. Figure 4.9 presents evolution of standard deviation of divergence fields across all tests. It shows uncertainty is mainly reflected within compaction band, while not much associated with expansion band. This agrees well with our observation of post-mortem specimens in which the majority are expanded in the middle, but due to varying shear bands and other issues (e.g., imperfection of initial specimen shape), the curvature from maximum bulging point to the end of the specimen is varying from test to test.

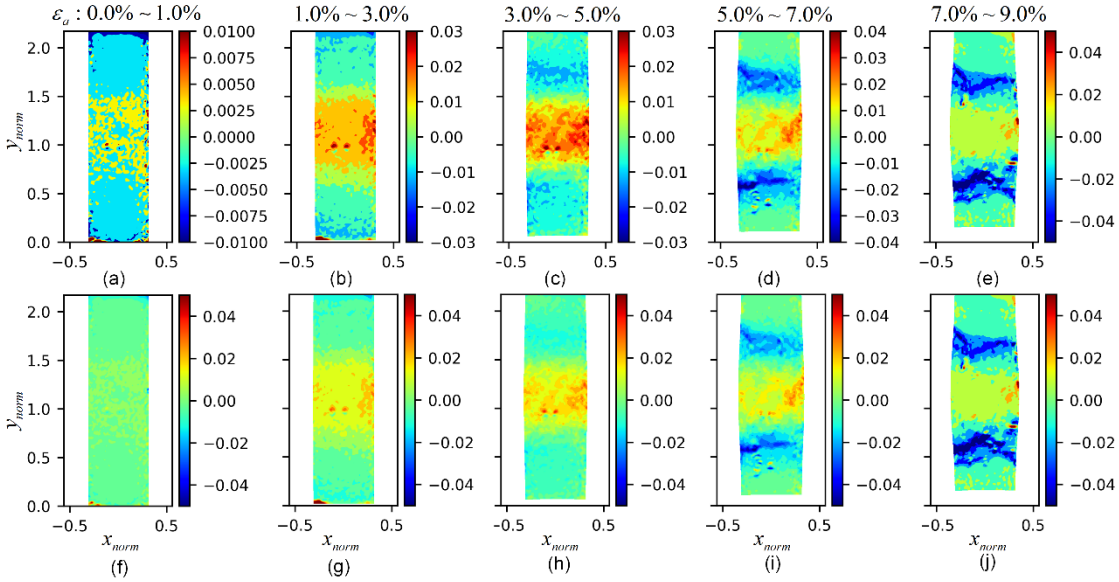

Figure 4.8 Evolution of mean of divergence field derived from data ensemble: the first row are plots in varying scales, while the second row is consistent with same scale (the rest figures in this paper follow the same fashion)

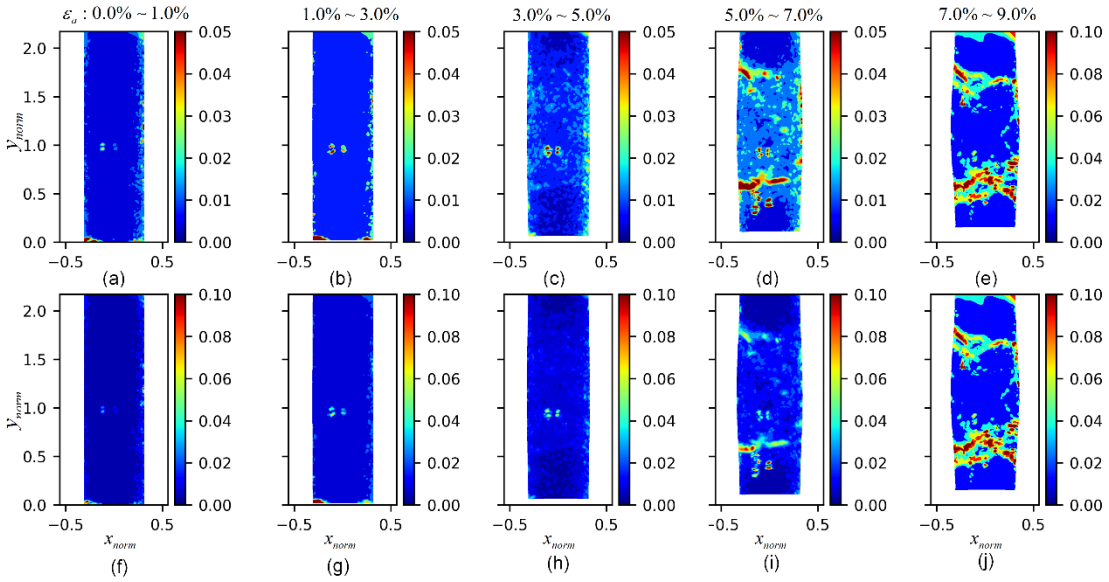

Figure 4.9 Evolution of standard deviation of divergence field derived from data ensemble

4.4.3. Statistical evolution of curl along $\hat{\rho}$ axis

Figure 4.10 and 4.11 give the evolution of mean and standard deviation fields of curl along $\hat{\rho}$ (radial) axis. In Figure 4.10, although strain bifurcation initiated from hardening stage (1.0-3.0%), it is not obvious of localization effects until post-peak reached (after 3.0%). Totally three shear banding areas exhibited at the last frame, and they are seen varying with inclination angles. Specifically, the shear band is oriented straighter when it appears to the middle of specimen compared to the upper and lower parts. This agrees well with previous observation made by Oda and Kazama (1998) through X-ray method, suggesting that shear band boundaries are gently curved with variation of the inclination angles. The standard deviation fields (Figure 4.11) indicate that rotational uncertainty is also highlighted along the shear bands, suggesting that after

the peak stress, varying strain localizations comprise the main uncertainty of failure mechanism.

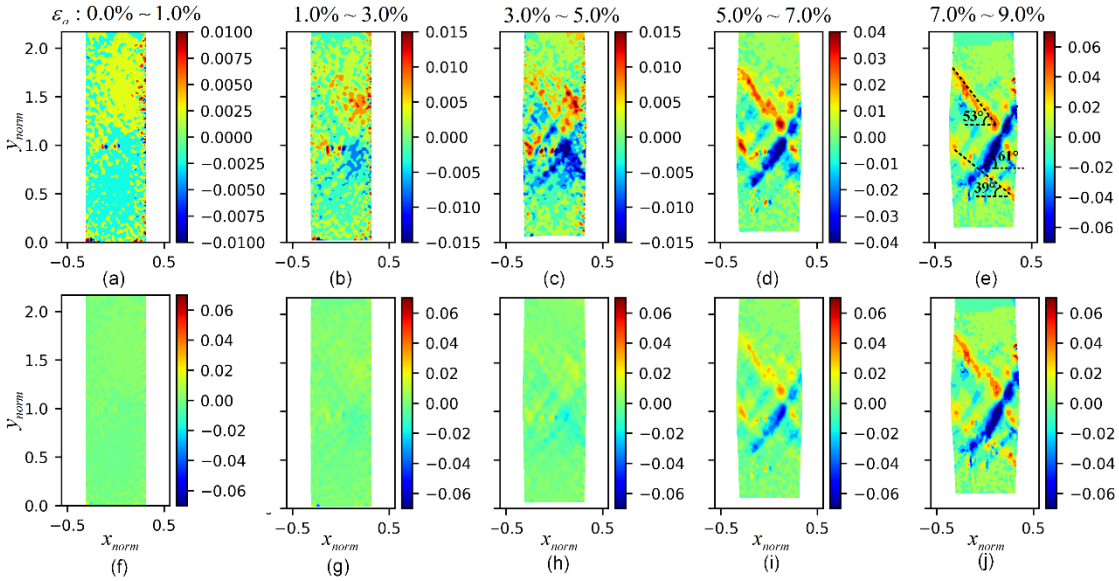

Figure 4.10 Evolution of mean of curl field along $\hat{\rho}$ axis

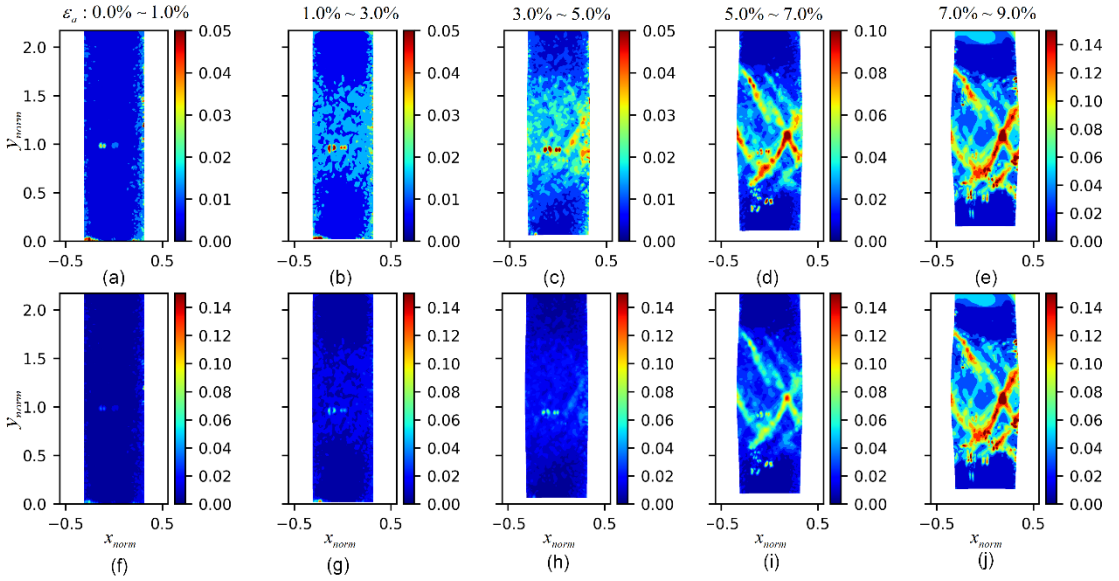

Figure 4.11 Evolution of standard deviation of curl field along $\hat{\rho}$ axis

4.4.4. Statistical evolution of gradient along $\hat{\rho}$ axis

Figure 4.12 and 4.13 show the evolution of mean and standard deviation fields of gradient along $\hat{\rho}$ (radial) axis. Since this quantity denotes radial deformation tendency, it explicitly signifies the development of expansion band. Figure 4.12 shows qualitatively similar trend as the divergence plot we described in Figure 4.8, that a middle expanding zone would keep growing from elastic to early softening stage, but the rate gradually declined once other localization effects become apparent, such as shear band and compaction band. It is also worth noting that the horizontal distribution of radial gradient transformed from uniform to irregular shape during this process. Figure 4.13 shows when expansion band is well formed, the uncertainty distribution will present with a basin shape that higher values arisen in the periphery of the maximum bulging point, suggesting again the curvature of expanding profile rather than the maximum expanding point compose the main uncertainty in terms of radial deformation.

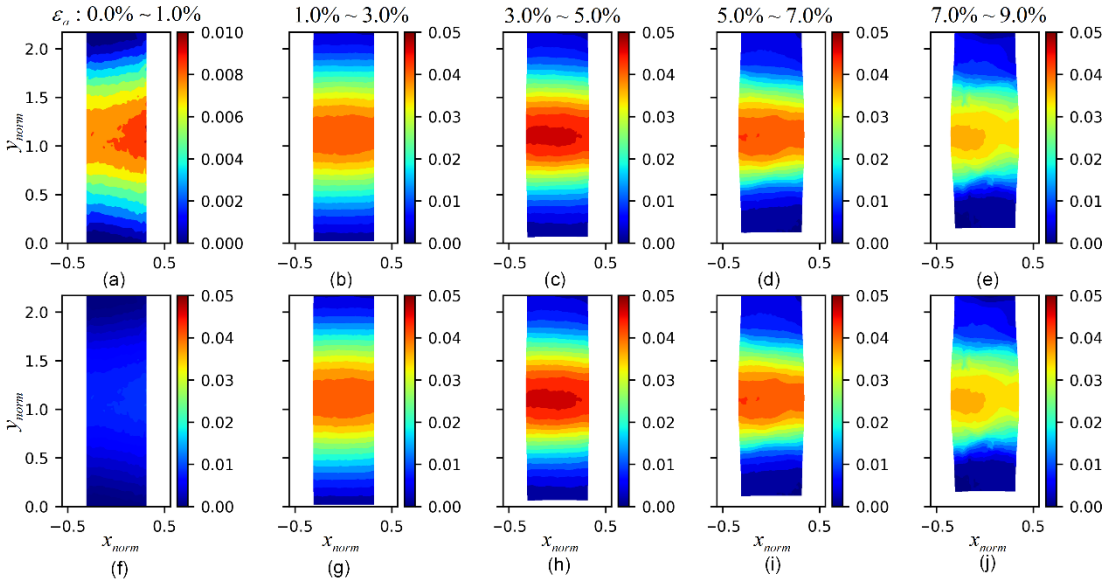

Figure 4.12 Evolution of mean field of gradient along $\hat{\rho}$ axis

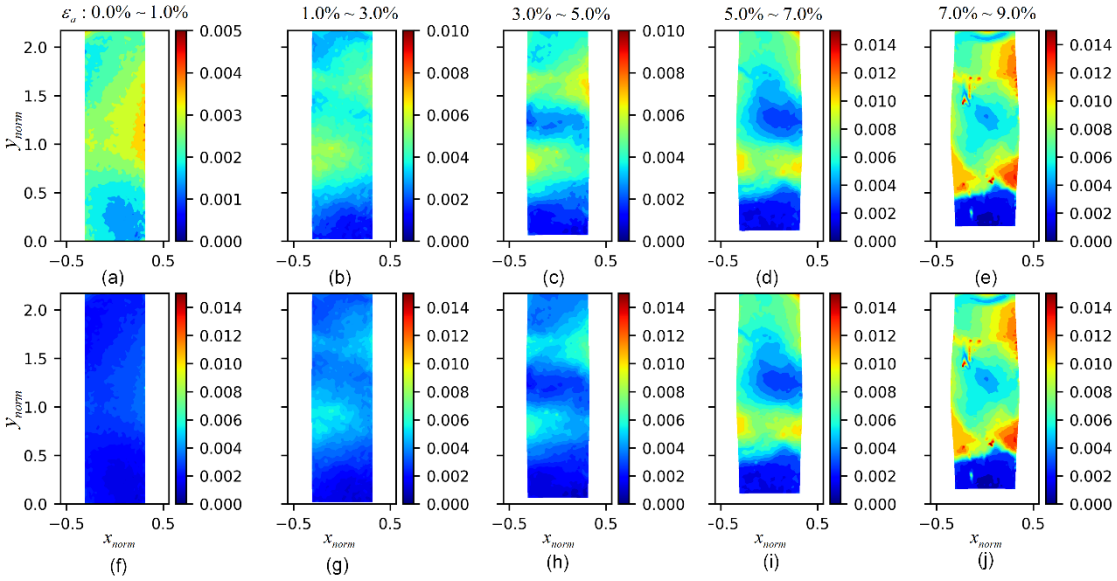

Figure 4.13 Evolution of standard field field of gradient along $\hat{\rho}$ axis

4.4.5. Statistical evolution of gradient along $\hat{y}$ axis

Gradient field along $\hat{y}$ axis specifies local deformations following axial direction. Figure 4.14 shows an intense axial compression zone coincided with radial deformation area that emerged in the hardening phase, however, the localization effects appeared only after the peak state (around axial strain 3.0%). Additionally, in later softening stage, such effects only evident inside of shear bands. The standard deviation plot is similar to that for curl_ρ field, which shows uncertainty is exclusively within the shear banding area. These combined evidence suggests particle rolling with respect to radial axis, and compression along axial direction should be main kinematic signatures of the shear band. Its relationship with the form and collapse of force chains, and the spatio-temporal distribution warrants discussion in our future work.

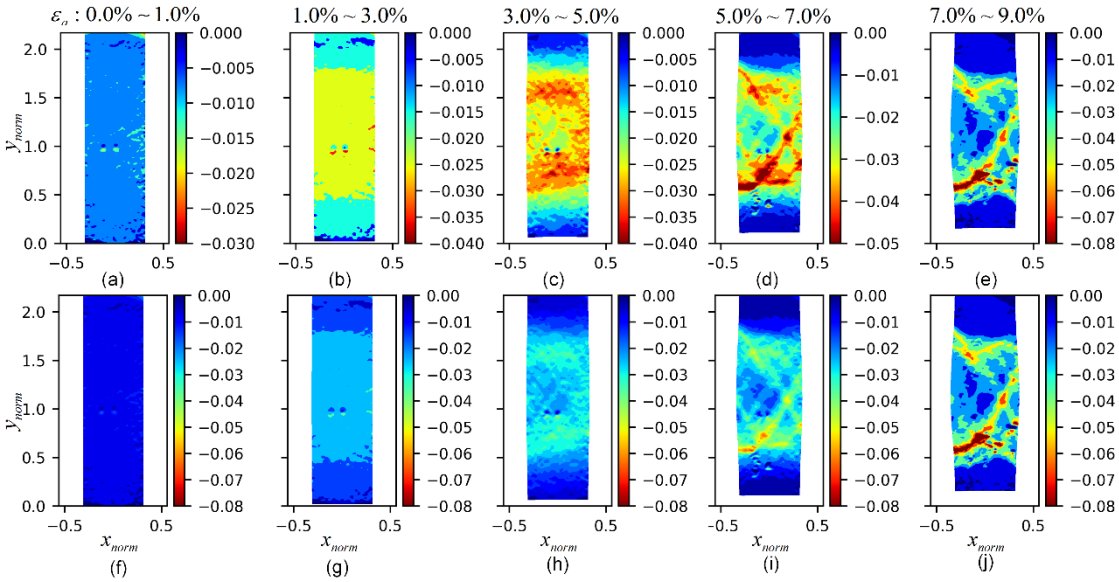

Figure 4.14 Evolution of mean field of gradient along $\hat{y}$ axis

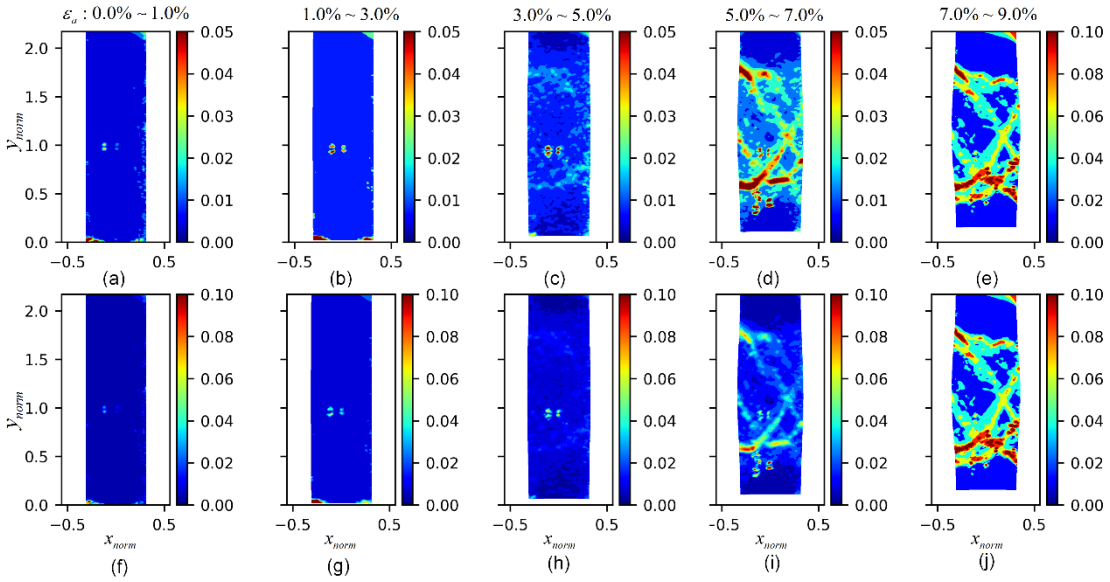

Figure 4.15 Evolution of standard deviation of gradient along $\hat{y}$ axis

4.5. Conclusion

Spatio-temporal statistical characterization was carried on a series of kinematic fields generated from 17 nominally similar triaxial compression tests. Herein, we calculated mean and standard deviation over four kinematic quantities-divergence, curl along radial axis, gradient along radial axis, and gradient along axial axis. The main contribution of this work is summarized as follows:

(a) During triaxial compression, local volumetric behavior takes place in a sequential order. The local dilation mainly in the middle of specimen is evident from hardening to peak state. Later, the onset of other localization effect, such as shear or compaction band, mobilized energy formerly accumulated and leads to the softening of specimen.

(b) Shear band appears to the specimen surface is seen varying with inclination angles. After the peak stress, the rotational uncertainty is localized within the shear banding area, suggesting varying strain localizations comprise the main source of uncertainty at this stage.

(c) The development of shear band can influence radial change of specimen. In addition, the curvature of expanding profile rather than the maximum expanding point represents the main uncertainty of radial deformation.

(d) Particle rolling with respect to radial axis, and compression along axial direction characterize the main kinematic signatures of the shear band. The spatio-temporal relationship of these two properties warrants further discussion in our ongoing work

4.6. References

Abedi, S., Rechenmacher, A. L. and Orlando, A. D. (2012) 'Vortex formation and dissolution in sheared sands', *Granular Matter*, 14(6), pp. 695–705. doi: 10.1007/s10035-012-0369-5.

Alshibli, K. A. *et al.* (2000) 'Assessment of Localized Deformations in Sand Using X-ray Computed Tomography', *ASTM Geotechnical Testing Journal*, 23(3), pp. 274–299.

Alshibli, K. A. *et al.* (2016) 'Influence of Particle Morphology on 3D Kinematic Behavior and Strain Localization of Sheared Sand', *Journal of Geotechnical and Geoenvironmental Engineering*, 143(2), p. 04016097. doi: 10.1061/(ASCE)GT.1943-5606.0001601.

Alshibli, K. A. and Alramahi, B. A. (2006) ‘Microscopic Evaluation of Strain Distribution in Granular Materials during Shear’, *Journal of Geotechnical and Geoenvironmental Engineering*, 132(1), pp. 80–91. doi: 10.1061/(ASCE)1090-0241(2006)132:1(80).

Amirrahmat, S. *et al.* (2018) ‘Micro Shear Bands: Precursor for Strain Localization in Sheared Granular Materials’, *Journal of Geotechnical and Geoenvironmental Engineering*. American Society of Civil Engineers, 145(2), p. 4018104.

Andrade, J. E. and Borja, R. I. (2006) ‘Capturing strain localization in dense sands with random density’, *International Journal for Numerical Methods in Engineering*, 67(11), pp. 1531–1564. doi: 10.1002/nme.1673.

Bardet, J.-P. and Proubet, J. (1991) ‘Adaptative dynamic relaxation for statics of granular materials’, *Computers & Structures*. Elsevier, 39(3–4), pp. 221–229.

Borja, R. I. (2000) ‘A finite element model for strain localization analysis of strongly discontinuous fields based on standard galerkin approximation’, *Computer Methods in Applied Mechanics and Engineering*. Elsevier, 190(11–12), pp. 1529–1549.

Desrues, J. *et al.* (1996) ‘Void ratio evolution inside shear bands in triaxial sand specimens studied by computed tomography’, *Géotechnique*, 46(3), pp. 529–546. doi: 10.1680/geot.1996.46.3.529.

Desrues, J. and Viggiani, G. (2004) ‘Strain localization in sand: An overview of the experimental results obtained in Grenoble using stereophotogrammetry’, *International Journal for Numerical and Analytical Methods in Geomechanics*, 28(4), pp. 279–321. doi: 10.1002/nag.338.

Hall, S. A. *et al.* (2010) ‘Discrete and continuum analysis of localised deformation in sand using X-ray μCT and volumetric digital image correlation’, *Géotechnique*, 60(5), pp. 315–322. doi: 10.1680/geot.2010.60.5.315.

Jiang, M. J. *et al.* (2011) ‘Modeling shear behavior and strain localization in cemented sands by two-dimensional distinct element method analyses’, *Computers and Geotechnics*. Elsevier, 38(1), pp. 14–29.

Liang, L. *et al.* (1997) ‘The use of digital image processing in monitoring shear band development’, *Geotechnical Testing Journal*. ASTM International, 20(3), pp. 324–339.

Medina-Cetina, Z. (2006) *Probabilistic calibration of a soil model*. The John Hopkins University, Baltimore, MD.

Mulilis, J. P. *et al.* (1977) ‘Effects of sample preparation on sand liquefaction’, *Journal of the Geotechnical Engineering Division*. ASCE, 103(2), pp. 91–108.

Oda, M. and Iwashita, K. (2000) ‘Study on couple stress and shear band development in granular media based on numerical simulation analyses’, *International Journal of Engineering Science*, 38(15), pp. 1713–1740. doi: 10.1016/S0020-7225(99)00132-9.

Oda, M. and Kazama, H. (1998) ‘Microstructure of shear bands and its relation to the mechanisms of dilatancy and failure of dense granular soils’, *Géotechnique*, 48(4), pp. 465–481. doi: 10.1680/geot.1998.48.4.465.

Oda, M., Takemura, T. and Takahashi, M. (2004) ‘Microstructure in shear band observed by microfocus X-ray computed tomography’, *Géotechnique*, 54(8), pp.

539–542. doi: 10.1680/geot.2004.54.8.539.

Rechenmacher, A., Abedi S. and Chupin, O. (2010) ‘Evolution of force chains in shear bands in sands’, *Géotechnique*, 60(5), pp. 343–351. doi: 10.1680/geot.2010.60.5.343.

Rechenmacher, A. L. *et al.* (2011) ‘Characterization of mesoscale instabilities in localized granular shear using digital image correlation’, *Acta Geotechnica*, 6(4), pp. 205–217. doi: 10.1007/s11440-011-0147-2.

Rechenmacher, A. L. and Finno, R. J. (2003) ‘Digital image correlation to evaluate shear banding in dilative sands’, *Geotechnical Testing Journal*. ASTM International, 27(1), pp. 13–22.

Roscoe, K. H. (1970) ‘The Influence of Strains in Soil Mechanics’, *Géotechnique*, 20(2), pp. 129–170. doi: 10.1680/geot.1970.20.2.129.

Song, A. (2012) *Deformation analysis of sand specimens using 3D digital image correlation for the calibration of an elasto-plastic model*. PhD DissertationTexas A&M University, College Station, TX.

Viggiani, G. and Hall, S. A. (2008) ‘Full-field measurements, a new tool for laboratory experimental geomechanics’, in *Fourth symposium on deformation characteristics of geomaterials*, pp. 3–26.

5. BAYESIAN PROBABILISTIC CALIBRATION OF A VISCO-ELASTOPLASTIC MODEL REPRESENTING THE RHEOLOGICAL BEHAVIOR OF SANDSTONE

5.1. Introduction

Landslides represents one of the most concerning geological hazard in Three Gorges Reservoir area (Deng *et al.*, 2000; Highland, 2008; Jiang and Zhou, 2013). Since first water impoundment in 2003, more than 5,000 landslides has been identified (Hu *et al.*, 2015) in which a great number are found attributed to long-term gravitational deformation of rock mass (Wang *et al.*, 2004, 2008; Jian, Wang and Yin, 2009), which is known can cause the stratum instability in the process of toppling or deep-seated creep (Wang *et al.*, 2004). In contrast to spectacular short-time slide, the process of rock creep can goes on for years or centuries without noticeable phenomenon. However, the induced adverse effects, as shown by previous studies, could decrease rock strength by the order of magnitude of 40-60% compared to its short-term strength (Damjanac and Fairhurst, 2010; Deng *et al.*, 2016), conditioned on the influence factors such as seating depth, thermo-hydrological conditions, initial defects of rocks, among others (Heap *et al.*, 2009; Brantut *et al.*, 2013). It is clear that a better understanding of creep nature is of practical need in optimizing stabilizing-slide design, which can help avoid or at least reduce the threat of landslides occurrence, in particular considering very densely populated area such as Three Gorge Reservoir that even a moderate landslide can entail enormous human and property losses (Highland, 2008).

The specific rock type studied in the present research is chosen as Jurassic sandstone, which is widely distributed around reservoir riverbanks and its acting sliding depth varying from 15 to 70 m (Xu, Yang and Chu, 2006; Li, Yin and Leo, 2010; Hu *et al.*, 2015). Some authors have studied creep behavior of sandstone under the confinement of 10-60 MPa (Tsai *et al.*, 2008; Weng *et al.*, 2010; Zheng, X. Feng and Hao, 2015), yet the results cannot be directly referred to the present work since the sandstones sampled in this work were confined under low pressures according to their in-situ buried depth as mentioned above. Note it has been demonstrated that higher confining pressure can significantly inhibit stress erosion in sandstones, and reduce the creep strain rate by multiple orders of magnitude (Heap *et al.*, 2009). It is consequently suggest the accurate laboratory approximation of sandstone's creep behavior in the nature environment needs to be carried out with the maximum restoration of its original low confinement conditions. Such experimental effort is only seen in Cong Lu and Hu Xinli (2017) amidst many recent studies, where triaxial compression tests and triaxial creep tests were conducted under a set of confining pressures consisting of 3.0 MPa, 5.0 MPa, and 7.0 MPa, to investigate time-dependent behavior of sandstone in Three Gorges area. These experimental observations as a result were adopted in this work, to calibrate proposed creep constitutive model and subsequently assessed as a participating source of evidence in an uncertainty quantification framework.

The creep constitutive model proposed in this paper were established by combination of different mechanical components, including Hooke spring (elastic behavior), Newtonian dashpot (viscous behavior), and plastic body. Theoretically, one

can simulate any visco-elastoplastic behavior of material by appropriate arrangement of above components, following the assumption that each rock property can be represented independently. This methodology provides great flexibility in describing complex solid rheological behavior and thus was widely embraced by rock rheology community. For instance, Boukharov et al.(1995) proposed a stress-triggered component model to describe three stages deformation of brittle rock (elastic, plastic and dilatant deformations). Xu et al.(2015) introduced a seven-component rheological model (Hohai model), and validated by the experimental and numerical modeling observations through rock creep tests and FLAC^{3D} simulations. Zheng et al.(2015) modified Burger's model by introducing a volumetric creep component to illustrate the visco-elastic volumetric behavior. And Jiang et al.(2013), added a strain-triggered inertial element into Nishihara model to describe the quadratic accelerating creep of sandstone. Note that characterization of these model parameters are usually estimated by deterministic search engine, or simply put, deterministic calibration. Its outcome is typically composed of a single vector of parameter values that are chosen following the principle of minimizing the difference between model predictions and experimental observations. By such definition, this approach carries little interest to quantify uncertainty may inherent in experimental observations, model predictions, or even experts' beliefs. More importantly, the calibrated result may merely represent one realization among millions of other combinations of model parameters that can yield the same likelihood of hitting the same set of experimental observations (i.e., ill-posed problem). Under such circumstances, the interpretation of deterministically calibrated constitutive parameters,

and further the physical process of interest, could become less convincing or even misleading.

The main goal of this paper is to improve the understanding of sandstone's rheological behavior under low confining pressures by systematically assimilate information from different participating sources, which include laboratory creep tests, constitutive model simulations, and the prior knowledge about model parameters. A key aspect of the present research structure grounded on the basis of probability theory, to quantify the level of uncertainty inherent in each participating source, and thereby reveal the state of evidence that one can integrate into his/her understanding of process of interest. In this work, the rheological model parameters are treated as *random* rather than *unknown*-such rendering representing one of main characteristics separating *Bayesianism* from *frequentism*-to assimilate evidence uncertainty stemmed from each participating source through *Bayesian* paradigm. Under this framework, the state of knowledge about rheological parameters (i.e., prior distribution), and the knowledge denoting the tradeoff between creep tests observations and model predictions (i.e., likelihood distribution) were numerically integrated, and signified by the updated variation range and modes of model governing parameters in the probability space (i.e., posterior distribution). This scheme is often referred as the probabilistic calibration of inverse problem, and has gained increasing relevance in geotechnical community evidenced by a variety of applications (Medina-Cetina, 2006; Medina-Cetina *et al.*, 2013; Medina-Cetina and Arson, 2014; Ranalli *et al.*, 2014; Esmailzadeh *et al.*, 2015; Zhu *et al.*, 2017). However, far too little attention has paid to applications regarding the

characterization of rock rheological behavior, the research area that we believe exhibited with great uncertainty no matter in current theoretical or experimental endeavors.

One major impact that can be generated by probabilistic calibration lies in its ability to explore the entire probability domain for model parameters, which promotes the inference level from point estimation to full description of probability distribution. The Metropolis-Hastings (MH) algorithm was used for this study to ensure the sampling of parametric space satisfying the detailed balance criterion, and the computational simulation of different combination of parameter samples was implemented via the Monte-Carlo (MC) approach (Metropolis *et al.*, 1953; Hastings, 1970; Gelman *et al.*, 2013). Once the numerical integration reaches the stationary level, results are expected to show the complete joint probability distribution of model parameters (i.e. posterior distribution), which in this case are composed of constitutive parameters defined in each model component. The aforementioned ill-posed problem, can be resolved by showing multiple modes of posterior distribution concentrated at different values simultaneously. The degree of uncertainty, as well as the correlation structure of each potential mode, can be directly observed from the posterior distribution. Additionally, through the transparent definition of the posterior, we can draw parameter samples to populate model simulations that will further inform us expected outcomes and confidence levels of model predictions, and consequently, offer us a comprehensive insight pertaining to rheological behavior of sandstone sampled from the site of interest.

The paper is organized in four parts: at the beginning, we provide a brief description of laboratory tests conducted, including triaxial compression test and triaxial

creep test, to inform the experimental evidence in our probabilistic calibration framework. The proposed constitutive creep model, representing the model evidence, is following introduced. Then we will present the details of the probabilistic approach to inverse problem, also the experimental design of the present problem. Finally, the paper is concluded based on obtained calibration results and the corresponding physical interpretation that can be used to further our understanding of rock creep phenomenon.

5.2. Laboratory tests

5.2.1. Triaxial compression test

The experimental study was carried out at China University of Geosciences, comprising triaxial compression tests and creep tests that were lasted totally four months. Details report of this study are presented in Cong Lu and Hu Xinli (Cong and Hu, 2017), herein only main processes and results are introduced for completeness.

The testing Jurassic sandstone samples were collected from the bedrock of Majiagou landslide, 20 miles upstream from Three Gorges Dam, and 40m underneath of ground surface. To circumvent sample variation, we conducted acoustic-wave test and only those results fell in a narrow range (2500m/s~3000m/s) were selected to proceed to testing phase. The confining pressure are chosen as 3MPa, 5MPa, and 7MPa, to correspond the in-situ sliding depth range from 15 to 70m. The Laboratory tests was started from the characterization of short-term strength σ_c, by performing the triaxial compression test, these were obtained under different confining pressures. As shown in Figure 5.1, the short-term strengths σ_c under three different confining pressures are 85.6, 110, and 160MPa, respectively. Also, the short-term yield stresses σ_s were

measured as 62, 74, and 114MPa, respectively. Next step, a series of creep loading stresses are determined by multiplying different coefficients to sandstone's short-time strength, such that $0.5\sigma_c$, $0.55\sigma_C$, $0.6\sigma_c$, …, and this set of deviatoric stresses were then applied in the creep test. Since the variation of sample's initial defects can exert great influence on sandstone's time-dependent behaviour (Heap *et al.*, 2009), stress-stepping loading strategy was adopted in which multiple brittle creep experiments were performed on one single sample. Specifically, in this research, ascending loading stresses were applied to sandstone sample in a stepwise manner. During each loading step, the deviatoric stress was hold as invariant when sample undergoing creep deformation. Keeping this stress-static condition until strain rate is seen stabilized, the next level loading stress was then ready to apply. This process was iterated until a clear failure was observed on testing sample. The specific loading sequences are presented in Table 5.1.

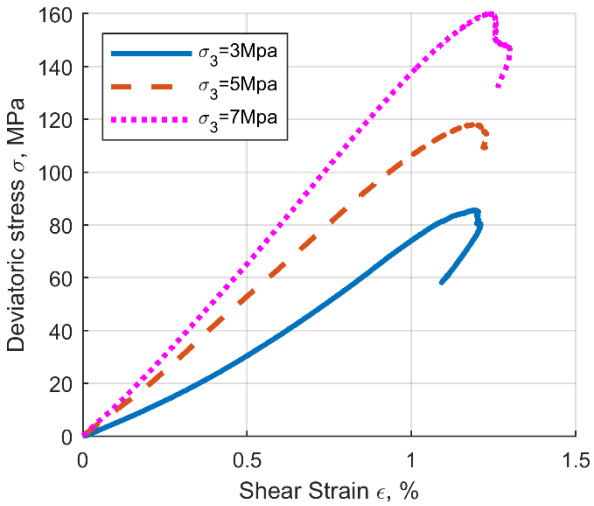

Figure 5.1 Short-term stress-strain curves (adapted from Cong and Hu, 2017)

Table 5.1 Loading steps in triaxial creep test (adapted from Cong and Hu, 2017)

Confining Pressure (MPa)	σ_c (MPa)	Triaxial creep loading stresses (MPa)					
		0.50 σ_c	0.55 σ_c	0.60 σ_c	0.65 σ_c	0.70 σ_c	0.75 σ_c
3	85.6	42.8	47.1	51.4	55.6	59.9	64.2
5	110	55.0	60.5	66.0	71.5	77.0	----
7	160	80.0	88.0	96.0	104.0	112.0	120.0

5.2.2. Triaxial creep test

Figure 5.2 shows the triaxial creep test result under the confining pressure of 3MPa. In Figure 5.2 (a), during each loading step, an apparent elastic strain is seen immediately emerged after deviatoric stress applied to the sandstone sample. These instantaneous material responses were processed according to *Boltzmann* superposition principle (Boltzmann, 1874; Henderson, 1951), and multi-step creep curves were consequently obtained as shown in Figure 5.2 (b). Figure 5.3 presents the processed axial strain against time curves while confining pressures are 5 and 7MPa, respectively. It is clearly shown that under high confining pressure, sample would be failed at higher values of deviatoric stress. Nonetheless, these obtained failure stresses (64.2, 77.0 and 120.0MPa), as presented in Figure 5.2 and 5.3, are seen about 25% less than the magnitude of sandstone's short-term strength (85.6, 110.0 and 160.0MPa), suggesting that creep deformation can cause considerable strength reduction to the testing sample. Further, the creep deformation pattern also show dependency on applied loading stresses. When deviatoric stresses is less than sample's short-term yield stress (62.0, 74.0 and 114.0MPa), only transient and steady-state creeps are presented (also referred as first and second stages of creep behavior in literatures). The complete three stages creep

behavior-consisting of transient, steady-state and accelerating deformation trend (Boukharov, Chanda and Boukharov, 1995; Heap *et al.*, 2009)-occurred only when deviatoric stress beyond sample's short-term yield stress as indicated in the last loading step in each plot. Note that this conclusion drawn herein is under the experimental time of months, not years or decades. In other words, we cannot preclude the case that steady-state creep could potentially progressed into accelerating phase if test could be conducted as long as latter scenarios, given the applied deviatoric stress is small (Ito and Sasajima, 1987; Boukharov, Chanda and Boukharov, 1995; Cong and Hu, 2017).

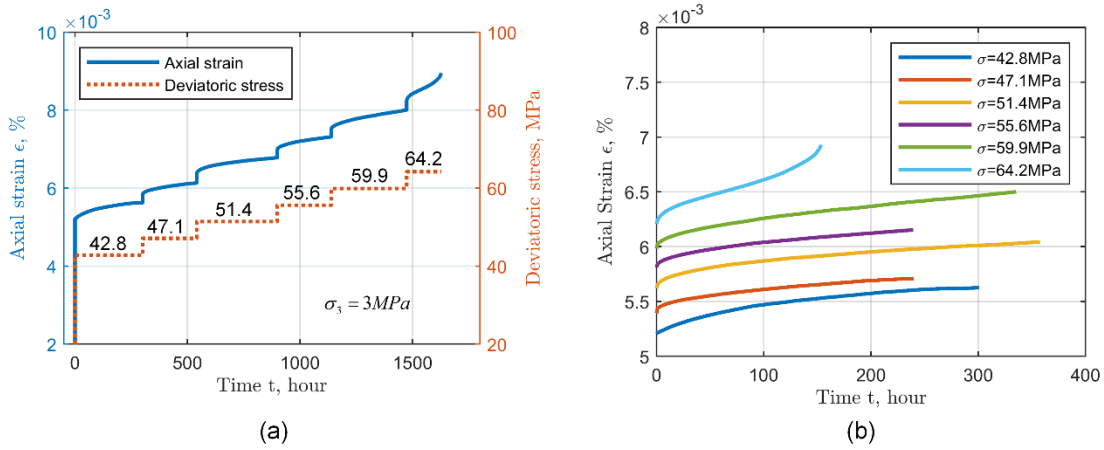

Figure 5.2 Tiaxial creep test result under confining pressure of 3MPa (a) axial strain vs. time and deviatoric stress vs. time response; (b) axial strain vs. time responses after applying *Boltzmann* superposition (adapted from Cong and Hu, 2017)

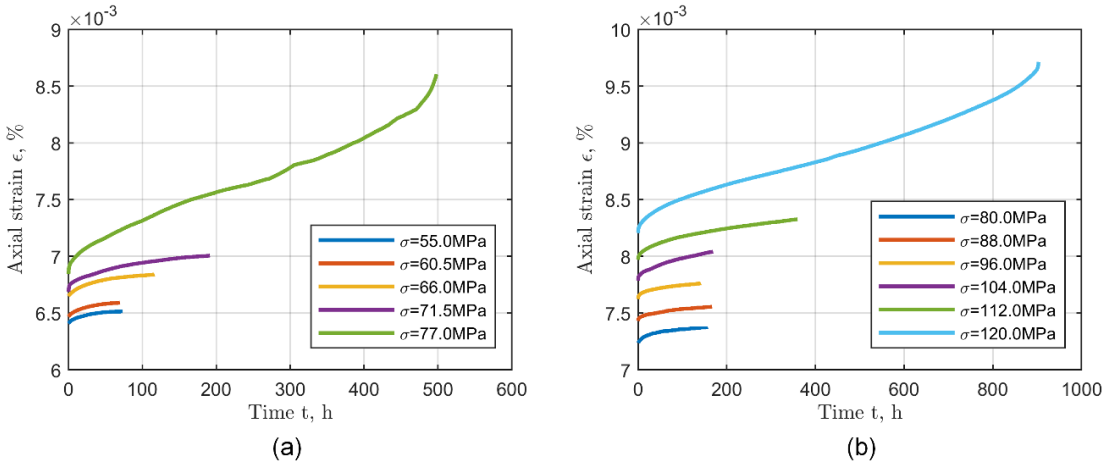

Figure 5.3 Creep tests results with confining pressures of (a) 5MPa and (b) 7MPa, respectively (adapted from Cong and Hu, 2017)

5.3. Visco-elastoplastic model representation

In this section, we introduce model development aiming to describe the non-linear rheological behavior of sandstone. Classic component models, such as Maxwell, Kelvin-Voigt, Van der Poel or Burger's model, have been thoroughly discussed in previous research and showed their ability to model visco-elastic behavior of rock (Boukharov, Chanda and Boukharov, 1995; Xu, Yang and Chu, 2006; Zhao, Liu and Dong, 2011; Jiang and Zhou, 2013). However, they are not designed for properly representing of visco-plastic behavior which is evident in accelerating creep phase. Thus, herein we propose a modified Van der Poel model by introducing a non-linear visco-plastic component to capture the accelerating deformation when sample approaches the creep failure.

The typical Van der Poel model is expressed as Equation 5.1, comprising the combination of Hooke spring and Kelvin-Voigt component:

$$\varepsilon = \frac{\sigma}{E_1} + \frac{\sigma}{E_2}(1 - e^{-E_2 \frac{t}{\eta_1}}) \tag{5.1}$$

Where ε is the total strain, E_1 is the elastic modulus responsible for instantaneous strain, E_2 and η_1 are elastic modulus and viscosity coefficient used to describe material visco-elastic deformation. Since the elastic modulus is reported exhibiting a positive linear relationship with the applied stress level (Cong and Hu, 2017), hence the model can be modified as:

$$\varepsilon = \frac{\sigma}{a\sigma + b} + \frac{\sigma}{E_2}(1 - e^{-E_2 \frac{t}{\eta_1}}) \tag{5.2}$$

Where a and b are constants during one creep test and should be calibrated through the relationship between E_1 and σ.

When loading stress exceeds the yield stress of sandstone ($\sigma > \sigma_s$), plastic strain would be involved in the deformation process. Therefore, a stress triggered visco-plastic string is invoked to complement the above model. The graphic representation of this component is shown in Figure 5.4, and the corresponding constitutive equation is:

$$\sigma - \sigma_s = \eta_2(t)\dot{\varepsilon} \tag{5.3}$$

Where $\eta_2 = \frac{A\eta_0}{At^2 - Bt + C}$, $C \neq 0$ and $B^2 - 4AC < 0$, η_0 is a positive initial viscosity coefficient. Solving the differential equation, Equation 5.3 is processed as:

$$\varepsilon = \frac{\sigma - \sigma_s}{\eta_0}(\frac{1}{3}t^3 - \frac{1}{2}\frac{B}{A}t^2 + \frac{C}{A}t) \tag{5.4}$$

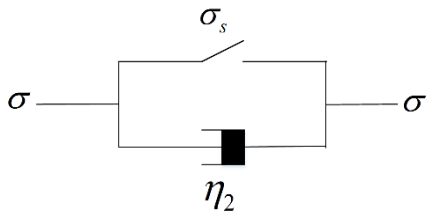

Figure 5.4 Non-linear visco-plastic model component

And it can be further simplified as:

$$\varepsilon = \frac{\sigma - \sigma_s}{\eta_0}\left(\frac{1}{3}t^3 - \frac{1}{2}\alpha_1 t^2 + \alpha_2 t\right) \tag{5.5}$$

Where $\alpha_1 = \frac{B}{A}$ and $\alpha_2 = \frac{C}{A}$. Therefore, the proposed visco-elastoplastic model is a summation of elastic, visco-elastic and visco-plastic model components, as depicted in Figure 5.5, and the functional expression is given in Equation 5.6.

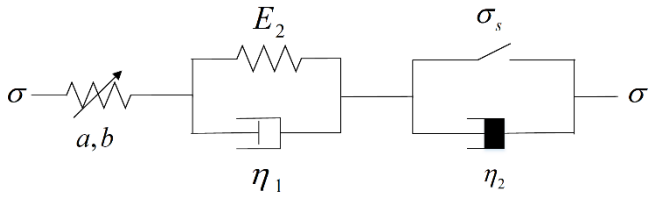

Figure 5.5 Visco-elastoplastic creep model

$$\begin{cases} \varepsilon = \dfrac{\sigma}{a\sigma + b} + \dfrac{\sigma}{E_2}\left(1 - e^{-E_2 \frac{t}{\eta_1}}\right) & \sigma < \sigma_s \\ \varepsilon = \dfrac{\sigma}{a\sigma + b} + \dfrac{\sigma}{E_2}\left(1 - e^{-E_2 \frac{t}{\eta_1}}\right) + \dfrac{\sigma - \sigma_s}{\eta_0}\left(\dfrac{1}{3}t^3 - \dfrac{1}{2}\alpha_1 t^2 + \alpha_2 t\right) & \sigma \geq \sigma_s \end{cases} \tag{5.6}$$

5.4. Probabilistic calibration of inverse problem

The characterization of model parameters can be generalized as the process of estimating causal factors or parameters that produced system responses (observations) (Tarantola, 2005). The conventional model predictions (forward problem), is a mathematical mapping from a vector of model parameters $\boldsymbol{\theta}$ to a set of obtained observations $\boldsymbol{d}_{obs}$, through a model definition $g(\cdot)$ reflecting one's theoretical belief towards the physical process of interest. The simulated model responses, would inevitably present with some deviations from the observed data, which can be denoted as:

$$\boldsymbol{d}_{obs} = g(\boldsymbol{\theta}) + \boldsymbol{\varepsilon} \tag{5.7}$$

Where $\boldsymbol{\varepsilon}$ represents the tradeoff term that quantify the difference between experimental observations and model predictions. It is noted that one should not confuse this quantity with errors between experimental observation and 'true process' ($\boldsymbol{d} - \boldsymbol{d}_{obs} = \Delta\boldsymbol{d}_{obs}$), or assuming it solely stems from modeling error ($\boldsymbol{d} - \boldsymbol{d}_{pred} = \Delta\boldsymbol{d}_{pred}$). Instead, it is the metric signifying how much the model error is deviate from observation error ($\boldsymbol{d}_{obs} - \boldsymbol{d}_{pred} = \Delta\boldsymbol{d}_{pred} - \Delta\boldsymbol{d}_{obs}$). Due to the true physical process is usually unknown, the independent characterization of $\Delta\boldsymbol{d}_{pred}$ and $\Delta\boldsymbol{d}_{obs}$ is practically difficult (Medina-Cetina, 2006). However, when probabilistic expectation $E(\Delta\boldsymbol{d}_{pred} - \Delta\boldsymbol{d}_{obs}) = 0$, as assumed in this paper, the bias error would be vanished in the definition of $\boldsymbol{\varepsilon}$, and the participating sources of uncertainty would merely rely on the state of evidence, $\boldsymbol{d}_{obs}$ and $\boldsymbol{d}_{pred}$, respectively.

The probabilistic calibration presented in this paper consisting in the inverse mapping (contrary to forward problem) of experimental creep observations $\boldsymbol{d}_{obs}$ onto the vector of rheological model parameters $\boldsymbol{\theta}$, while accounting the uncertainty across all participating sources both from $\boldsymbol{d}_{obs}$ and $g(\boldsymbol{\theta})$. The Bayesian paradigm provides a suitable framework to address this inversion by treating model parameters $\boldsymbol{\theta}$ as random variables and through a functional approach to integrate each participating evidence, such that:

$$\pi(\boldsymbol{\theta} \mid \boldsymbol{d}_{obs}) = \frac{f[\boldsymbol{d}_{obs} \mid g(\boldsymbol{\theta}), \boldsymbol{\theta}]\pi(\boldsymbol{\theta})}{\int f[\boldsymbol{d}_{obs} \mid g(\boldsymbol{\theta}), \boldsymbol{\theta}]\pi(\boldsymbol{\theta}) d\boldsymbol{\theta}} \tag{5.8}$$

Where the factor $\pi(\boldsymbol{\theta})$ is called prior distribution, summarizing the information is available on $\boldsymbol{\theta}$ prior to the coming of observations $\boldsymbol{d}_{obs}$; $f[\boldsymbol{d}_{obs} \mid g(\boldsymbol{\theta}), \boldsymbol{\theta}]$ is called likelihood, used to assess the probability of observed data $\boldsymbol{d}_{obs}$ produced by the model $g(\cdot)$ with parameters $\boldsymbol{\theta}$; $\pi(\boldsymbol{\theta} \mid \boldsymbol{d}_{obs})$ is called posterior, representing the inference of probability distribution of $\boldsymbol{\theta}$ conditioned on $\boldsymbol{d}_{obs}$.

The solving of above function is often facing difficulties in integration of denominator analytically ($f[d_{obs}] = \int f[\boldsymbol{d}_{obs} \mid g(\boldsymbol{\theta}), \boldsymbol{\theta}]\pi(\boldsymbol{\theta}) d\boldsymbol{\theta}$). Alternatively, one can turn to numerical approximation for the calculation of posterior. In this paper, we sample the posterior distribution by combining Markov-chain Monte-Carlo method (MCMC) with Metropolis-Hastings criteria, which essentially perform intelligent search in parametric space and Bayesian models in high dimensions become tractable (Robert and Casella, 2013). The total integration of posterior in present research took several

millions of parameter samples, in which the initial fluctuation part was discarded as burn-in session, and the rest was used to calculate the statistics providing both uncertainty and correlation quantifications as discussed in the following.

5.5. Application to visco-elastoplastic model

5.5.1. Experimental design and convergence diagnosis

Based on laboratory creep test results, we conducted totally 18 probabilistic calibrations with proposed constitutive model. As illustrated in Figure 5.6, when $\sigma < \sigma_s$, model is composed of elastic and visco-elastic components, which applied to 15 creep test results. The rest three testing groups, involving accelerating creep behavior, were modeled by constitutive relationship including additional visco-plastic component.

With regard to the element definition in Equation 8, we choose *non-information* prior for all model parameters, meaning that no initial knowledge imposed on governing parameters while the calibration outcomes solely depend on the tradeoff between experimental observation and model predictions. A univariate Gaussian distribution was selected for defining the likelihood function, as shown below:

$$f[\boldsymbol{d}_{obs} \mid g(\boldsymbol{\theta}), \boldsymbol{\theta}] \propto \frac{1}{\sigma^n} \exp\left\{-\frac{1}{2\sigma^2}\sum_{i=1}^{n}[\boldsymbol{d}_{obs} - g(\boldsymbol{\theta})]^2\right\} \tag{5.9}$$

Where σ equals to the residuals between observations and model predictions, computed during each iteration. Note that by choosing univariate Gaussian likelihood, we implicitly assume data points are independent with each other and uncertainty is homoscedastic along the domain of interest.

Due to different cases may require different computational efforts to achieve stationary status, we over-sampled parametric space (10 million iterations) to ensure all calibrations can be converged and all probability modes were explored. Figure 5.7 to 5.10 showcase the convergence diagnose based on one test result where $\sigma_3 = 3MPa$ and $\sigma = 42.8MPa$. Figure 5.7 present sample sequence of each parameter after 10 million iterations. The cumulative mean and standard deviation of sequences were calculated and as shown in Figure 5.8 and 5.9, in which a stationary state can be observed after 4 million iterations. Thus, the previously described burn-in point was set as 4 million and only samples afterwards were used for posterior evaluation.

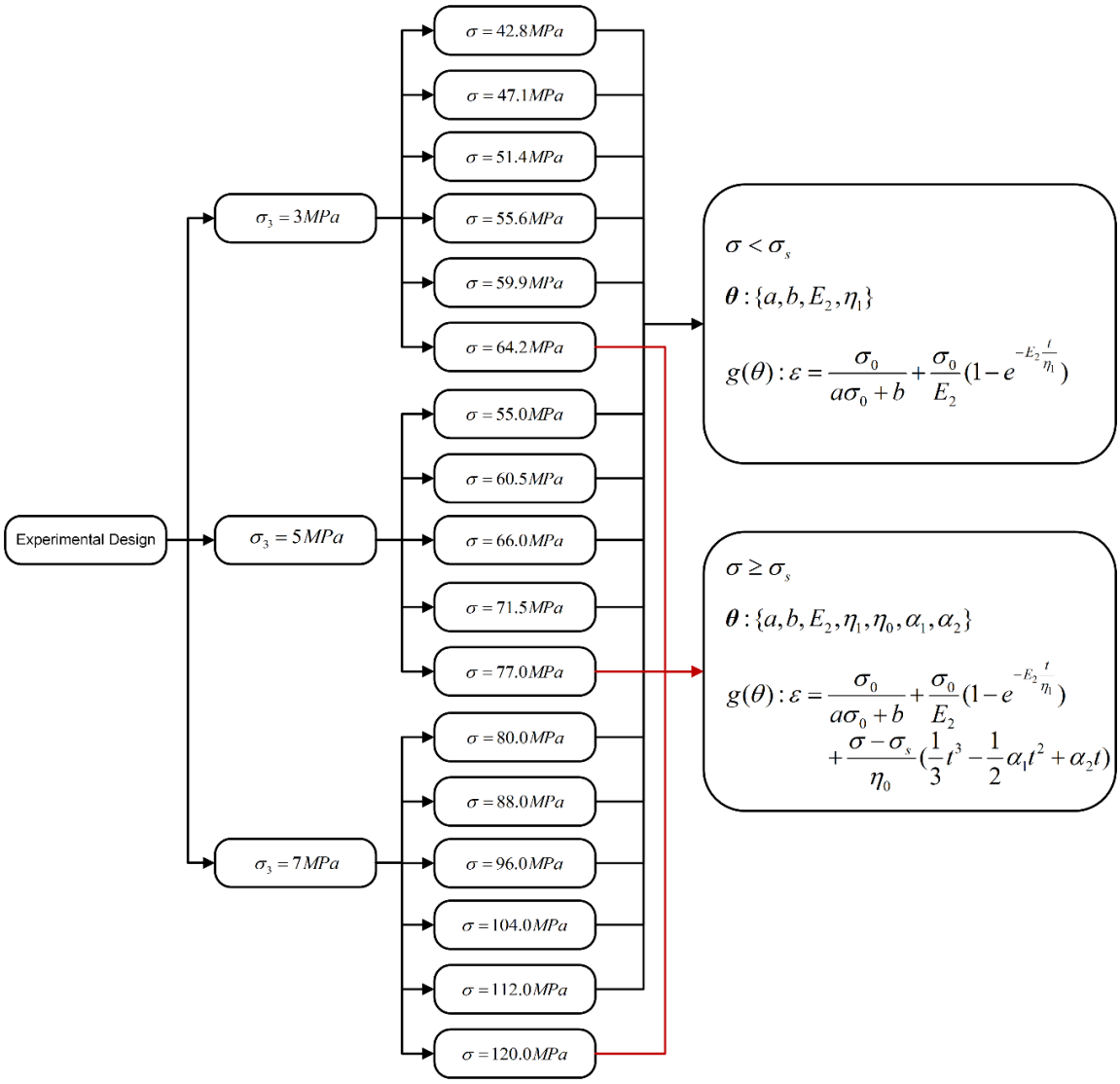

Figure 5.6 Experimental design of probabilistic calibration

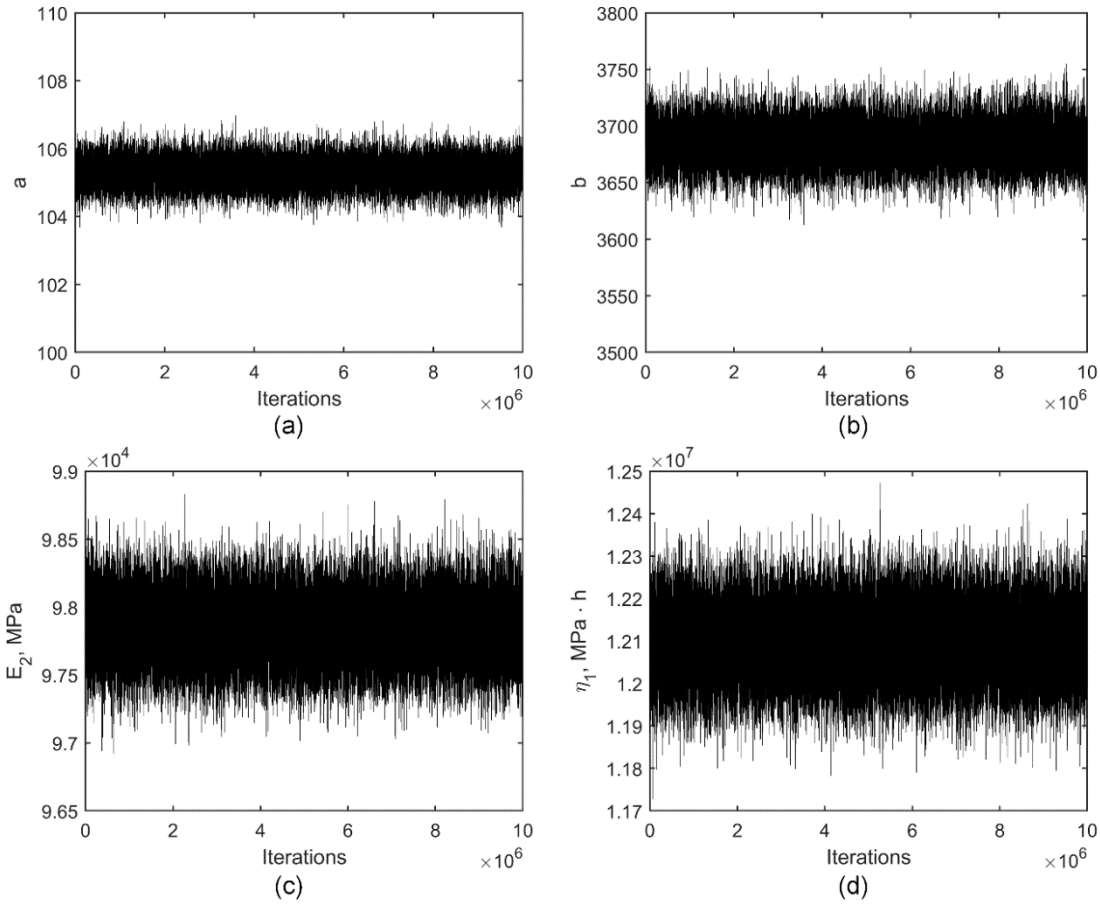

Figure 5.7 Sample sequences of model parameters (a) a, (b) b, (c) E_2, (d) η_1

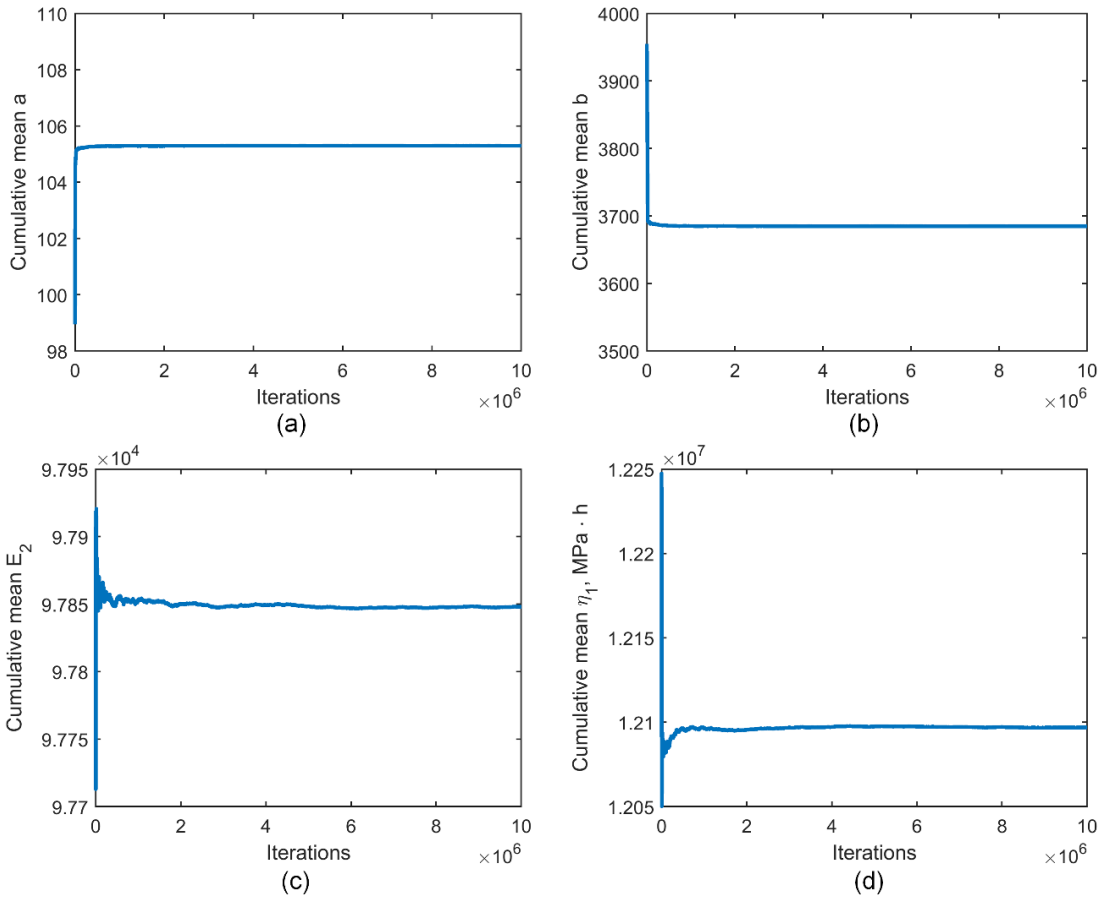

Figure 5.8 Cumulative mean of sample sequence for each parameter (a) a, (b) b, (c) E_2, (d) η_1

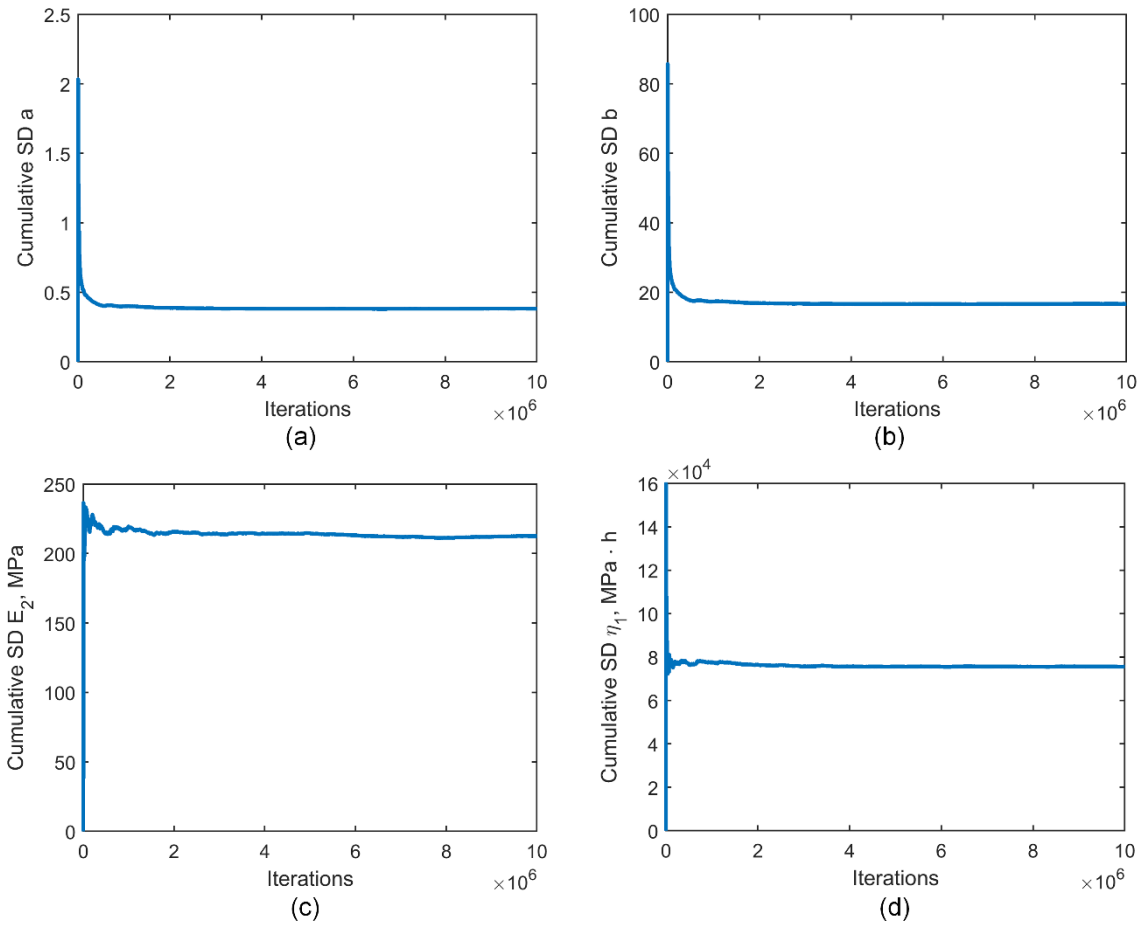

Figure 5.9 Cumulative standard deviation of sample sequence for each parameter (a) a, (b) b, (c) E_2, (d) η_1

5.5.2. Results

5.5.2.1. Marginal statistics of posterior ($\sigma < \sigma_s$)

The probabilistic calibration offers full probability distribution of model parameters in light of experimental observations and model predictions, thus it allows us to assess probability modes and uncertainty levels of each model parameter for each calculation case. In this section, we present the results related to the cases when $\sigma < \sigma_s$,

and model is defined as the combination of elastic and visco-elastic components. The calibration results related to accelerating creep behavior ($\sigma \geq \sigma_s$) will be discussed in a separate section since that model function is different because of the import of visco-plastic component. Figures 5.10 to 5.12 offer the probabilistically calibrated model parameters under varying confining pressures. In Figure 5.10, amidst five loading levels, parameters a and b are seen varying within narrow ranges in comparison with parameters E_2 and η_1. This is due to a and b are in fact derived from the relationship $E_1 = a\sigma + b$, and further suggests the variation range of E_1 is small. In PDF plots of E_2 and η_1 (Figure 5.10), the uncertainty levels are showing less in the first loading step ($\sigma = 42.8MPa$) than other loading phases. This behavior needs to be interpreted combined with time dependent behavior as previously presented in Figure 5.2, that the strain-time response is seen more flat for the first loading case, indicating viscosity is not obvious for sandstone subjected to such low loading pressure. As a consequence, it ease the difficulty of modeling visco-elastic response of sandstone and constitutive parameters are solved with higher confidence.

It is worth noting that visco-elastic component is also called as "delayed elasticity" in rock rheology literature (Ito and Sasajima, 1987; Boukharov, Chanda and Boukharov, 1995; Sterpi and Gioda, 2009). When $t \to \infty$, such component will equals to $\frac{\sigma}{E_2}$. Thus, E_2 is the modulus of delayed elasticity, and η_1 is so called "elastic viscosity". In Figures 5.10 to 5.12, it can be seen the varying ranges of E_2 are

approximate from 0.8 to 1.7 when $\sigma_3 = 3MPa$, 2.5 to 5 when $\sigma_3 = 5MPa$, and 3.4 to 9 when $\sigma_3 = 7MPa$, revealing a steady increase of E_2 with the rise of confining pressure. On the other hand, the trend of η_1 does not show an obvious pattern with the change of confinement conditions. However, under a constant confining pressure, η_1 seems gradually increase with the growth of axial loading stress, indicating the delayed effect is less significant when sandstone is subjected to a high loading pressure.

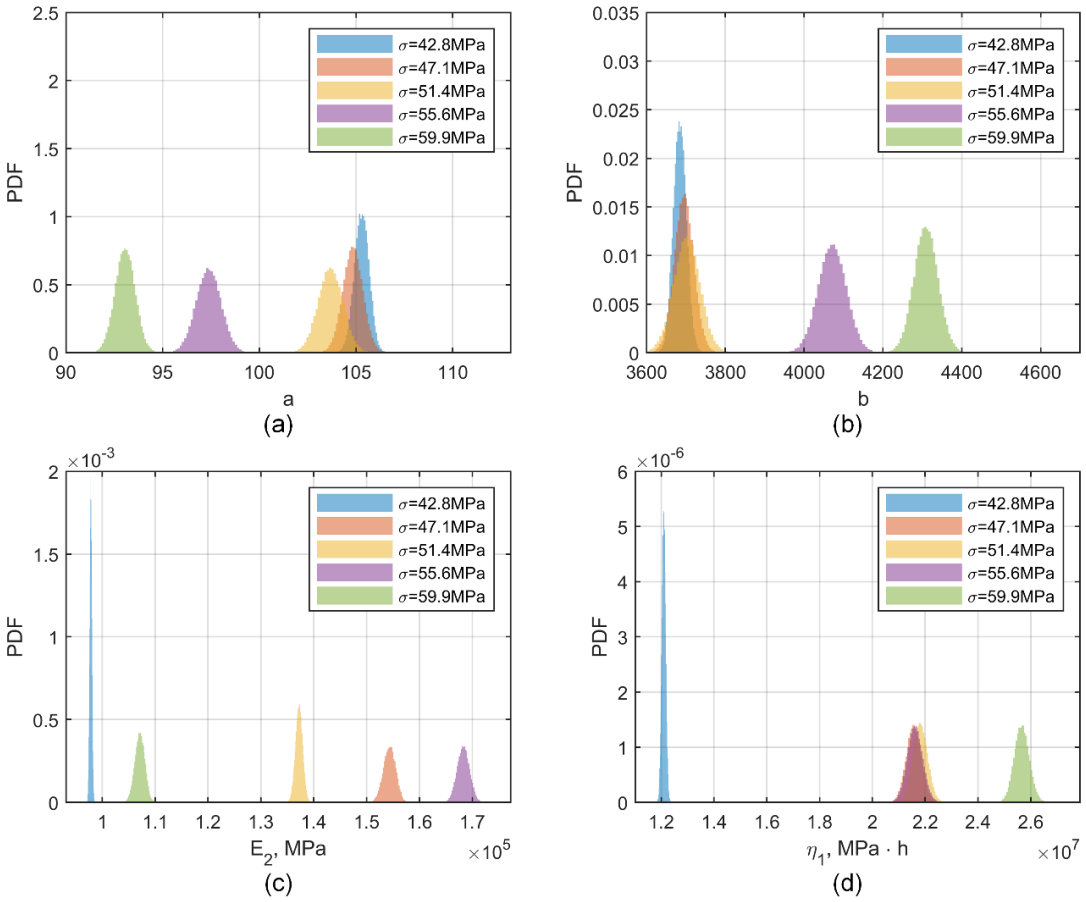

Figure 5.10 Posterior PDFs of constitutive model parameters ($\sigma_3 = 3MPa$)

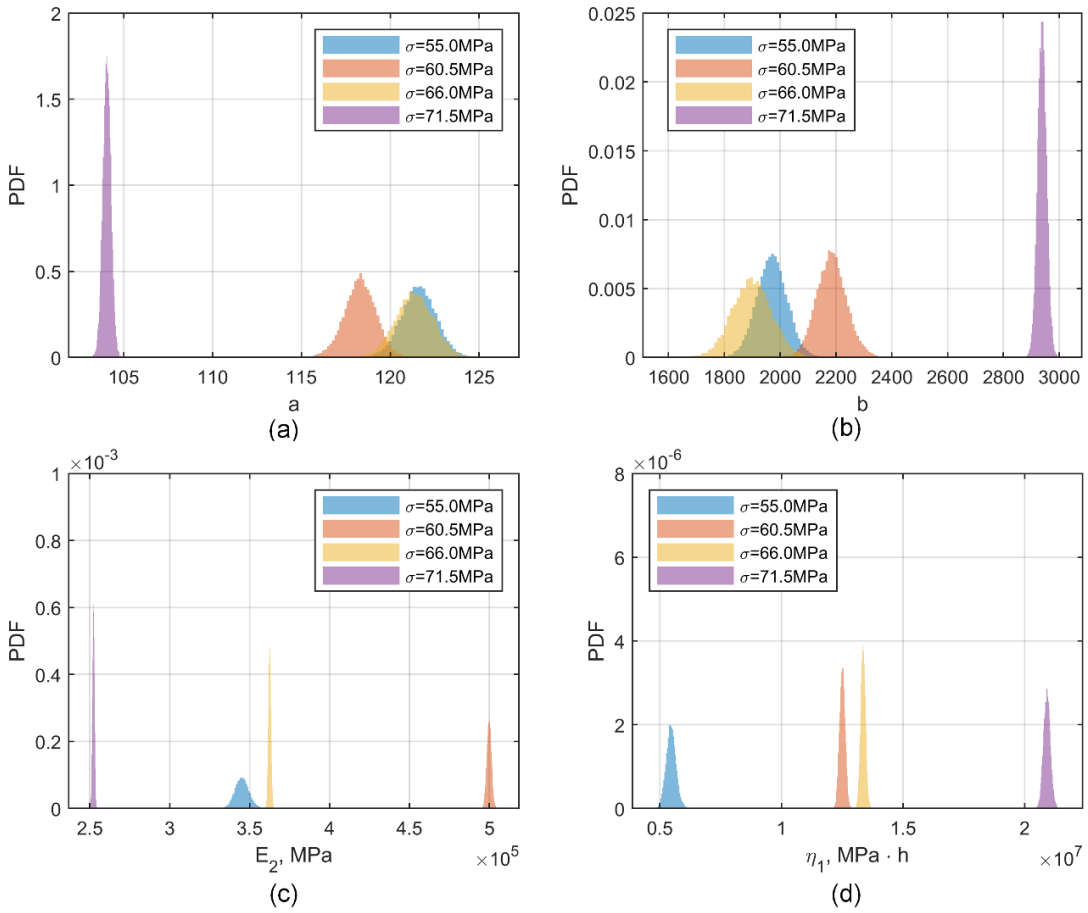

Figure 5.11 Posterior PDFs of constitutive model parameters ($\sigma_3 = 5MPa$)

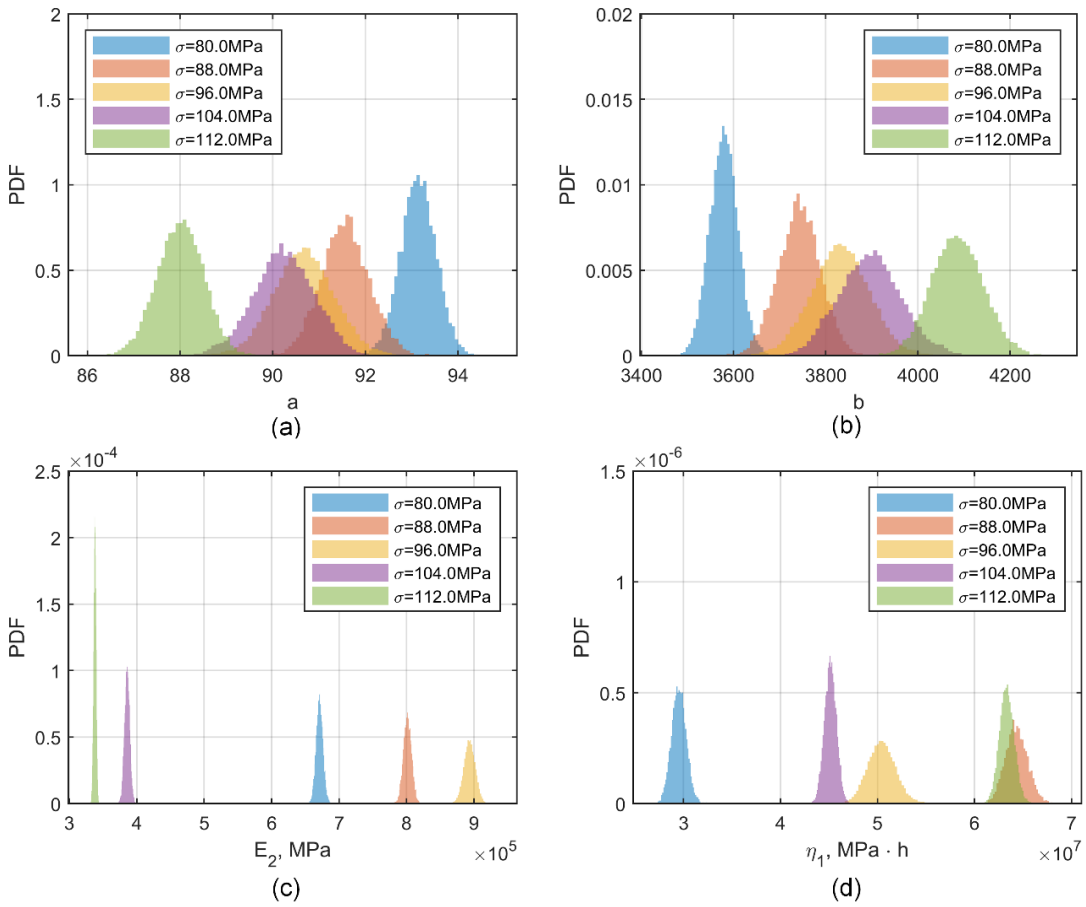

Figure 5.12 Posterior PDFs of constitutive model parameters ($\sigma_3 = 7MPa$)

5.5.2.2. Correlation statistics of posterior ($\sigma < \sigma_s$)

One of the benefits of probabilistic calibration is that it offers full probability description of parameters, thus correlations of model parameters are explicit in the posterior distribution. For instance, in the case where $\sigma_3 = 3MPa$ and $\sigma = 42.8MPa$, after simulation attained stationary status, samples in terms of E_2 and η_1 extracted from posterior distribution are presented with negative correlation as illustrated in Figure 5.13, indicating elastic modulus E_2 and elastic viscosity η_1 are negatively associated in

simulating visco-elastic response. Tables 5.2 to 5.4 present correlation matrices of model parameters obtained from probabilistic calibrations across all experimental data scenarios, which show that the distinct correlation exists when two parameters are come from same model component (i.e., a and b, E_2 and η_1). This can be explained through the basic assumption of component model, which assumes each model component can work independently, thus correlation should be obvious only when parameters are defined in the same model component. It is also noticed that such description may not strictly account for all calibration results. For instance, in Table 5.2, when confining pressure is 3MPa, we see moderate cross-correlation between parameters b_2 and η_1. However, such association is not showing with a clear, characteristic pattern, in contrast to those of a and b, E_2 and η_1.

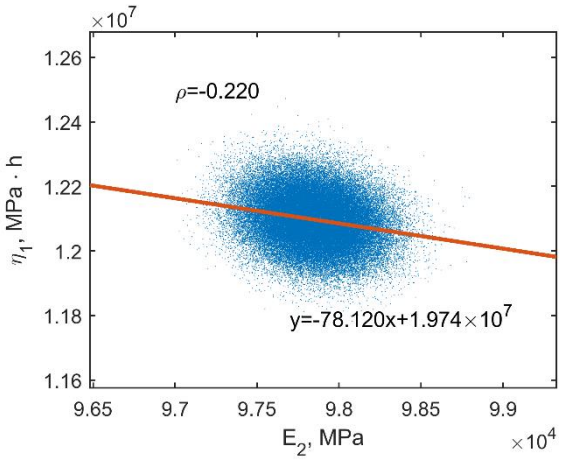

Figure 5.13 Parameter samples of E_2 and η_1 from the posterior distribution

Table 5.2 Correlation matrix of model parameters calibrated when $\sigma_3 = 3MPa$

Parameters	Loading stress (MPa)	Parameters			
		a	b	E_2	η_1
a	42.8	1.000	-0.997	0.038	0.192
	47.1	1.000	-0.998	-0.075	0.194
	51.4	1.000	-0.998	0.001	0.098
	55.6	1.000	-0.999	0.033	-0.093
	59.9	1.000	-0.998	0.108	-0.224
b	42.8		1.000	-0.051	-0.255
	47.1		1.000	0.093	-0.245
	51.4		1.000	-0.001	-0.151
	55.6		1.000	-0.021	0.05
	59.9		1.000	-0.078	0.167
E_2	42.8			1.000	-0.22
	47.1			1.000	-0.673
	51.4			1.000	-0.415
	55.6			1.000	-0.633
	59.9			1.000	-0.799
η_1	42.8				1.000
	47.1				1.000
	51.4				1.000
	55.6				1.000
	59.9				1.000

Table 5.3 Correlation matrix of model parameters calibrated when $\sigma_3 = 5MPa$

Parameters	Loading stress (MPa)	Parameters			
		a	b	E_2	η_1
a	55.0	1.000	-0.997	0.17	0.164
	60.5	1.000	-0.998	0.032	0.056
	66.0	1.000	-0.997	0.015	0.033
	71.5	1.000	-0.999	-0.008	-0.2
b	55.0		1.000	-0.218	-0.211
	60.5		1.000	-0.036	-0.064
	66.0		1.000	-0.021	-0.042
	71.5		1.000	0.003	0.157
E_2	55.0			1.000	0.683
	60.5			1.000	0.043
	66.0			1.000	0.263
	71.5			1.000	-0.319
η_1	55.0				1.000

Table 5.3 Continued

Parameters	Loading stress (MPa)	Parameters			
		a	b	E_2	η_1
η_1	60.5				1.000
	66.0				1.000
	71.5				1.000

Table 5.4 Correlation matrix of model parameters calibrated when $\sigma_3 = 7MPa$

Parameters	Loading stress (MPa)	Parameters			
		a	b	E_2	η_1
a	80.0	1.000	-0.999	0.100	0.092
	88.0	1.000	-0.998	-0.035	0.091
	96.0	1.000	-0.999	0.005	0.038
	104.0	1.000	-0.997	0.032	-0.055
	112.0	1.000	-0.998	0.034	-0.113
b	80.0		1.000	-0.137	-0.138
	88.0		1.000	0.036	-0.107
	96.0		1.000	-0.01	-0.058
	104.0		1.000	-0.024	0.037
	112.0		1.000	-0.028	0.085
E_2	80.0			1.000	0.414
	88.0			1.000	-0.452
	96.0			1.000	-0.202
	104.0			1.000	-0.772
	112.0			1.000	-0.581
η_1	80.0				1.000
	88.0				1.000
	96.0				1.000
	104.0				1.000
	112.0				1.000

5.5.2.3. Assessment of model predictions ($\sigma < \sigma_s$)

Because model parameters are updated probabilistically through present approach, it allows us to run random sampling towards posterior distribution and calculate statistics of model predictions. 10,000 combinations of model parameters were

randomly selected from posterior distribution and substituted into constitutive model expression, which consequently yielded 10,000 model realizations. Figure 14 shows all model realizations and standard deviation of these model realizations against experimental time *t*, under confining pressures are 3, 5, and 7MPa, respectively. The comparison with observations indicates that the proposed model captures sandstone's creep deformation with good accuracy and precision, whereas errors can be observed arising mainly at the initial part. Sub-plots (b), (d), and (f) show variability of model predictions in which a persistent "w" shape SD pattern with respect to time is seen across all calibration cases, suggesting the proposed model has a systematic uncertainty in simulating the initial elastic and the end viscosity behaviors during each loading step. Meanwhile, the general uncertainty of model prediction tends to increase with the rise of the loading stress as shown in each sub-plot. A higher order polynomial term, for instance, could possibly improve the model performance by producing more flexible fits and stable estimates. However, the order of magnitude of variability can be observed very small (10^{-6}), which may imply such advancing effort is trivial.

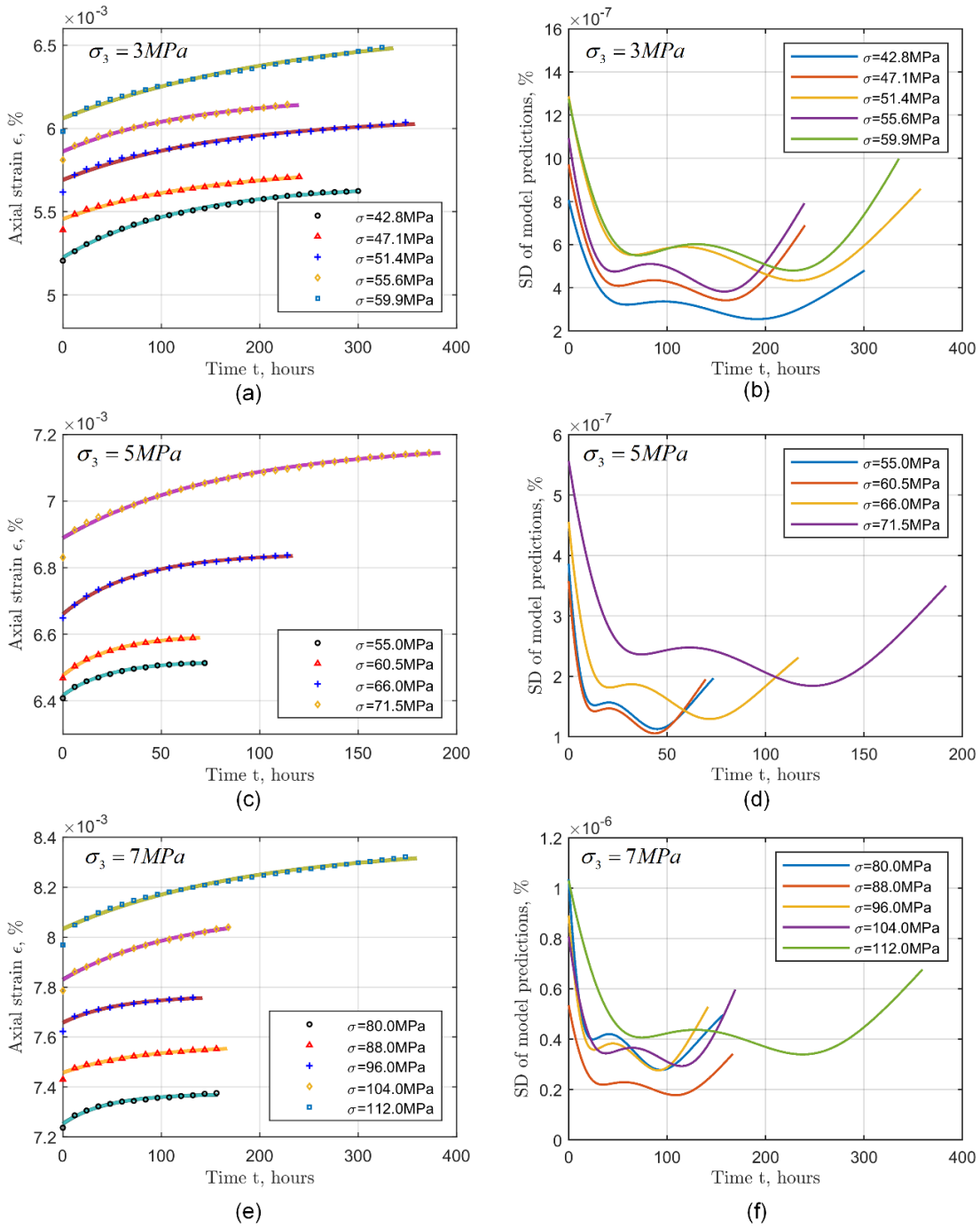

Figure 5.14 10,000 model realizations and standard deviation of model realizations, (a) and (b), (c) and (d), (e) and (f) are results related to σ_3 = 3, 5, and 7MPa, respectively (modeling results are denoted by solid lines, and experimental data are expressed by markers).

To further evaluate the model performance, we conducted residual analysis towards all calculation cases. Figure 5.15 presents full variabilities of residuals between model predictions and experimental observations, and empirical CDF of residuals obtained from all calibration results. Similarly, it is shown that the significant residuals occurred at the initial stage of loading, with the model tends to over-predict the sample's creep deformation. The CDF plots in Figure 5.15 also corroborate this observation, despite the cumulative probability median is around zero, a long tail is seen on positive residual side happened to all loading phases. It also follows the tendency that variability would increase with the progress of loading stress, suggesting that the proposed model agree better with experimental observations when loading stress is low.

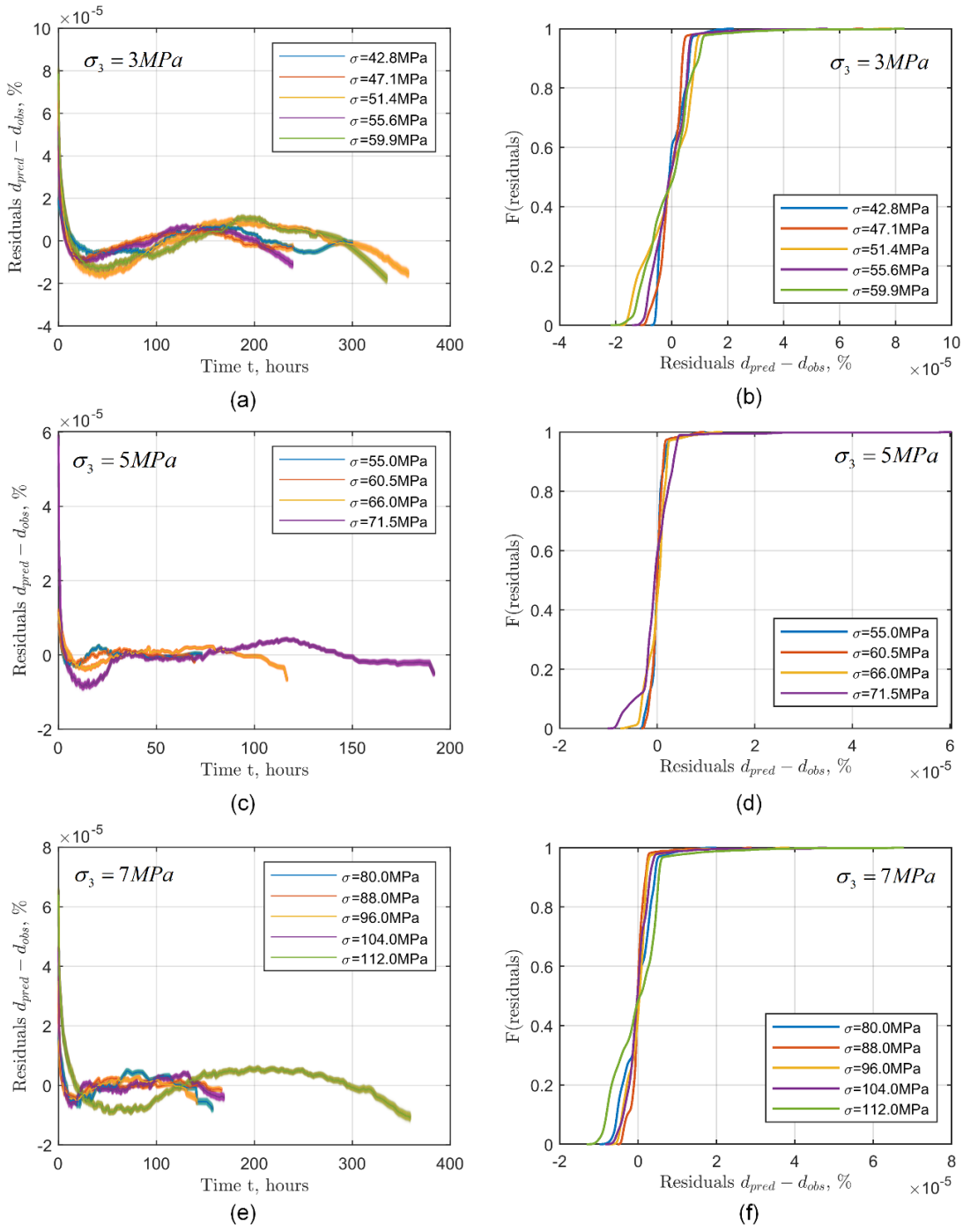

Figure 5.15 Residual analysis, (a), (c), and (e) are full variabilities of residuals between model predictions and experimental observations, (b), (d), and (f) are empirical CDF of residuals, under the confining pressures are 3, 5, and 7MPa

5.5.2.4. Probabilistic calibration of full visco-elastoplastic model ($\sigma > \sigma_s$)

Results of probabilistic calibration of visco-elastic model, relating to cases where loading stresses are less than yield stress, were described in preceding sections. Herein, we introduce calibration results regarding visco-plastic string has been triggered in the definition of constitutive model, meaning that acceleration creep is of consideration and aimed to be captured. Figures 5.16 to 5.18 present posterior distributions of model parameters after probabilistic calibration. The plots along diagonal direction are independent PDFs of model parameters, while the off-diagonal terms are representing joint relative frequency histograms (JRFHs) of each two parameters. It is worth noting that JRFH is not only showing joint mode of the pair of parameters, the shape of intensity map is also indicative of correlation relationship. For instance, a strong negative association between parameters a and b can be seen denoted by negative inclination angle of their joint probability mode in the parametric space. Apart from this distinct relationship between a and b, significant correlation are also found among other parameters, for instance, a positive correlation between η_0 and α_1, and a negative correlation between η_0 and α_2 are seen in Figure 5.16, meaning that these parameters are essentially correlated within visco-plastic string. It is further found that correlation patterns presented in JRFHs appear consistent from Figure 5.16 to 5.18, indicating model parameters are following the same association mechanism to simulate the constitutive properties even under different confining pressures.

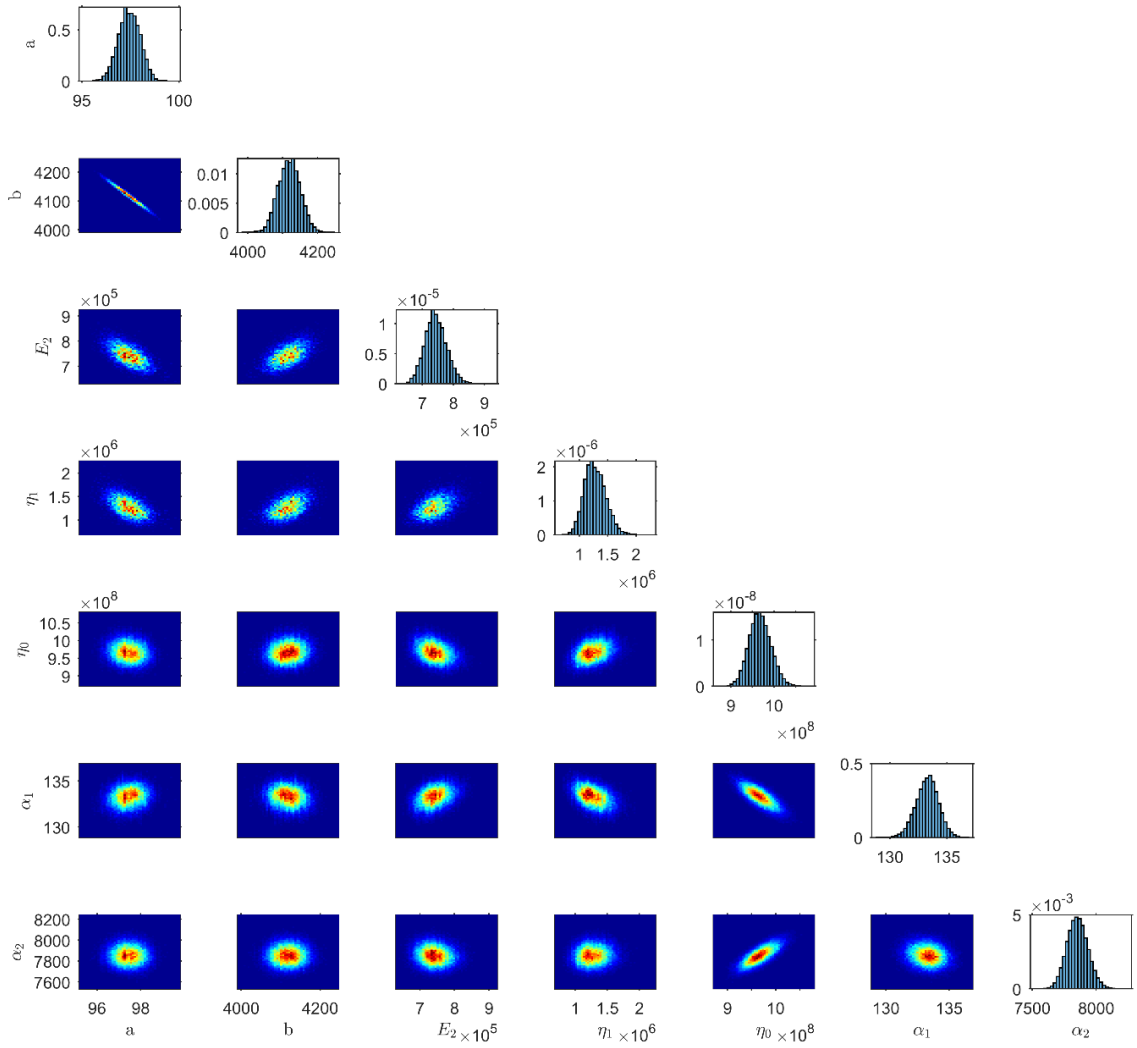

Figure 5.16 Posterior distributions of parameters when $\sigma_3 = 3MPa$ and $\sigma = 64.2MPa$

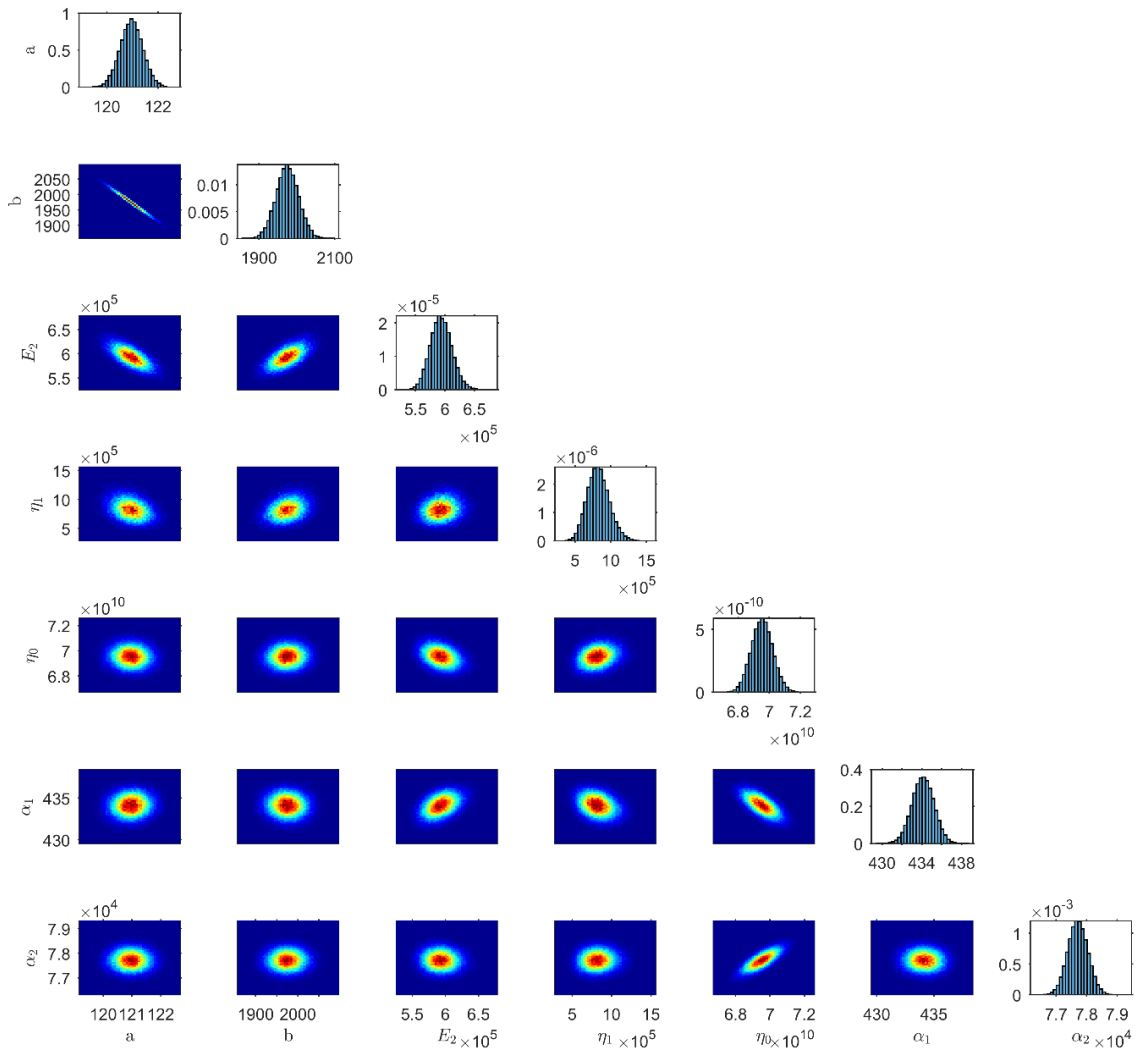

Figure 5.17 Posterior distributions of parameters when $\sigma_3 = 5MPa$ and $\sigma = 77.0MPa$

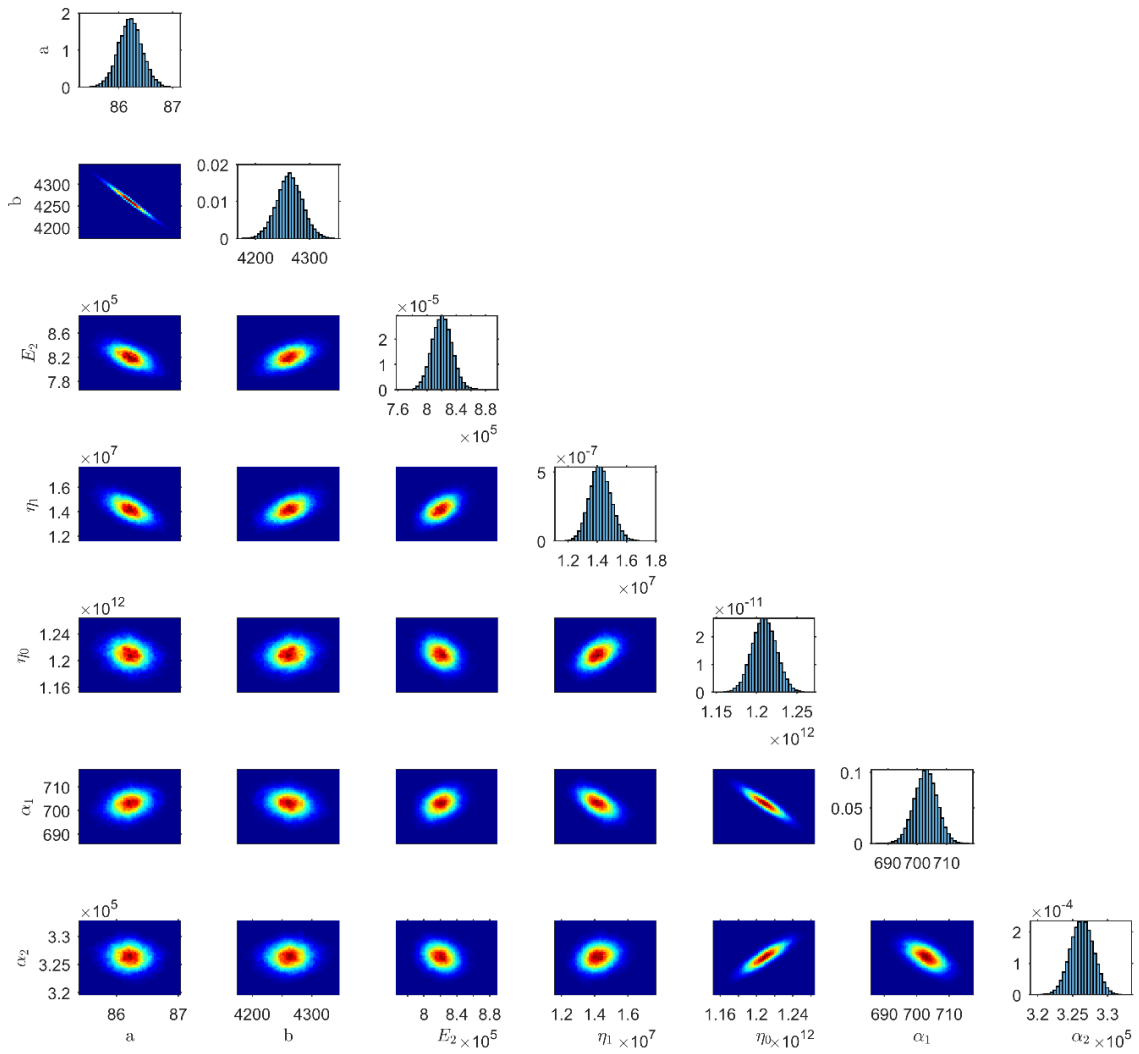

Figure 5.18 Posterior distributions of parameters when $\sigma_3 = 7MPa$ and $\sigma = 120.0MPa$

Similar to previous section, once posterior distribution was obtained, it allows us to randomly sample combinations of parameters and therefore evaluate model performance. Figure 5.19 (a) shows 10,000 model realizations compared to experimental observations of last loading stages when confining pressures are 3, 5, and 7MPa,

respectively. The total variation of model predictions is seen very small and unbiased to experimental observations, validated the full model is capable of simulating visco-elastoplastic behavior of sandstone with satisfying accuracy and precision. Figure 5.19 (b) presents the corresponding standard deviations versus experimental time. Again, the higher uncertainty takes place close to the initial and end moments of the tests, whereas the middle portion is observed more stable than previous cases (as in Figure 5.14), indicating model has gained the flexibility to capture the creep deformation due to the introduce of non-linear visco-plastic component.

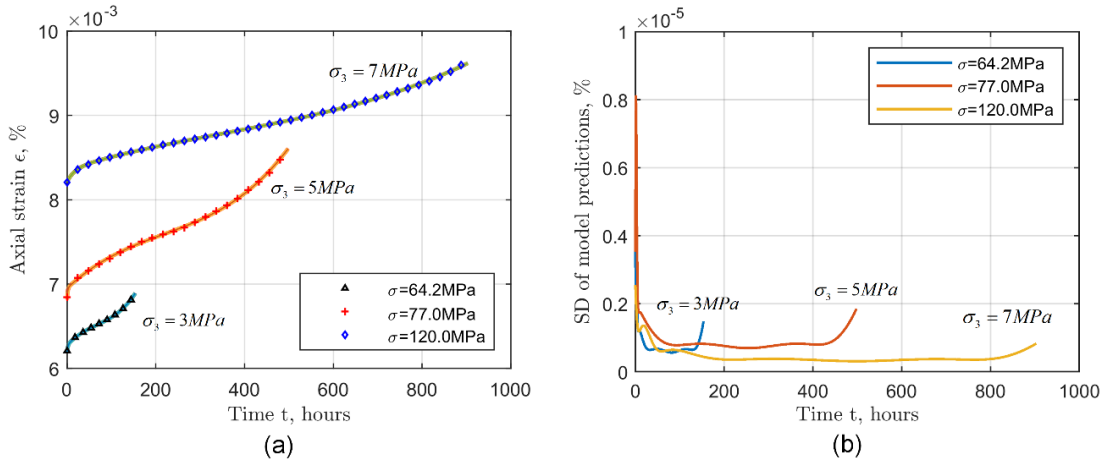

Figure 5.19 (a) 10,000 model realizations and experimental observations when σ_3 = 3, 5, and 7MPa, respectively (modeling results are denoted by solid lines, and experimental data are expressed by markers); (b) standard deviations of model realizations

One important feature of probabilistic calibration lies in its fundamental concept that a belief, or probability of a hypothesis, can be updated in light of newly emerged evidence or information. Hence, the knowledge yielded from the calibration of the

tradeoff between the present laboratory results and the proposed model can be translated as a-prior information in future model assessment on similar scenarios, by following a probability intersecting formulation (Esmailzadeh *et al.*, 2011). Such effort is anticipated to aid the substantial reduction of uncertainty level in model inferences. Considering that the significant resources and time cost of carrying out such time-dependent experiments in regards to one of the most critical hydroelectric reservoirs on the earth, the advantage of systematically updating of existing knowledge can shed much lights on improved decision-making and optimize the use of resources in practical activities.

5.6. Conclusion

A Bayesian probabilistic calibration was conducted to assess the uncertainty of a proposed visco-elastoplastic model when presented to experimental observations comprised of a series of creep tests performed on sandstone specimen sampled from Three Gorges Reservoir. Results validated the proposed model can represent the rheological behavior of sandstone with great accuracy and precision. Main conclusions are drawn as follows:

(a) The calibrated parameter marginal distributions show that in visco-elastic model component, the modulus of delayed elasticity will increase with the rise of confining pressure, and delayed effect is less significant when sandstone is subjected to a high loading pressure.

(b) The correlation analysis show the strong association between parameters defined in the same model component, whereas cross-correlation among different model components is insignificant.

(c) The proposed model tend to over-predict the sample's creep deformation at the initial stage of loading. However, the errors analysis demonstrates the order of magnitude is very small.

(d) When the acceleration creep is of consideration and visco-plastic string is triggered in simulation, the model presents with higher flexibility to capture the non-linear creep deformation. The variation of model predictions is regarded as trivial and the uncertainty mainly takes place close to the initial and end moments of the tests.

5.7. References

Boltzmann, L. (1874) 'SB Akad. Wiss. Wien', *Ber*, 70, p. 275.

Boukharov, G. N., Chanda, M. W. and Boukharov, N. G. (1995) 'The three processes of brittle crystalline rock creep', in *International journal of rock mechanics and mining sciences & geomechanics abstracts*, pp. 325–335.

Brantut, N. *et al.* (2013) 'Time-dependent cracking and brittle creep in crustal rocks: A review', *Journal of Structural Geology*. Elsevier, 52, pp. 17–43.

Cong, L. and Hu, X. (2017) 'Triaxial rheological property of sandstone under low confining pressure', *Engineering Geology*. Elsevier, 231, pp. 45–55.

Damjanac, B. and Fairhurst, C. (2010) 'Evidence for a long-term strength threshold in crystalline rock', *Rock Mechanics and Rock Engineering*. Springer, 43(5), pp. 513–531.

Deng, H. F. *et al.* (2016) 'Creep degradation mechanism by water-rock interaction in the red-layer soft rock', *Arabian Journal of Geosciences*. Springer, 9(12), p. 601.

Deng, Q. L. *et al.* (2000) ‘Mass rock creep and landsliding on the Huangtupo slope in the reservoir area of the Three Gorges Project , Yangtze River , China’, *Engineering Geology*, 58, pp. 67–83.

Esmailzadeh, S. *et al.* (2011) ‘Joint states of information from different probabilistic calibrations of undrained shear strength of submarine clays’, in *Reston, VA: ASCEProceedings of the Geo-Frontiers 2011 conference, March 13-16, 2011, Dallas, Texas| d 20110000*.

Esmailzadeh, S. *et al.* (2015) ‘Varying dimensional Bayesian acoustic waveform inversion for 1D semi-infinite heterogeneous media’, *Probabilistic Engineering Mechanics*. Elsevier, 39, pp. 56–68.

Gelman, A. *et al.* (2013) *Bayesian data analysis*. London: Chapman and Hall/CRC.

Hastings, W. K. (1970) ‘Monte Carlo sampling methods using Markov chains and their applications’, *Biometrika*. Oxford University Press, 57, pp. 97–109.

Heap, M. J. *et al.* (2009) ‘Time-dependent brittle creep in Darley Dale sandstone’, *Journal of Geophysical Research: Solid Earth*. Wiley Online Library, 114(B7).

Henderson, C. (1951) ‘The application of Boltzmann’s superposition theory to materials exhibiting reversible β flow’, *Proceedings of the Royal Society of London. Series A. Mathematical and Physical Sciences*. The Royal Society London, 206(1084), pp. 72–86.

Highland, L. M. (2008) *Geographical Overview of the Three Gorges Dam and Reservoir, China-Geologic Hazards and Environmental Impacts*.

Hu, X. *et al.* (2015) 'Deformation characteristics and failure mode of the Zhujiadian landslide in the Three Gorges Reservoir, China', *Bulletin of Engineering Geology and the Environment*. Springer, 74(1), pp. 1–12.

Ito, H. and Sasajima, S. (1987) 'A ten year creep experiment on small rock specimens', in *International Journal of Rock Mechanics and Mining Sciences & Geomechanics Abstracts*, pp. 113–121.

Jian, W., Wang, Z. and Yin, K. (2009) 'Mechanism of the Anlesi landslide in the Three Gorges Reservoir, China', *Engineering Geology*. Elsevier, 108(1–2), pp. 86–95.

Jiang, Q. and Zhou, C. (2013) 'An extended Nishihara model for the description of three stages of sandstone creep', *Geophysical Journal International*, 193(2), pp. 841–854. doi: 10.1093/gji/ggt028.

Li, D., Yin, K. and Leo, C. (2010) 'Analysis of Baishuihe landslide influenced by the effects of reservoir water and rainfall', *Environmental Earth Sciences*. Springer, 60(4), pp. 677–687.

Medina-Cetina, Z. (2006) *Probabilistic calibration of a soil model*. PhD Dissertation. The John Hopkins University, Baltimore, MD.

Medina-Cetina, Z. *et al.* (2013) 'Bayesian inversion of heterogeneous media: Introducing the next generation of integrated studies for offshore site investigations', in *Offshore Technology Conference*. Houston, Texas, May 6-9.

Medina-Cetina, Z. and Arson, C. (2014) 'Probabilistic Calibration of a damage rock mechanics model', *Geotechnique Letters*, 4(1), pp. 17–21.

Metropolis, N. *et al.* (1953) 'Equation of state calculations by fast computing machines', *The Journal of Chemical Physics*. AIP, 21(6), pp. 1087–1092.

Ranalli, M. *et al.* (2014) 'Probabilistic Calibration of a Dynamic Model for Predicting Rainfall-Controlled Landslides', *Journal of Geotechnical and Geoenvironmental Engineering*, 140(4), p. 04013039. doi: 10.1061/(ASCE)GT.1943-5606.0000972.

Robert, C. and Casella, G. (2013) *Monte Carlo Statistical Methods*. Springer Science & Business Media.

Sterpi, D. and Gioda, G. (2009) 'Visco-plastic behaviour around advancing tunnels in squeezing rock', *Rock Mechanics and Rock Engineering*. Springer, 42(2), pp. 319–339.

Tarantola, A. (2005) *Inverse problem theory and methods for model parameter estimation*. SIAM.

Tsai, L. S. *et al.* (2008) 'Time-dependent deformation behaviors of weak sandstones', *International Journal of Rock Mechanics and Mining Sciences*. Elsevier, 45(2), pp. 144–154.

Wang, F.-W. *et al.* (2004) 'The July 14, 2003 Qianjiangping landslide, three gorges reservoir, China', *Landslides*. Springer, 1(2), pp. 157–162.

Wang, F. *et al.* (2008) 'Movement of the Shuping landslide in the first four years after the initial impoundment of the Three Gorges Dam Reservoir, China', *Landslides*. Springer, 5(3), pp. 321–329.

Weng, M. C. *et al.* (2010) 'Numerical modeling of tunnel excavation in weak sandstone using a time-dependent anisotropic degradation model', *Tunnelling and Underground Space Technology*. Elsevier, 25(4), pp. 397–406.

Xu, W., Yang, S. and Chu, W. (2006) 'Nonlinear viscoelasto-plastic rheological model (Hohai model) of rock and its engineering application', *Chinese Journal of Rock Mechanics and Engineering*, 25(3), pp. 433–447.

Zhao, B., Liu, D. and Dong, Q. (2011) 'Experimental research on creep behaviors of sandstone under uniaxial compressive and tensile stresses', *Journal of Rock Mechanics and Geotechnical Engineering*. Elsevier, 3, pp. 438–444.

Zheng, H., Feng, X.-T. and Hao, X. (2015) 'A creep model for weakly consolidated porous sandstone including volumetric creep', *International Journal of Rock Mechanics and Mining Sciences*, 100(78), pp. 99–107.

Zheng, H., Feng, X. and Hao, X. (2015) 'A creep model for weakly consolidated porous sandstone including volumetric creep', *International Journal of Rock Mechanics and Mining Sciences*. Elsevier, 78, pp. 99–107. doi: 10.1016/j.ijrmms.2015.04.021.

Zhu, Y. *et al.* (2017) 'Probabilistic Calibration of a Modified Van der Poel Model Representing the Viscoelastic Behavior of Sandstone', *Geotechnical Special Publication GSP*, 285, pp. 113–123. doi: 10.1061/9780784480724.007.

APPENDIX A

GRADIENT, DIVERGENCE AND CURL IN CYLINDRICAL COORDINATES

A.1. The *del* operator ∇

The gradient, the divergence, and the curl are first-order kinematic operators acting on fields. The conventional way to express them is via a vector called *del* or *nabla*, whose components are partial derivatives with respect to certain coordinates system. For instance, in Cartesian coordinates, the *del* operator ∇ is defined as:

$$\nabla = \hat{i}\frac{\partial}{\partial x} + \hat{j}\frac{\partial}{\partial y} + \hat{k}\frac{\partial}{\partial z} \tag{A.1}$$

Given the *del* operator is a vector, we can conduct some vector operations such as dot product and cross product which leads to the concept of divergence and curl in Cartesian coordinates as shown in Equations A.2 and A.3:

$$\nabla \cdot U = \frac{\partial U_x}{\partial x} + \frac{\partial U_y}{\partial y} + \frac{\partial U_z}{\partial z} \tag{A.2}$$

$$\nabla \times U = \hat{i}\left(\frac{\partial U_z}{\partial y} - \frac{\partial U_y}{\partial z}\right) + \hat{j}\left(\frac{\partial U_x}{\partial z} - \frac{\partial U_z}{\partial x}\right) + \hat{k}\left(\frac{\partial U_y}{\partial x} - \frac{\partial U_x}{\partial y}\right) \tag{A.3}$$

A.2. Coordinate Transformation

The transformations between Cylindrical and Cartesian coordinates are:

$$Cartesian \rightarrow Cylindrical : \begin{Bmatrix} \rho = \sqrt{x^2 + y^2} \\ \phi = \arctan(y, x) \\ z = z \end{Bmatrix} \tag{A.4}$$

$$Cylindrical \rightarrow Cartesian: \begin{Bmatrix} x = \rho\cos\phi \\ y = \rho\sin\phi \\ z = z \end{Bmatrix} \tag{A.5}$$

The unit vector in the Cylindrical coordinates are the functions of position. They are point to radius, tangential, and vertical directions, respectively. The forward and inverse transformations of unit vectors between Cartesian and Cylindrical coordinates are:

$$Cartesian \rightarrow Cylindrical: \begin{Bmatrix} \hat{\rho} = \hat{i}\cos\phi + \hat{j}\sin\phi \\ \hat{\phi} = -\hat{i}\sin\phi + \hat{j}\cos\phi \\ \hat{z} = \hat{k} \end{Bmatrix} \tag{A.6}$$

$$Cylindrical \rightarrow Cartesian: \begin{Bmatrix} \hat{i} = \hat{r}\cos\phi - \hat{\phi}\sin\phi \\ \hat{j} = \hat{r}\sin\phi + \hat{\phi}\cos\phi \\ \hat{k} = \hat{z} \end{Bmatrix} \tag{A.7}$$

If we calculate the derivatives of $\hat{\rho}$, $\hat{\phi}$, and $\hat{z}$ with respect to ρ, ϕ, and z, the only non-zeros terms are:

$$\frac{\partial\hat{\rho}}{\partial\phi} = -\hat{i}sin\phi + \hat{j}cos\phi = \hat{\phi} \tag{A.8}$$

And,

$$\frac{\partial\hat{\phi}}{\partial\phi} = -\hat{i}cos\phi - \hat{j}sin\phi = -\hat{\rho} \tag{A.9}$$

These are useful relationships can greatly simplify the derivation of Divergence and Curl in Cylindrical coordinates.

A.3. The *del* operator in Cylindrical coordinates

To express *del* operator ∇ in Cylindrical coordinates, we have to map the terms $\hat{i}\frac{\partial}{\partial x}$, $\hat{j}\frac{\partial}{\partial y}$, and $\hat{k}\frac{\partial}{\partial z}$ onto the terms $\hat{r}\frac{\partial}{\partial r}$, $\hat{\phi}\frac{\partial}{\partial \phi}$, and $\hat{z}\frac{\partial}{\partial z}$ in accordance with vector field is defined in Cylindrical coordinates $U(r,\phi,z)$. A direct approach is to use the chain rule and transformation relationships introduced above, namely,

$$\begin{aligned}\hat{\rho}\frac{\partial}{\partial \rho} &= (\hat{i}\cos\phi + \hat{j}\sin\phi)(\frac{\partial x}{\partial \rho}\frac{\partial}{\partial x} + \frac{\partial y}{\partial \rho}\frac{\partial}{\partial y}) \\ &= (\hat{i}\cos\phi + \hat{j}\sin\phi)(\cos\phi\frac{\partial}{\partial x} + \sin\phi\frac{\partial}{\partial y}) \\ &= \cos^2\phi\hat{i}\frac{\partial}{\partial x} + \sin\phi\cos\phi\hat{i}\frac{\partial}{\partial y} + \sin\phi\cos\phi\hat{j}\frac{\partial}{\partial x} + \sin^2\phi\hat{j}\frac{\partial}{\partial y}\end{aligned} \tag{A.10}$$

$$\begin{aligned}\hat{\phi}\frac{\partial}{\partial \phi} &= (-\hat{i}\sin\phi + \hat{j}\cos\phi)(\frac{\partial x}{\partial \phi}\frac{\partial}{\partial x} + \frac{\partial y}{\partial \phi}\frac{\partial}{\partial y}) \\ &= (-\hat{i}\sin\phi + \hat{j}\cos\phi)(-\rho\sin\phi\frac{\partial}{\partial x} + \rho\cos\phi\frac{\partial}{\partial y}) \\ &= \rho\sin^2\phi\hat{i}\frac{\partial}{\partial x} - \rho\sin\phi\cos\phi\hat{i}\frac{\partial}{\partial y} - \rho\sin\phi\cos\phi\hat{j}\frac{\partial}{\partial x} + \rho\cos^2\phi\hat{j}\frac{\partial}{\partial y}\end{aligned} \tag{A.11}$$

And,

$$\hat{z}\frac{\partial}{\partial z} = \hat{k}\frac{\partial}{\partial z} \tag{A.12}$$

Compare to Equation A.A.1, an intuitive attempt is to divide Equation A.A.11 by ρ, and add it to Equations A.A.10 and A.A.12, then,

$$\begin{aligned}\hat{\rho}\frac{\partial}{\partial \rho} + \frac{\hat{\phi}}{\rho}\frac{\partial}{\partial \phi} + \hat{z}\frac{\partial}{\partial z} &= (\sin^2\phi + \cos^2\phi)\hat{i}\frac{\partial}{\partial x} + (\sin^2\phi + \cos^2\phi)\hat{j}\frac{\partial}{\partial y} + \hat{k}\frac{\partial}{\partial z} \\ &= \hat{i}\frac{\partial}{\partial x} + \hat{j}\frac{\partial}{\partial y} + \hat{k}\frac{\partial}{\partial z}\end{aligned} \tag{A.13}$$

Therefore, we have,

$$\nabla = \hat{\rho}\frac{\partial}{\partial \rho} + \frac{\hat{\phi}}{\rho}\frac{\partial}{\partial \phi} + \hat{z}\frac{\partial}{\partial z} \tag{A.14}$$

A.4. Divergence in Cylindrical coordinates

Similar to analyzing divergence in Cartesian coordinates, the divergence in Cartesian coordinates is carried out by computing dot product of *del* operator ∇ and vector field $U(\rho, \phi, z)$. That is,

$$\begin{aligned}
\nabla \cdot U &= \left(\hat{\rho}\frac{\partial}{\partial \rho} + \frac{\hat{\phi}}{\rho}\frac{\partial}{\partial \phi} + \hat{z}\frac{\partial}{\partial z} \right)\left(U_\rho \hat{\rho} + U_\phi \hat{\phi} + U_z \hat{z} \right) \\
&= \hat{\rho}\left(\hat{\rho}\frac{\partial U_\rho}{\partial \rho} + U_\rho \frac{\partial \hat{\rho}}{\partial \rho} + \hat{\phi}\frac{\partial U_\phi}{\partial \rho} + U_\phi \frac{\partial \hat{\phi}}{\partial \rho} + \hat{z}\frac{\partial U_z}{\partial \rho} + U_z \frac{\partial \hat{z}}{\partial \rho} \right) \\
&+ \frac{\hat{\phi}}{\rho}\left(\hat{\rho}\frac{\partial U_\rho}{\partial \phi} + U_\rho \frac{\partial \hat{\rho}}{\partial \phi} + \hat{\phi}\frac{\partial U_\phi}{\partial \phi} + U_\phi \frac{\partial \hat{\phi}}{\partial \phi} + \hat{z}\frac{\partial U_z}{\partial \phi} + U_z \frac{\partial \hat{z}}{\partial \phi} \right) \\
&+ \hat{z}\left(\hat{\rho}\frac{\partial U_\rho}{\partial z} + U_\rho \frac{\partial \hat{\rho}}{\partial z} + \hat{\phi}\frac{\partial U_\phi}{\partial z} + U_\phi \frac{\partial \hat{\phi}}{\partial z} + \hat{z}\frac{\partial U_z}{\partial z} + U_z \frac{\partial \hat{z}}{\partial z} \right)
\end{aligned} \tag{A.15}$$

Since $\hat{\rho}$, $\hat{\phi}$, and $\hat{z}$ are orthogonal unit vectors, the inner product between each two are 0 (self-inner product equals to 1). Together with Equations A.A.8 and A.A.9, we have

$$
\begin{aligned}
\nabla \cdot U = \hat{\rho}\left(\hat{\rho}\frac{\partial U_\rho}{\partial \rho} + 0 + \hat{\phi}\frac{\partial U_\phi}{\partial \rho} + 0 + \hat{z}\frac{\partial U_z}{\partial \rho} + 0 \right) \\
+ \frac{\hat{\phi}}{\rho}\left(\hat{\rho}\frac{\partial U_\rho}{\partial \phi} + U_\rho\hat{\phi} + \hat{\phi}\frac{\partial U_\phi}{\partial \phi} - U_\phi\hat{\rho} + \hat{z}\frac{\partial U_z}{\partial \phi} + 0 \right) \\
+ \hat{z}\left(\hat{\rho}\frac{\partial U_\rho}{\partial z} + 0 + \hat{\phi}\frac{\partial U_\phi}{\partial z} + 0 + \hat{z}\frac{\partial U_z}{\partial z} + 0 \right) \\
= \left(\frac{\partial U_\rho}{\partial \rho} + \frac{U_\rho}{\rho} \right) + \frac{1}{\rho}\frac{\partial U_\phi}{\partial \phi} + \frac{\partial U_z}{\partial z} \\
= \frac{1}{\rho}\frac{\partial}{\partial \rho}\left(U_\rho \cdot \rho \right) + \frac{1}{\rho}\frac{\partial U_\phi}{\partial \phi} + \frac{\partial U_z}{\partial z}
\end{aligned}
\tag{A.16}
$$

A.5. Curl in Cylindrical coordinates

The calculation of curl follows the same fashion as divergence calculated in Cylindrical coordinates. The cross product is calculated between *del* operator ∇ and vector field $U(\rho, \phi, z)$.

$$
\begin{aligned}
\nabla \times U &= \left(\hat{\rho}\frac{\partial}{\partial \rho} + \frac{\hat{\phi}}{\rho}\frac{\partial}{\partial \phi} + \hat{z}\frac{\partial}{\partial z} \right) \times \left(U_\rho \hat{\rho} + U_\phi \hat{\phi} + U_z \hat{z} \right) \\
&= \hat{\rho} \times \left(\hat{\rho}\frac{\partial U_\rho}{\partial \rho} + U_\rho \frac{\partial \hat{\rho}}{\partial \rho} + \hat{\phi}\frac{\partial U_\phi}{\partial \rho} + U_\phi \frac{\partial \hat{\phi}}{\partial \rho} + \hat{z}\frac{\partial U_z}{\partial \rho} + U_z \frac{\partial \hat{z}}{\partial \rho} \right) \\
&\quad + \frac{\hat{\phi}}{\rho} \times \left(\hat{\rho}\frac{\partial U_\rho}{\partial \phi} + U_\rho \frac{\partial \hat{\rho}}{\partial \phi} + \hat{\phi}\frac{\partial U_\phi}{\partial \phi} + U_\phi \frac{\partial \hat{\phi}}{\partial \phi} + \hat{z}\frac{\partial U_z}{\partial \phi} + U_z \frac{\partial \hat{z}}{\partial \phi} \right) \\
&\quad + \hat{z} \times \left(\hat{\rho}\frac{\partial U_\rho}{\partial z} + U_\rho \frac{\partial \hat{\rho}}{\partial z} + \hat{\phi}\frac{\partial U_\phi}{\partial z} + U_\phi \frac{\partial \hat{\phi}}{\partial z} + \hat{z}\frac{\partial U_z}{\partial z} + U_z \frac{\partial \hat{z}}{\partial z} \right) \\
&= \hat{\rho} \times \left(\hat{\rho}\frac{\partial U_\rho}{\partial \rho} + 0 + \hat{\phi}\frac{\partial U_\phi}{\partial \rho} + 0 + \hat{z}\frac{\partial U_z}{\partial \rho} + 0 \right) \\
&\quad + \frac{\hat{\phi}}{\rho} \times \left(\hat{\rho}\frac{\partial U_\rho}{\partial \phi} + U_\rho \hat{\phi} + \hat{\phi}\frac{\partial U_\phi}{\partial \phi} - U_\phi \hat{\rho} + \hat{z}\frac{\partial U_z}{\partial \phi} + 0 \right) \\
&\quad + \hat{z} \times \left(\hat{\rho}\frac{\partial U_\rho}{\partial z} + 0 + \hat{\phi}\frac{\partial U_\phi}{\partial z} + 0 + \hat{z}\frac{\partial U_z}{\partial z} + 0 \right) \\
&= \frac{\partial U_\phi}{\partial \rho}\hat{z} - \frac{\partial U_z}{\partial \rho}\hat{\phi} - \frac{1}{\rho}\frac{\partial U_\rho}{\partial \phi}\hat{z} + \frac{U_\phi}{\rho}\hat{z} + \frac{1}{\rho}\frac{\partial U_z}{\partial \phi}\hat{\rho} + \frac{\partial U_\rho}{\partial z}\hat{\phi} - \frac{\partial U_\phi}{\partial z}\hat{\rho} \\
&= \hat{\rho}\left(\frac{1}{\rho}\frac{\partial U_z}{\partial \phi} - \frac{\partial U_\phi}{\partial z} \right) + \hat{\phi}\left(\frac{\partial U_\rho}{\partial z} - \frac{\partial U_z}{\partial \rho} \right) + \hat{z}\left(\frac{1}{\rho}\frac{\partial}{\partial \rho}\left(V_\phi \cdot \rho \right) - \frac{1}{\rho}\frac{\partial U_\rho}{\partial \phi} \right)
\end{aligned}
\tag{A.17}
$$

A.6. Gradient in Cylindrical coordinates

The gradient of a smooth vector field $U(\rho, \phi, z)$ in Cylindrical coordinates is defined to be a second order tensor field,

$$
\begin{aligned}
\nabla \otimes U = & \frac{\partial}{\partial \rho}\left(U_\rho \hat{\rho} + U_\phi \hat{\phi} + U_z \hat{z}\right) \otimes \hat{\rho} \\
& + \frac{\partial}{\partial \phi}\left(U_\rho \hat{\rho} + U_\phi \hat{\phi} + U_z \hat{z}\right) \otimes \frac{\hat{\phi}}{\rho} \\
& + \frac{\partial}{\partial z}\left(U_\rho \hat{\rho} + U_\phi \hat{\phi} + U_z \hat{z}\right) \otimes \hat{z} \\
= & \left(\frac{\partial U_\rho}{\partial \rho}\hat{\rho} + \frac{\partial U_\phi}{\partial \rho}\hat{\phi} + \frac{\partial U_z}{\partial \rho}\hat{z}\right) \otimes \hat{\rho} \\
& + \left(\frac{\partial U_\rho}{\partial \phi}\hat{\rho} + U_\rho \hat{\phi} + \frac{\partial U_\phi}{\partial \phi}\hat{\phi} - U_\phi \hat{\rho} + \frac{\partial U_z}{\partial \phi}\hat{z}\right) \otimes \frac{\hat{\phi}}{\rho} \\
& + \left(\frac{\partial U_\rho}{\partial z}\hat{\rho} + \frac{\partial U_\phi}{\partial z}\hat{\phi} + \frac{\partial U_z}{\partial z}\hat{z}\right) \otimes \hat{z} \\
= & \frac{\partial U_\rho}{\partial \rho}\hat{\rho} \otimes \hat{\rho} + \frac{\partial U_\phi}{\partial \rho}\hat{\phi} \otimes \hat{\rho} + \frac{\partial U_z}{\partial \rho}\hat{z} \otimes \hat{\rho} \\
& + \frac{1}{\rho}\left(\frac{\partial U_\rho}{\partial \phi} - U_\phi\right)\hat{\rho} \otimes \hat{\phi} + \frac{1}{\rho}\left(\frac{\partial U_\phi}{\partial \phi} + U_\rho\right)\hat{\phi} \otimes \hat{\phi} + \frac{1}{\rho}\frac{\partial U_z}{\partial \phi}\hat{z} \otimes \hat{\phi} \\
& + \frac{\partial U_\rho}{\partial z}\hat{\rho} \otimes \hat{z} + \frac{\partial U_\phi}{\partial z}\hat{\phi} \otimes \hat{z} + \frac{\partial U_z}{\partial z}\hat{z} \otimes \hat{z}
\end{aligned}
\tag{A.18}
$$

Or, in matrix form,

$$
gradU = [\nabla \otimes U] = \begin{bmatrix}
\dfrac{\partial U_\rho}{\partial \rho} & \dfrac{1}{\rho}\left(\dfrac{\partial U_\rho}{\partial \phi} - U_\phi\right) & \dfrac{\partial U_\rho}{\partial z} \\
\dfrac{\partial U_\phi}{\partial \rho} & \dfrac{1}{\rho}\left(\dfrac{\partial U_\phi}{\partial \phi} + U_\rho\right) & \dfrac{\partial U_\phi}{\partial z} \\
\dfrac{\partial U_z}{\partial \rho} & \dfrac{1}{\rho}\dfrac{\partial U_z}{\partial \phi} & \dfrac{\partial U_z}{\partial z}
\end{bmatrix}
\tag{A.19}
$$